IMPROVING MODEL REPRESENTATIONS OF BLACK CARBON USING A PARTICLE-RESOLVED AEROSOL MODEL

BY

LAURA FIERCE

DISSERTATION

Submitted in partial fulfillment of the requirements
for the degree of Doctor of Philosophy in Environmental Engineering in Civil Engineering
in the Graduate College of the
University of Illinois at Urbana-Champaign, 2015

Urbana, Illinois

Doctoral Committee:

Associate Professor Tami C. Bond, Chair
Associate Professor Nicole Riemer, Co-Director of Research
Dr. Susanne E. Bauer
Associate Professor Matthew West

Abstract

Particles containing black carbon (BC) alter the Earth's energy balance by scattering and absorbing solar radiation, by interacting with clouds, and by decreasing the albedo of ice and snow. Each of these climate effects depends on the properties of individual BC-containing particles and their atmospheric residence time. The dominant removal mechanism of BC mass from the atmosphere is wet deposition, with one important pathway being the activation of BC-containing particles into cloud condensation nuclei (CCN) and their subsequent removal if the cloud precipitates. Although freshly emitted BC-containing particles are too small and hydrophobic to activate, their morphology and chemical composition are altered soon after emission by condensation of semi-volatile gases and coagulation with pre-existing particles. This transformation in black carbon's characteristics, termed "aging", increases particles' susceptibility to cloud droplet nucleation and wet removal. Further, these aging process also modify light absorption and scattering by particles containing black carbon. However, a complex aerosol population that evolves with time is not easily simulated in climate models, so even sophisticated aerosol schemes do not fully resolve aerosol properties on a per-particle level.

The objective of this research is (1) to improve the scientific understanding of the underlying factors that drive aerosol aging, (2) to quantify error in climate-relevant aerosol properties for the approximate representations of aerosol microphysical properties that are commonly applied in global models, and (3) to produce parameterizations that enable improved representations of black carbon within existing global model frameworks. Particle-resolved model simulations were used to complete these objectives. First, I applied a process-level analysis to identify the set of independent variables that best explain variance in BC's aging timescale for a large collection of simulations. I show that 80-90% of variance in BC's aging timescale is explained by just a few independent variables. Second, I used PartMC-MOSAIC as a benchmark for comparing other aerosol modeling frameworks. I found that cloud condensation nuclei activity can often be modeled with high accuracy using very simple representations of aerosol composition, but more complex representations of aerosol composition are needed to simulate aerosol absorption. Finally, based on particle-resolved simulations I developed one parameterization to represent black carbon's aging timescale and a different parameterization to predict enhancement in light absorption by mixed BC populations.

To my family

Acknowledgements

The research described in this dissertation would not have been possible without the support and guidance from many others.

I thank my advisors Tami Bond and Nicole Riemer for their mentorship and for demanding excellence in my work. I am grateful to them for taking me on as their student, for the helpful discussions, for editing my writing, and for their patience. I am also grateful to the other members of my doctoral committee, Susanne Bauer and Matthew West, for the many thoughtful suggestions to improve my research over the years.

I also thank many colleagues, professors, and friends for their help and inspiration. I thank all members of the Bond, Riemer, and PartMC research groups, past and present, for their many insightful suggestions. Specifically, I am grateful to Cheryl Weyant for her critical feedback of my work, to Benjamin Barnes for the many discussions on my early research, for editing my first manuscripts, and for providing feedback on my defense presentation, to Peter Maginnis for his thoughtful ideas on my first two manuscripts, to Jeffrey Curtis for helping me debug many computing issues, and to Francisco Mena Gonzales for the lively discussion and for helping me with particle optical modeling. I also thank the many others who have contributed that are not specifically named here.

This research would not have been possible without financial support from the National Atmospheric and Space Administration (NNX09AK66G) or the Untied States Environmental Protection Agency (R835042).

Table of Contents

Chapter 1

Introduction

The Earth's atmosphere modulates the balance between incoming solar radiation and energy that is radiated back to space. Changes in the composition of the atmosphere alter this radiative balance. Anthropogenic emissions of greenhouse gases have caused changes in climate relative to pre-industrial times, evident through an increase in the global mean surface temperature (50; 93; 68; 69; 126), an increase in upper ocean temperatures (80), rise in sea level (148; 30), and decreases in the extent of arctic sea ice (141). This warming effect by greenhouse gases is partially offset by cooling from atmospheric aerosols (96).

This dissertation makes a contribution to understanding how aerosols affect the radiative balance through absorption of solar radiation and through cloud interactions. Specifically, this dissertations quantifies error in particle absorption and cloud-nucleating properties from common representations of aerosol composition, identifies variables that most affect these climate-relevant properties, and provides parameterizations for improving aerosol model representations. Before describing my research contribution, this section provides background on radiative forcing in general, properties of atmospheric aerosol, direct and indirect aerosol radiative effects, and model representations of atmospheric aerosol.

1.1 Radiative forcing

Uncertainty in the perturbation of Earth's radiative budget due to anthropogenic aerosols exceeds uncertainties from all other climate forcing mechanisms combined (96). The response in Earth's energy balance to changes in a particular atmospheric component is quantified in terms of "radiative forcing." Specifically, Ramaswamy et al. (111) defines radiative forcing as "the change in the net irradiance at the tropopause after allowing for stratospheric temperatures to readjust to radiative equilibrium, but with surface and tropospheric temperatures and state held fixed at the unperturbed values." The radiative forcing of a particular component depends on its atmospheric abundance and its radiative properties (96). The effective radiative forcing is similar to the instantaneous radiative forcing, but effective radiative forcing also accounts for rapid adjustments in the troposphere that may increase or decrease the effects the direct radiative perturbation

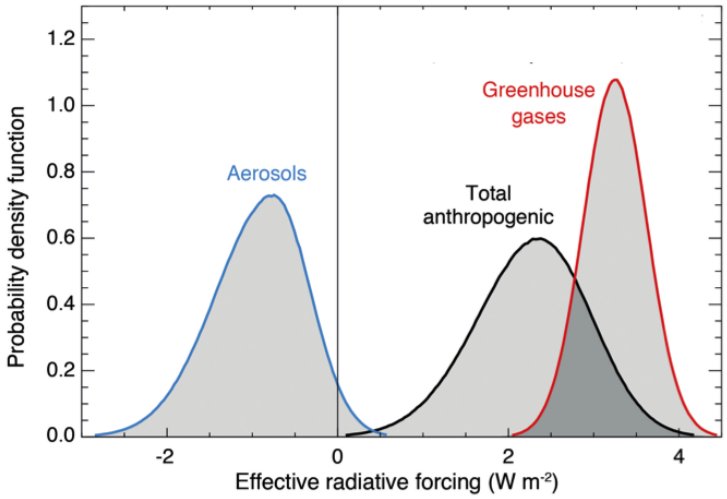

Figure 1.1: Probability density distribution of radiative forcing predictions, reproduced from (96).

(96).

Figure 1.1 shows the probability density distributions for present-day radiative forcing by anthropogenic emissions, constructed using a series of global model simulations. The overall anthropogenic forcing (black curve) is the combined effect of forcing by greenhouse gases (red curve) and by forcing aerosols (blue curve). Whereas forcing by greenhouse gases ranges from +2.5 to +3.1 m^{-2} (90% confidence levels) (96), the negative forcing by aerosols partially offsets this positive greenhouse forcing, leading to an overall anthropogenic forcing of +1.1 to +3.3 W m^{-2} (96). This uncertainty in total anthropogenic forcing is driven largely by uncertainty in the prediction of aerosol radiative effects, with predictions of effective aerosol radiative forcing ranging from −1.9 to −0.1 W m^{-2} (17). As will be explained in Section 1.3, this uncertainty in aerosol radiative forcing is caused by uncertainties in the way that aerosols affect the climate directly, through scattering and absorption and solar radiation, and indirectly, by interacting with clouds.

1.2 Properties of atmospheric aerosol

An aerosol is a stable population of solid or liquid particles suspended in a gas, where a population refers to a collection of distinct, multi-component particles. The ways aerosols impact climate are fundamentally different from those of greenhouse gases. Greenhouse gases are mostly transparent to incoming solar radiation at visible wavelengths, but affect the climate by absorbing radiation at infrared wavelengths emitted from the Earths surface. Aerosols, on the other hand, interact with incoming solar radiation either through direct

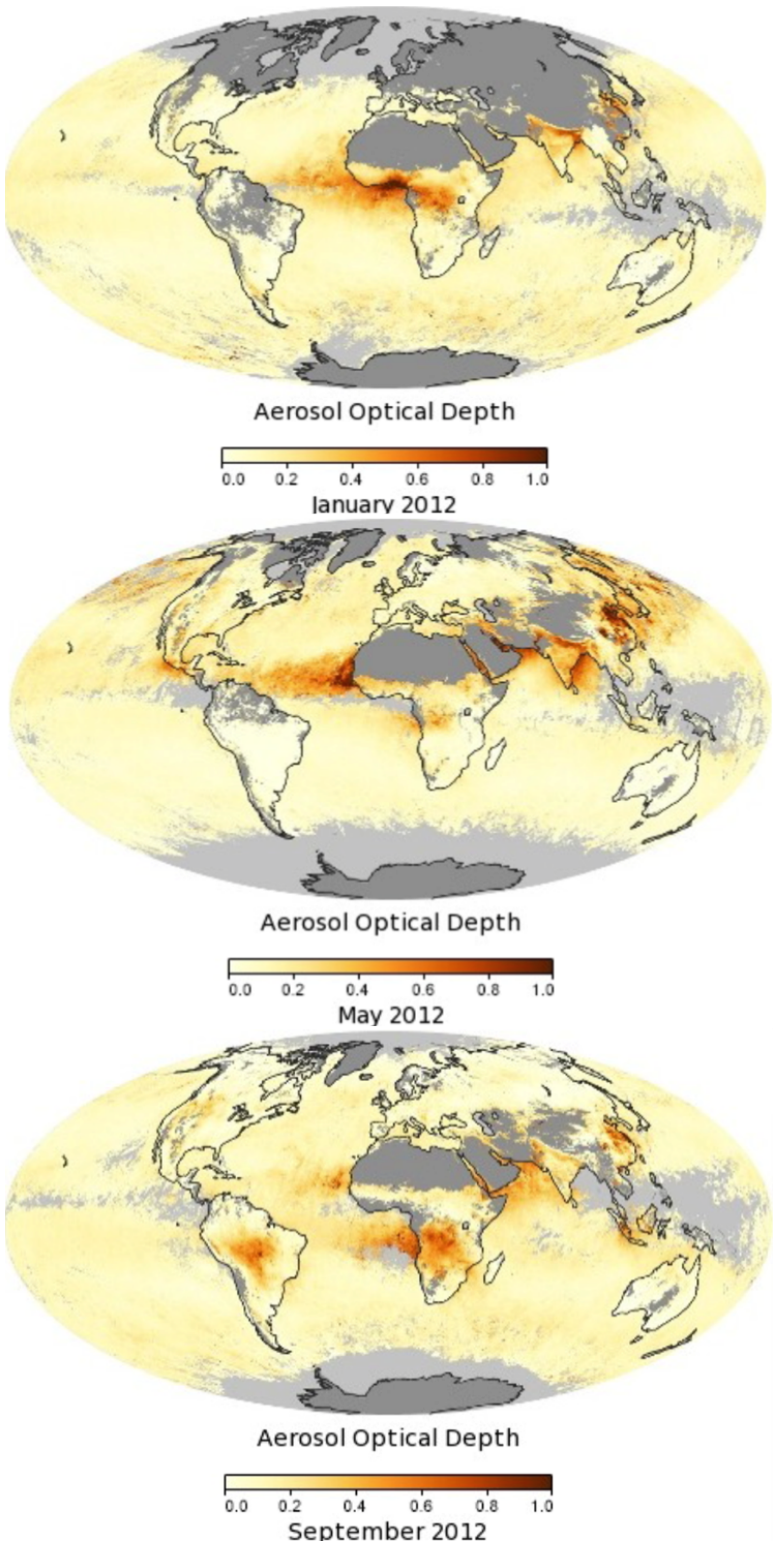

Figure 1.2: Aerosol optical depth predicted by Moderate Resolution Imaging Spectroradiometer (MODIS) on NASAs Terra satellite in January (top), May (middle), and September (bottom) of 2012. (98)

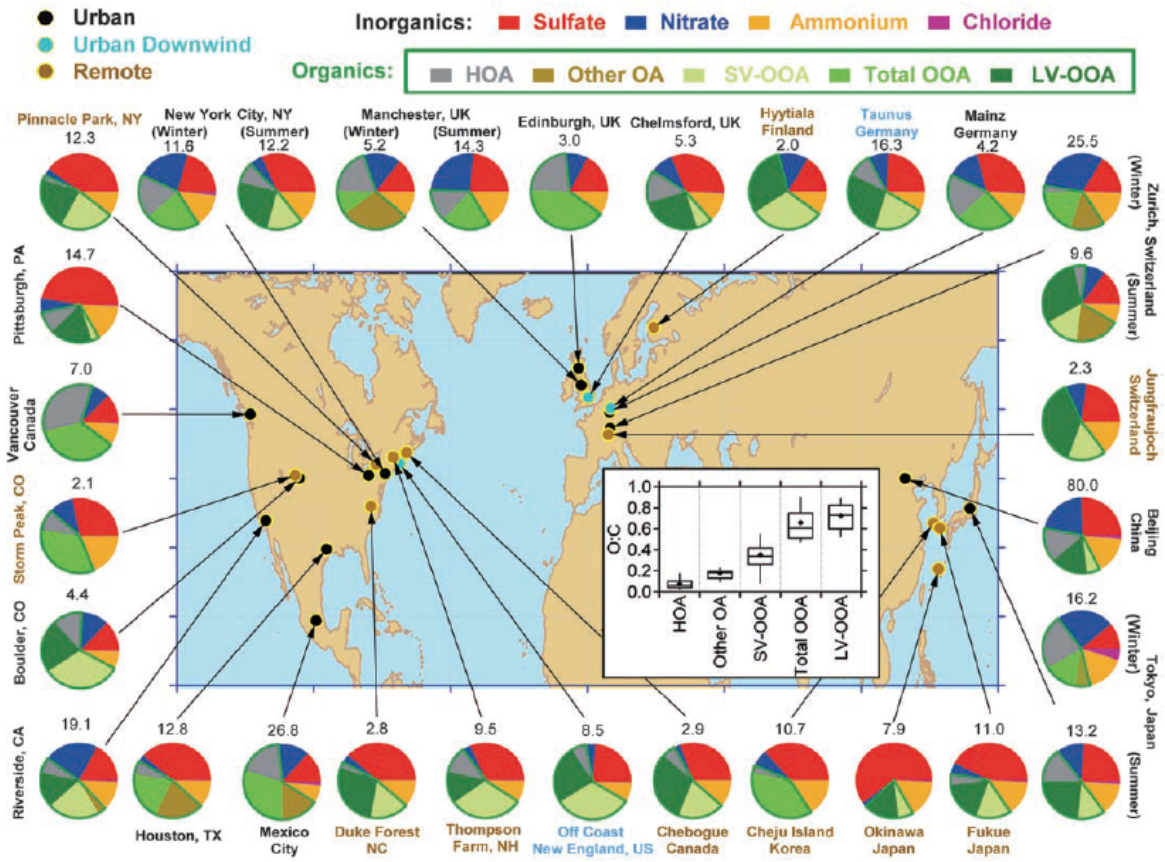

Figure 1.3: Spatial variation in aerosol composition, observed by the aerosol mass spectrometer (65).

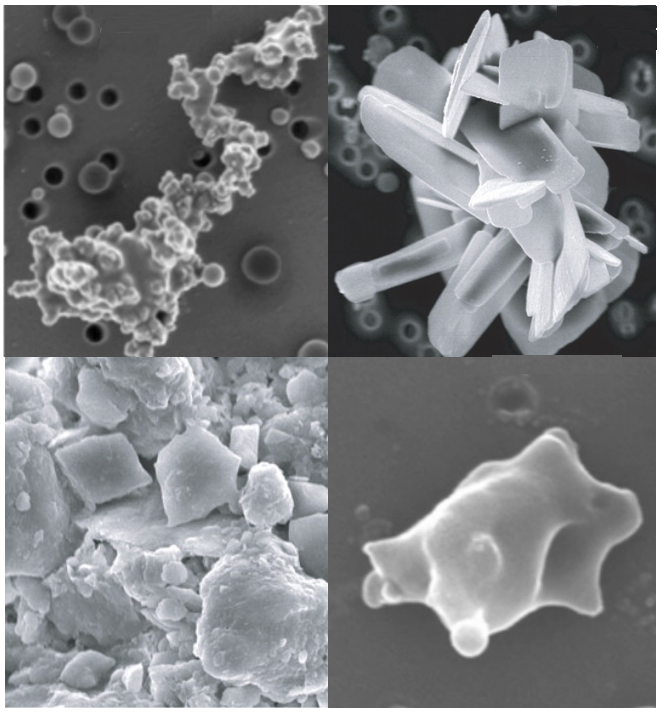

Figure 1.4: Electron microscope images illustrate dramatic variation in particle size, shape, and chemical composition (47; 26).

scattering and absorption by suspended particles (51; 12; 134; 71) or indirectly through their interactions with clouds (137; 138; 3; 84).

Aerosols may be emitted to the atmosphere directly from anthropogenic and natural sources, known as "primary" particles, or they may form in the atmosphere from nucleation of gas-phase precursors, known as "secondary" particles. Once particles are emitted or formed, their composition and morphology evolve through condensation of semi-volatile substances and through particle coagulation (144; 67). Further, unlike long-lived greenhouse gases, aerosols remain in the atmosphere on the order of days to weeks (99). Due to their short atmospheric lifetimes and variation in aerosol emission sources, aerosol abundance and composition varies in time and space.

Over the last decades the variation of abundance and composition with time and space has been surveyed with remote sensing techniques and with in situ measurements, both airborne and ground based. Figure 1.2 shows the spatial and temporal variation in aerosol optical depth observed by the Moderate Resolution Imaging Spectroradiometer (MODIS) on NASA's Terra satellite (98). The aerosol optical depth indicates the reduction in light transmitted to the surface due to absorption and scattering by aerosols, indicating the spatial and temporal variation in aerosol abundance from a satellite view. Agricultural fires and land clearing over South America lead to high values of aerosol optical thickness between July and September

(Figure 1.2c). On the other hand, dust storms over the Arabian Peninsula lead to elevated optical thicknesses over the Atlantic Ocean between May and August (Figure 1.2b). Anthropogenic aerosol emissions lead to high aerosol optical thicknesses are high over China most of the year. Figure 1.2 demonstrates that the wide spatial and temporal variation in aerosol abundance is driven largely by variation in emissions.

Although satellites provide information about spatial variation in aerosol optical thickness, they sense only the total effect of many collocated aerosol types. Aircraft and ground-based measurements help to improve our understanding of aerosol properties, though these observations have a limited spatial coverage. Figure 1.3 shows the spatial variation in bulk aerosol composition, including organics, sulfate, nitrate, ammonium, and chloride of particulate mater with diameters smaller than 1 μm. The observations shown in Figure 1.3 do not show the concentration of black carbon, which is a focus of this dissertation, because refractory materials like black carbon are difficult to measure by techniques that work for other types of aerosols.

Information on bulk aerosol composition is sparse, but even less information is available about the composition and morphology of individual particles. Ambient observations of particle-level properties show tremendous variation in the morphology and chemical composition of individual particles (78; 156), caused by differences in particle emission sources and in their atmospheric transformations (67; 41). Figure 1.4 shows electron microscope images of individual aerosol particles (47; 26), demonstrating the dramatic variation in particle microphysical properties between aerosol types.

This dissertation focuses on particles containing a particular aerosol component, black carbon (BC). BC forms in flames as a product of incomplete fuel combustion. BC enters the atmosphere as chain-like agglomerates with diameters on the order of tens to hundreds of nanometers, and the characteristics these freshly emitted particles vary, depending on the emission source and combustion conditions. Although particles containing BC also contain other aerosol species, for simplicity we refer to BC-containing particles as "BC particles".

Unlike most aerosol types, which scatter incoming solar radiation and, thereby, cool the planet, BC is strongly absorbing and, hence, has a strong warming effect (117; 15; 96). Figure 1.5 shows how predictions of direct forcing by black carbon compare with predictions of other aerosol effects. In addition to its direct warming, BC may decrease or increase cloud cover by altering the thermal structure of the atmosphere (1) and by altering the optical properties of cloud droplets (31; 63), known as semi-direct effects. Further, BC that has deposited on ice and snow decreases the surface albedo (49; 61), which warms the climate and leads to increased melting. Transport of BC-containing particles to the arctic depends on the treatment of BC removal processes (18), which depend strongly on the treatment of particle CCN activation and wet

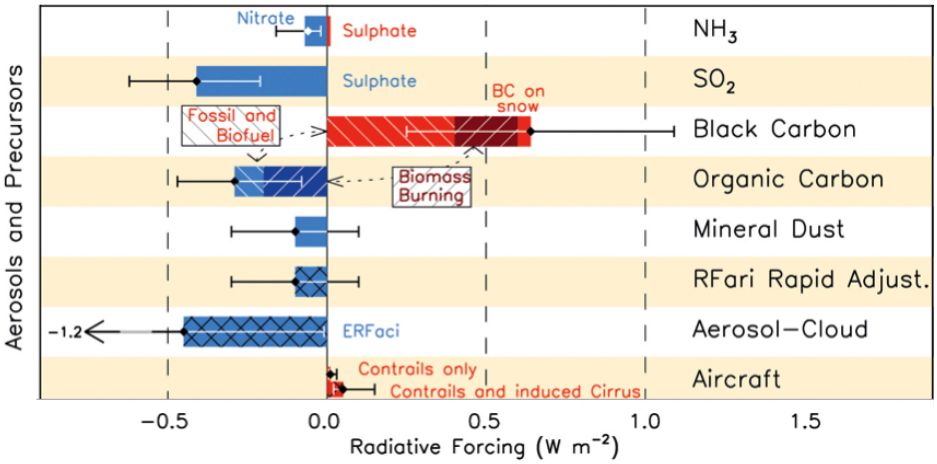

Figure 1.5: Estimates of radiative forcing associated with atmospheric aerosols, reproduced from (96)

deposition (35).

The lifetime of black carbon is approximately one week (20; 131), as opposed to carbon dioxide, which has an estimated lifetime to be on the order of 50 to 100 years (62) or much longer (6; 7). Even with its short atmospheric lifetime, black carbon absorbs so strongly that BC-containing particles have a significant climate impact (110; 57; 15). Whereas Figure 1.5 shows direct radiative forcing by BC, the best estimate for total radiative forcing by black carbon through all mechanisms is +1.1 W m^{-2} with 90% confidence bounds ranging from +0.17 W m^{-2} to +2.1 W m^{-2} (15).

1.3 Aerosol radiative effects

The total aerosol forcing is the combination of direct aerosol forcing, which is estimated to range from +0.05 W m^{-2} to -0.95 W m^{-2} (96), and indirect aerosol forcing due to cloud interactions, which ranges from 0 W m^{-2} to -1.2 W m^{-2}. These direct and indirect aerosol effects depend on the characteristics of complex aerosol populations (59; 119; 16; 19; 95) and and environmental conditions. Therefore, physically-based models of aerosol effects must simulate the three-dimensional distribution of aerosol populations and their interactions with other components of the climate system, which is not easily captured in global and regional chemical transport models or by atmospheric measurements. This section describes the dominant aerosol forcing mechanisms and how they depend on particle-level characteristics of aerosol populations.

1.3.1 Influence of aerosol microphysical properties on direct forcing

Estimating the direct radiative effects of atmospheric aerosols requires knowledge of the influence of particles, as a bulk, on radiative transfer through the atmosphere, and these bulk aerosol radiative effects depend on the interactions of individual particles with, primarily, incoming solar radiation. Light interacts with an individual particle by either 1) scattering light in all directions or 2) absorbing a portion of the radiation and converting into thermal energy. As incident solar radiation is transmitted through an atmospheric layer, the cumulative effects of scattering and absorption by many particles leads modifies the flux of solar energy through the layer, where in this discussion flux is defined as being positive in the direction of incident radiation. A net decrease in radiative flux indicates that absorbed radiant energy is being transferred to heat. The corresponding atmospheric heating rate depends on the changes in net flux and the thermal mass of the atmospheric layer.

The bulk effects of scattering and absorption by aerosol populations are quantified in terms of the volume scattering coefficient (b_{scat}) and the volume absorption coefficient (b_{abs}), respectively. The coefficients b_{scat} and b_{abs} indicate the attenuation in transmitted light caused by absorption and scattering, respectively. Aerosol properties related to direct aerosol forcing and visibility depend on the three-dimensional distribution in b_{scat} and b_{abs}. For example, the aerosol optical depth (Figure 1.2) is computed as the integration of the aerosol extinction coefficient, which is the combination of b_{scat} and b_{abs}, over the entire vertical column.

For a specific aerosol population, b_{scat} and b_{abs} of a population of particles depends on the scattering cross section (σ_{scat}) and the absorption cross section (σ_{abs}), in units of m^2, of individual particles. For a given particle, σ_{scat} and σ_{abs} quantify the likelihood of a scattering or absorption event, respectively. Scattering and absorption by individual particles are modeled using Mie theory, which describes scattering of an electromagnetic wave by a sphere. Values for σ_{scat} and σ_{abs} predicted by Mie theory depend on the size, composition, and configuration, where the configuration of components within a particle is modeled using simple approximations.

Estimating σ_{scat} and σ_{abs} is challenging because different aerosol components are often mixed within the same particle, and the size, shape, and distribution of components within individual particles is not easily simulated. Global models simulate approximate representations of aerosol composition(145; 56; 88; 11; 9), in addition to simplifying particle morphology. For example, some global models simulate the evolution of aerosol components in separate size bins, assuming uniform composition for particles of the same size. For each size bin, σ_{scat} and σ_{abs} are computed as a function of the simplified composition, and b_{scat} and b_{abs} are computed from the integration of σ_{scat} and σ_{abs}, respectively, for each size bin, weighted by the number

concentration of particles in each size bin.

Model predictions of direct aerosol forcing are sensitive to the treatment of particle characteristics. Chung and Seinfeld (29) found that BC would be expected to raise the global average surface air temperature by 0.2 K if BC is assumed to exist in pure, uncoated particles, based on 100-year simulations. If, instead, BC was assumed to be internally mixed with sulfate aerosol, they predicted nearly twice the increase in global average surface temperature.

1.3.2 Influence of aerosol microphysical properties on indirect forcing

Aerosol particles act as nuclei for cloud droplet formation. An increase in aerosol concentrations due to anthropogenic may increase cloud droplet number and lead to more reflective clouds (137; 138) with longer atmospheric lifetimes (3), known as the first and second indirect effects, respectively. This perturbation in cloud properties from anthropogenic aerosol emissions is estimated to have a strong cooling effect on the climate (17).

Similar to direct scattering and absorption, aerosol effects on clouds also depend on interactions between particles and the environment. In air supersaturated with water vapor, aerosol particles may become activated for cloud formation, and these particles are defined to be cloud condensation nuclei (CCN) at that supersaturation level. CCN activation depends on the environmental supersaturation and the size and composition of individual particles, in that large, hygroscopic particles are better able to activate cloud droplets. The number concentration of CCN in a given location is the total number of particles per unit volume that have a critical supersaturation for CCN activation (s_c) lower than the environmental supersaturation (s), where s_c is a function of particle-level properties and s depends on the local environmental conditions, such as temperature, pressure, and the partial pressure of water vapor. Therefore, perturbations to cloud droplet number concentrations, which governs the aerosol indirect effects, depend on changes in the number concentration of particles that are hygroscopic enough to serve as CCN and the collocation of these droplets with elevated supersaturation levels.

Assumptions about particle characteristics (38; 86; 140) and their transformations in the atmosphere (41; 67) are important for predicting aerosol CCN activity. For example, although freshly emitted BC-containing particles are too small and hydrophobic to activate (85; 144), they become larger and more hygroscopic after emission by condensation of semi-volatile gases and coagulation with pre-existing particles (67; 102; 155). This change in aerosol size and composition, termed "aging" (144), increases particles' susceptibility to CCN activation (19; 55; 159; 4; 46). Further, in addition to playing a role in the aerosol indirect effect,

absorbing particles like BC may also decrease or increase cloud cover by altering the thermal structure of the atmosphere (1) and by altering the optical properties of cloud droplets (31; 63), known as semi-direct effects.

In addition to being important for understanding aerosol indirect effects, cloud-aerosol interactions influence the removal rate of many aerosol types (123). A common pathway for wet removal is the activation of BC-containing particles into cloud condensation nuclei and their subsequent removal through precipitation (35). Therefore, the lifetime and transport of particles depends on the timescale for the initially hydrophobic particles to become sufficiently hygroscopic to be CCN (105).

1.4 Model representations of atmospheric aerosols

While observations are helping to improve our understanding of aerosol radiative effects now, models are needed to predict global distribution in aerosol abundance and composition in past, present, and future, to quantify interactions between aerosols and other components of the climate system, and to disaggregate the influence of individual chemical components or individual sources on the climate system. This section provides an overview of chemical transport models and commonly used aerosol schemes.

1.4.1 Chemical transport models

Chemical transport models simulate changes in atmospheric composition due to changes in gas and aerosol components, the radiative responses and cloud feedback resulting from this changes in atmospheric composition, and the response in regional and global climate caused by these changes in radiative effects (123). These models simulate interacting processes using coupled equations that represent emissions, transport, transformations, and removal of gas and aerosol components.

Aerosols are only one component of chemical transport models, but, as explained in Section 1.3, their climate-relevant properties depend on local meteorology, chemical interactions between gas-phase components, and the changes in their characteristics after emission. For this reason, the evolution of aerosol properties must be simulated using aerosol microphysical schemes that operate within global models. However, because chemical transport models simulate a number of interacting processes in addition to aerosols, the representation of aerosol microphysical properties is necessarily limited in these schemes to minimize their computational cost.

1.4.2 Bulk aerosol schemes

The simplest representations of aerosols in global models are bulk aerosol schemes (33; 74; 28). These schemes track the three-dimensional distribution in aerosol mass, without resolving any information about the characteristics of individual particles. The size distribution is prescribed for each aerosol species. The dominant chemical components of atmospheric aerosol represented by these models include sulfates, black carbon, organic carbon, mineral dust and, sea salt. Initially insoluble primary aerosol like black and organic carbon become hygroscopic through processing in the atmosphere, and these simple models capture this transformation using a first-order aging timescale that is on the order of 1-3 days (33; 74; 28). The first-order model of aging is the simplest representation of aerosol transformations applied in global models.

1.4.3 Distribution-based aerosol models

Many global models have moved toward the inclusion of aerosol microphysical schemes, which simulate the evolution of the aerosol size distribution rather than prescribe it. Figures 8.5b and 8.5c shows two representations of aerosol size and composition commonly applied in global models. Sectional models (145; 56) track the evolution of aerosol species within separate size bins, assuming particles of the same size have the same composition. On the other hand, modal models (11; 9) track the evolution of separate lognormal size distribution, assuming particles within a mode have the same composition even while assuming the size distribution shape.

While univariate sectional and modal models are the most common representation of aerosol microphysical properties in global models, schemes that resolve additional microphysical details have been developed as box models or are being implemented in global models. The box model MADRID-BC (102) uses a 2-D sectional framework to simulate the evolution of distributions with respect to particle diameter and black carbon mass fraction. A 3-D sectional model, MOSAIC-MIX, that represents distributions with respect to dry diameter, hygroscopic parameter, and black carbon mass fraction is currently under development (**?**). Multivariate distributions have also been simulated using a moment-based approach (149; 90; 89).

1.4.4 Particle-resolved aerosol models

This dissertation describes simulations using the most detailed representation representation of aerosol microphysics, the particle-resolved aerosol model (Figure 8.5a). The particle-resolved model fully resolves the distribution in particle composition (115) but is computationally too expensive for global-scale simulations.

Both sectional and modal aerosol models simulate the evolution of univariate aerosol distributions with

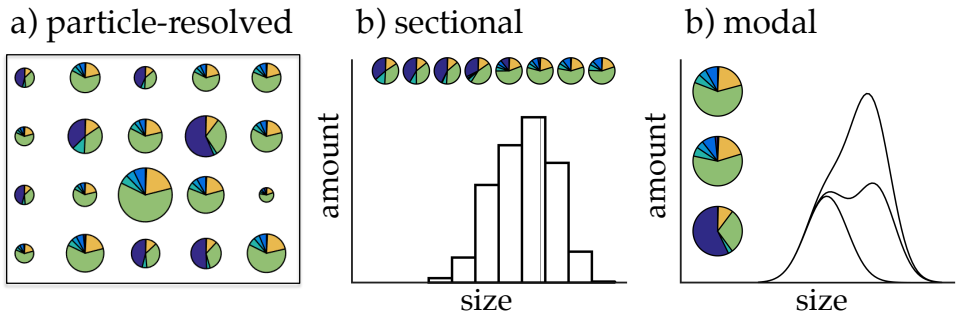

Figure 1.6: Aerosols in models: (a) particle-resolved models track particle-level composition for thousands of particles but are computationally too expensive for global simulation, whereas (b) sectional and (c) modal models do not adequately resolve variation in particle characteristics.

respect to particle size, where size is expressed as either dry diameter, volume, or mass. On the other hand, particle-resolved model tracks each simulated particle, fully resolving variation in aerosol components between individual particles. Additional details on the particle-resolved model are provided in Section 3.1.

1.5 Scope of dissertation

In this dissertation, a particle-resolved aerosol model is used to quantify error in, and improve, less detailed representations of aerosol composition. Although many of the findings apply to primary particles or aerosols in general, we focus on particles containing black carbon. Black carbon has distinct optical properties and hygroscopic properties than other types of aerosols, and the studies described in this dissertation show that particle-level characteristics strongly affect black carbon's radiative properties.

The objectives of the dissertation research are described in Chapter 2, and a general overview of the research methodology is described in Chapter 3. Chapters 4–7 describes the findings of five different modeling studies that were designed to meet the objectives described in Chapter 2. A final summary of the conclusions is provided in Chapter 9.

Chapter 2

Research objectives

Previous studies have shown that particle-scale characteristics affect predictions of black carbon's climate impact (38; 86; 29; 2). Climate models require a means to account for particle-level variation in key characteristics that does not require substantial computational cost. This dissertation is based on the hypothesis that the findings from particle-resolved model simulations can be generalized in order to improve aerosol simulations in global models.

Overview of research objectives: The objective of this research is 1) to improve the scientific understanding of the underlying factors that drive aerosol aging, 2) to quantify error in climate-relevant aerosol properties for the approximate representations of aerosol microphysical properties that are commonly applied in global models, and 3) to produce parameterizations that enable improved representations of black carbon within existing aerosol model frameworks. A meta-analysis of multiple particle-resolved model simulations are used to accomplish these objectives.

2.1 Sensitivity of CCN activity to particle characteristics at emission

Background: The CCN activation properties of an aerosol population depend on the distribution in particle size and composition. The distribution in particle size and composition of primary aerosol emissions varies between sources and, for many sources, is not well known. However, the characteristics of emitted particles are modified after emission by condensation and coagulation, so it is unclear to what degree particle characteristics at emission influence the CCN activity after aging.

Study objective: The objective of this study is to improve the scientific understanding of the connection between particle characteristics at emission and their CCN activation properties after aging. This study identifies when, if ever, the CCN activity of aged aerosol is affected by uncertainty in aerosol characteristics

at emission and, thereby, the importance of resolving specific particle-level characteristics for freshly emitted particles.

2.2 Factors that explain variance in black carbon's aging timescale

Background: Black carbon is emitted in small, hydrophobic particles that are initially unlikely to be encompassed in cloud droplets. However, particles soon age by condensation and coagulation, enabling their activation as CCN and subsequent removal through wet deposition if the cloud precipitates. It has been estimated that 80% of black carbon mass is removed through wet deposition, so models must adequately represent this transformation of BC-containing particles from hydrophobic to hygroscopic in order to model BC's atmospheric lifetime. The simplest representation of this aging process represents BC mass in two separate classes, hydrophobic ("fresh") BC and hygroscopic ("aged") BC, and assumes that BC transitions from fresh to aged according to a first-order timescale. However, changes in BC's susceptibility to wet removal varies with local conditions and depend the characteristics of individual BC-containing particles. The timescale for BC's transformation from hydrophobic to hygroscopic through aging is not well constrained, and the extent to which this aging timescale varies with local conditions is not well understood.

Study objective: The objective of this study is to improve the scientific understanding of black carbon's atmospheric lifecycle by identifying the factors that most affect changes in BC-containing particles' hygroscopic properties. Specifically, this study aims to identify the independent variables that most affect transformations in BC's CCN activation properties through aging. These independent variables identified in this study are used in a later study, which is described in Section 2.5, to develop a parameterization that can be applied directly in global models.

2.3 Impact of particle-level composition on absorption enhancement by black carbon

Background: Modeling and laboratory studies suggest that absorption by black carbon is enhanced when BC is coated with non-absorbing material, but recent observations find only weak absorption enhancement from aerosol coatings. Modeled particles do not represent real BC-containing particles found in the atmosphere in various ways. Other authors have evaluated how unrealistic representations of particle config-

uration lead to error in modeled absorption by black carbon, but no study has evaluated how oversimplified representations of aerosol composition could contribute to the discrepancy between modeled and measured absorption by black carbon.

Study objective: The objective of this study is to quantify the degree to which particle-level variation in composition affects population-level absorption enhancement, considering many aerosol populations that have aged under different atmospheric conditions, and to evaluate whether the oversimplification of aerosol composition could explain some of the discrepancy between modeled and measured absorption. The particle-resolved model PartMC-MOSAIC is used to find realistic distributions in the composition of BC-containing particles, representing variation in particle-level composition that other modeling studies have not considered. Simulating a series of scenarios, this study aims to identify how absorption predicted by the particle-resolved model, which accounts for diversity in particle composition, compares with an oversimplified representation in which all BC-containing particles are assumed to have identical composition, neglecting diversity in particle composition within BC populations.

2.4 Relationship to predict absorption by complex BC populations

Background: Modal aerosol schemes require a method to predict absorption by populations of BC-containing particles, while somehow accounting for variation in relevant particle-level properties. Study 4 shows that, by assuming uniform composition across particle populations, modal models overestimate absorption by BC. However, this study also showed that absorption enhancement from the particle-resolved model can be predicted with high accuracy with knowledge of only a few variables, all of which global models are able to track.

Objective: The objective of this study is to improve the scientific understanding of black carbon's radiative effects by developing a parameterization for absorption enhancement by black carbon that can be used in models of the global atmosphere and Earth system. This objective is based on the hypothesis that a parameterization of particle-resolved model data can be used to represent variation in particle composition in absorption calculations and will not increase computational costs. The parameterization predicts the absorption coefficient by populations of BC-containing particles as a function of five independent variables: (1) the mass concentration of BC in each population, (2) the volume fraction of dry aerosol coatings, (3) the hygroscopicity of that coating, (4) the environmental relative humidity, and (5) the wavelength of light.

This study aims to develop and validate the parameterization for absorption enhancement and to evaluate the impact of this parameterization on absorption aerosol optical depth.

2.5 Identifying the minimal representation of the aerosol composition

Background: Global models simplify the representation of particle size and composition, and these approximations likely affect model predictions of CCN activity and optical properties. Models are moving toward more detailed representations of particle composition, but the extent to which common representations of aerosol composition represent climate-relevant aerosol properties is not known. Error in CCN concentrations and aerosol optical properties from approximate representations of the aerosol mixing state has not been thoroughly quantified, so it is unclear what the minimal representation of aerosol composition is required for global aerosol simulations.

Study objective: The objective of this study is to improve model representations of atmospheric aerosols by evaluating error from commonly applied representations of the aerosol mixing state. Error in CCN activity and aerosol optical properties caused by approximating particle composition is evaluated through comparisons with particle-resolved model data. By identifying the minimal representation of the aerosol mixing state needed to adequately model climate-relevant aerosol properties and the timescale for approximate representations to become valid, the results of this study will instruct the development of more accurate aerosol models.

Chapter 3

Methodology

This dissertation describe a series of studies using the Particle Monte Carlo (PartMC) model coupled to the Model for Simulating Aerosol Interactions and Chemistry (MOSAIC). PartMC-MOSAIC was used to quantify error in CCN concentrations and aerosol absorption from approximate representations of the aerosol mixing state, to identify the variables that most affect changes in CCN activation by primary emissions, and to develop parameterizations to improve black carbon representations in existing global and regional aerosol schemes. This chapter provides an overview of the methodology behind these studies.

All studies include a few common steps: (1) simulate the evolution of aerosol populations with the particle-resolved model PartMC-MOSAIC, (2) predict climate-relevant properties from PartMC-MOSAIC output, and (3) apply different approaches to connect findings from the particle-resolved model to bulk and distribution-based schemes. The continuity equations that describe the evolution of the aerosol mixing state are described in Section 3.1, along with their numerical implementation in PartMC-MOSAIC. Section 3.2 describes models for optical properties, hygroscopic growth, and cloud condensation nuclei activation of individual particles, which take as inputs the particle-resolved composition output from PartMC-MOSAIC. Section 3.2 also describes how bulk properties of aerosol populations are computed from the particle-level quantities modeled by PartMC-MOSAIC. Finally, an overview of various approaches to connect the particle-resolved model findings to less detailed aerosol models, for example, through the identification of key sensitivities and development of parameterizations, are described in Section 3.3.

3.1 Particle-resolved simulation of aerosol dynamics

The particle-resolved model PartMC-MOSAIC was used to simulate the evolution of individual aerosol particles by emissions, dilutions with background, condensation and evaporation of semi-volatile substances, and coagulation with other particles. Unlike other aerosol models, which approximate the representation of particle composition, PartMC-MOSAIC fully resolves the aerosol mixing state. The full aerosol mixing state is a A-dimensional distribution for A aerosol species. Per-particle composition is given by the vector

$\vec{\mu}$, where each component μ_i is the mass of each constituent species $i = 1, ..., A$. The number concentration of particles with a particular composition $\vec{\mu}$ is given by:

$$n(\vec{\mu}, t) = \frac{\partial N^A(\vec{\mu}, t)}{\partial \mu_1 \partial \mu_2 ... \partial \mu_A}, \tag{3.1}$$

where $N(\vec{\mu}, t)$ is the cumulative distribution with respect $\vec{\mu}$.

This multivariate mixing state distribution evolves by simultaneous processes. The continuity equation describing the evolution of $n(\vec{\mu}, t)$ in an air parcel is given by:

$$\begin{aligned}\frac{\partial n(\vec{\mu}, t)}{\partial t} = & \underbrace{\frac{1}{2} \int_0^{\mu_1} \int_0^{\mu_2} ... \int_0^{\mu_A} K(\vec{\mu} - \mu', \mu') n(\vec{\mu} - \mu', \vec{\mu}, t) n(\vec{\mu}', t) d\mu'_1 d\mu'_2 ... d\mu'_A}_{\text{coagulation gain}} \\ & \underbrace{- n(\vec{\mu}, t) \int_0^{\mu_1} \int_0^{\mu_2} ... \int_0^{\mu_A} K(\vec{\mu}, \vec{\mu}') n(\vec{\mu}', t) d\mu'_1 d\mu'_2 ... d\mu'_A}_{\text{coagulation loss}} \underbrace{- \sum_{k=1}^{A} \frac{\partial}{\partial \mu_k} \left[c_k I_k(\vec{\mu}, \vec{g}, t) n(\vec{\mu}, t) \right]}_{\text{gas-particle mass transfer}} \\ & \underbrace{+ \dot{n}_{\text{emit}}(\vec{\mu}, t)}_{\text{emission}} \underbrace{+ \dot{n}_{\text{nuc}}(\vec{\mu}, t)}_{\text{nucleation}} \underbrace{+ \lambda_{\text{dil}} \big(n_{\text{back}}(\vec{\mu}, t) - n(\vec{\mu}, t) \big)}_{\text{dilution}} \underbrace{+ \frac{1}{\rho_{\text{dry}}(t)} \frac{d\rho_{\text{dry}}(t)}{dt} n(\vec{\mu}, t)}_{\text{air density change}} .\end{aligned} \tag{3.2}$$

As particles interact with each other and the environment, the distribution in per-particle composition $\hat{\mu}$ changes. For example, if a particle having composition $\hat{\mu}$ coagulates with another particles, the new particle takes on a different composition and $n(\hat{\mu})$ decreases (coagulation loss). On the other hand, if a particle having composition $\hat{\mu}$ forms through the combination of two particles through coagulation, $n(\hat{\mu})$ increases (coagulation gain). In the simulations described in this proposal, particles coagulate through Brownian motion, so the probability of coagulation events depends on each particles' respective size, which can be determined from μ.

Particles grow by condensation or shrink by evaporation of semi-volatile substances, which depends on the mass condensation rate $I_k(\vec{\mu}, \vec{g}, t)$ of each species $k = 1, ..., A$. Gas-aerosol mass transfer, through condensation, evaporation or new particle formation, depends on the particular distribution $n(\hat{\mu})$ and the concentration of semi-volatile gases. Nucleation is not included in the model simulations described in this study. MOSAIC simulates mass transfer between gas-phase components and aerosol particles through deterministic equations that describe chemical equilibria and gas- and aerosol-phase thermodynamics.

The continuity equation describing the evolution of the aerosol mixing state (Equation 3.2 could be solved

deterministically by binning particles in composition space and tracking the evolution an A-dimensional distribution, where $A = 20$ aerosol species in the model simulations described in this dissertation. Equation 3.2 could also be solved using a particle-based method, where the model simulates stochastic interactions between thousands of particles in the A-dimensional distribution. If the number of simulated particles is large enough, the collection of discrete particles can be used to reconstruct the A-dimensional number density distribution $n(\hat{\mu})$.

As the simulation proceeds, the particle population simulated by PartMC-MOSAIC is altered in two ways. First, each particle's mass composition evolves continuously by condensation and evaporation of semi-volatile substances, processes that are simulated deterministically by MOSAIC. MOSAIC includes modules for gas-phase photochemistry (154), particle-phase thermodynamics (152; 153), and gas-particle mass transfer (151). The coupled model treats all atmospherically important aerosol species including sulfate (SO_4^{2-}), nitrate (NO_3^-), chloride (Cl^-), carbonate (CO_3^{2-}), ammonium (NH_4^+), sodium (Na^+), calcium (Ca^+), methanesulfonic acid (MSA), black carbon (BC), primary organic aerosol (POA), and a number of secondary organic aerosol (SOA) species.

Second, particles are added to and removed from the simulation through aerosol emissions, dilution with background air, and coagulation events, processes that are simulated stochastically by PartMC. PartMC also tracks the source from which each particle originated. If two particles coagulate, the model stores the number of particles originating from each source that are contained within the combined particle. In this work, we pay special attention to the evolution of particles that contain at least one particle originating from diesel exhaust. A detailed model description can be found in (115). PartMC Version 2.1.4 was used to generate the results in this dissertation.

3.2 Computing climate-relevant properties from particle-resolved model output

The bulk properties of aerosol populations depend on the characteristics of individual particles that make up that population. While other aerosol schemes simplify the representation of particle size and composition, PartMC-MOSAIC tracks the composition of each simulated particle. Therefore, climate-relevant properties of aerosol populations can be computed explicitly by modeling relevant properties of individual particles.

This section describes models for predicting cloud condensation nuclei activation, water uptake, and optical properties of individual aerosol particles, demonstrating that climate-relevant aerosol properties depend strongly on size and chemical composition. Although atmospheric particles exist in a variety of shapes

and have complex internal morphology, aerosol microphysical schemes are unable to track particle shape or particles' internal structure as they evolve in the atmosphere. Instead, aerosol microphysical schemes assume particles are spherical with a simplified internal morphology. We follow this approach, treating particles as homogeneous spheres when modeling hygroscopic growth, CCN activity, absorption and scattering, focusing instead on the representation of particle size and composition. To model absorption by BC-containing particles, we assumed that particles contained one or more BC inclusions within an otherwise homogeneous particle, again assuming the overall particle and the inclusions are spherical.

3.2.1 Cloud condensation nuclei activation

The cloud condensation nuclei (CCN) activity of an aerosol population is a key determinant in aerosol indirect effects. Increases in the number concentration of CCN, N_{CCN}, affects cloud albedo and lifetime, as described in Section 1.3.2. At a specific environmental supersaturation, N_{CCN} depends on the aerosol size distribution, mixing state, and number concentration.

A particle's ability to activate cloud droplet formation depends on its dry diameter $D_{\mathrm{dry},i}$ and its hygroscopicity parameter κ_i. The environmental saturation ratio S_i is the ratio between the environmental vapor pressure and the equilibrium vapor pressure for the particular environmental conditions. For each particle i, the equilibrium saturation ratio S_i over an aqueous droplet of diameter D_i is the environmental saturation ratio at which a the droplet and the environment are at equilibrium. The saturation ratio S_i is modeled as a combination of the Raoult and Kelvin effects:

$$S_i(D_i) = \underbrace{a_{\mathrm{w},i}(D_i)}_{\substack{\text{Raoult}\\ \text{term}}} \underbrace{K_i(D_i)}_{\substack{\text{Kelvin}\\ \text{term}}}, \tag{3.3}$$

where $a_{\mathrm{w},i}$ is the water activity of the droplet solution, which depends on the droplet composition, and $K_i(D_i)$ is the Kelvin effect term, which depends on the droplet wet diameter D_i.

The Kelvin effect is modeled as:

$$K_i(D_i) = \exp\left(\frac{4M_{\mathrm{sol}}\sigma_{\mathrm{sol}}}{RT\rho_{\mathrm{sol}}D_i}\right), \tag{3.4}$$

where M_{sol} is the molecular weight of the droplet solution, σ_{sol} is the surface tension over the droplet solution, ρ_{sol} is the density of the solution, R is the universal gas constant, and T is the ambient temperature. We model the Kelvin effect assuming M_{sol}, σ_{sol}, and ρ_{sol} are those of water.

Applying the hygroscopicity parameter for each particle κ_i, the water activity $a_{\mathrm{w},i}$ is expressed a function

of particle wet diameter D_i and dry diameter $D_{\mathrm{dry},i}$, as describe in (104):

$$\frac{1}{a_{\mathrm{w},i}} = 1 + \kappa_i \frac{D_{\mathrm{dry},i}^3}{D_i^3 - D_{\mathrm{dry},i}^3}. \tag{3.5}$$

They hygroscopicity parameter κ_k has been derived empirically different aerosol species $k = 1, ..., A$, as given in Table 3.1. The effective hygroscopicity parameter each particle is given as the volume-weighted average of κ_k for each constituent species:

$$\kappa_i = \sum_{k=1}^{A} \epsilon_{k,i} \kappa_k. \tag{3.6}$$

All other factors being equal, particles with a greater κ_i are more hygroscopic and more easily activated. The parameter κ has been determined empirically for a number of aerosol species (Table 3.1), and the effective hygroscopicity parameter κ_i for each particle is the volume-weighted average of κ for its constituent aerosol species.

From (77; 104), the saturation ratio S_i is then modeled as:

$$S_i(D_i) = \frac{D_i^3 - D_{\mathrm{dry},i}^3}{D_i^3 - D_{\mathrm{dry},i}^3(1 - \kappa_i)} \exp\left(\frac{4\sigma_{\mathrm{w}} M_{\mathrm{w}}}{RT\rho_{\mathrm{w}} D_i}\right). \tag{3.7}$$

We apply this model to determine the environmental supersaturation needed to activate a particle for cloud formation. If a particle grows to some critical wet diameter ($D_{\mathrm{c},i}$), it will continue to grow without bound at that supersaturation and is said to be "activated". We denote the critical saturation ratio at which a particle activates and forms a cloud droplet with $S_{\mathrm{c},i} = S_i(D_{\mathrm{c},i})$ and the critical supersaturation as $s_{\mathrm{c},i} = \big(S_{\mathrm{c},i} - 1\big) \times 100$. Particle are CCN-active if their critical supersaturation is lower than the environmental supersaturation, and the critical supersaturation is computed by solving the non-linear equation for $\partial S_i(D_i)/\partial D_i = 0$. The number concentration of CCN, N_{CCN} is then computed by counting the number of particles per volume that have critical supersaturation $s_{\mathrm{c},i}$ lower than the environmental supersaturation s.

3.2.2 Hygroscopic growth

Water uptake in sub-saturated air was modeled using κ-Köhler theory. MOSAIC also simulates water uptake, which is used for model's simulation of chemistry and coagulation. However, in the studies described in this dissertation, it is useful to evaluate water uptake by a specific particle or specific particle population as a function of relative humidity. Rather then repeating the same simulation at multiple relative humidity levels, κ-Köhler theory was used to model water uptake as a post-processing step for the populations simulated

Table 3.1: Properties assigned to aerosol species. Values for density and refractive index are the same as those assumed in Zaveri et al. (155). The range in values for κ were chosen based on (104) and references therein.

aerosol species	density [kg m^{-3}]	κ	refractive index at $\lambda = 550$ nm
NO_3	1800	0.65	1.5
SO_4	1800	0.65	1.5
NH_4	1800	0.65	1.5
SOA	1400	0.1	1.45
BC	1800	0	1.82 + 0.74i
POA	1000	0.001	1.45
H_2O	1000		1.33

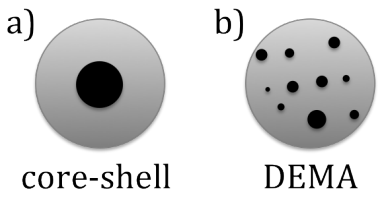

Figure 3.1:

by PartMC-MOSAIC. From Petters and Kreidenweis (104), the wet diameter for a particle with a given dry diameter $D_{\mathrm{dry},i}$ and hygroscopicity parameter κ_i is computed for relative humidity (RH) below 100% as follows:

$$\frac{\mathrm{RH}}{\exp\left(\frac{A}{D_i}\right)} = \frac{D_i^3 - D_{\mathrm{dry},i}^3}{D_i^3 - D_{\mathrm{dry},i}^3(1-\kappa_i)}. \tag{3.8}$$

In this dissertation, the amount of water contained in each particle is used to model absorption and scattering as a function of relative humidity.

3.2.3 Aerosol optical properties

Direct radiative forcing by aerosols depends on the ability of aerosol populations to absorb and scatter solar radiation. The scattering cross section $\sigma_{\mathrm{scat},i}$ for a particle i indicates the likelihood of light being scattered by a particle, and depends on the wavelength of light λ. The scattering cross section $b_{\mathrm{scat}}(\lambda)$ is given by the sum over $\sigma_{\mathrm{scat},i}$ for all particles $i = 1, .., N$ per unit volume V that the particles occupy:

$$b_{\mathrm{scat}}(\lambda) = \frac{\sum_{i=1}^{N} \sigma_{\mathrm{scat,i}}(\lambda)}{V} \tag{3.9}$$

Similarly, the absorption coefficient $b_{\mathrm{abs}}(\lambda)$ is the sum over the per-particle absorption cross section $\sigma_{\mathrm{abs},i}(\lambda)$ per unit volume:

$$b_{\mathrm{abs}}(\lambda) = \frac{\sum_{i=1}^{N} \sigma_{\mathrm{abs,i}}(\lambda)}{V} \tag{3.10}$$

Values for $\sigma_{\mathrm{abs},i}$ and $\sigma_{\mathrm{scat},i}$ depend on the morphology of individual particles, quantities that are difficult to represent in models. Existing aerosol models assume simple representations of particle morphology, typically treating particles as homogeneous spheres or as containing a single insoluble core with a uniform coating, known as the core-shell approximation (Figure 3.1a). Optical properties for particles with complex shape can be computed for individual particles (2), but the evolution of particle configuration cannot yet be tracked in chemical transport models. In this proposal, we modeled particles using the dynamic effective medium approximation (31; 63), referred to as DEMA (Figure 3.1b). Under this approximation, each particle is assumed to contain one or more randomly-distributed BC inclusions. In order to apply this model, the number of inclusions must also be tracked, in addition to particle size and composition.

DEMA is used to determine the effective refractive index of particles containing on or more black carbon inclusions. The effective complex refractive index $m = n + ik$ is given by the square root of the effective emissivity ϵ, where ϵ is computed from the following non-linear equation:

$$\left(1 - \frac{v_{\mathrm{c}}}{v}\right)\frac{\epsilon_{\mathrm{s}} - \epsilon}{\epsilon_{\mathrm{s}} - 2\epsilon} + \frac{v_{\mathrm{c}}}{v}\frac{\epsilon_{\mathrm{c}} - \epsilon}{\epsilon_{\mathrm{c}} - 2\epsilon} + \frac{2\pi}{45}\left(\frac{\omega}{c}\right)^2(\epsilon_{\mathrm{c}} - \epsilon)\left[1 + \frac{5\epsilon}{2\epsilon_{\mathrm{c}} + 3\epsilon} + \frac{18\epsilon(\epsilon_{\mathrm{c}} - 2\epsilon)}{(\epsilon_{\mathrm{c}} + 2\epsilon)^2}\right]\int r^5 n(r)dr = 0\ . \quad (3.11)$$

Once the effective refractive index for each particle is known, the absorption cross section $\sigma_{\mathrm{abs},i}$ is modeled using Mie theory. Mie theory describes absorption and scattering by electromagnetic radiation within a spherical particle (13). The refractive index of a particle that does not contain any absorbing material is computed the volume-weighted average of the refractive indices of its constituent aerosol species.

3.3 Connecting particle-level and population-level models

In the studies described in this dissertation, findings from the particle-resolved model are interpreted to improve aerosol representations in large-scale chemical transport models. Specifically, PartMC-MOSAIC is used to identify variables that most affect aerosol processes and properties, to quantify error in approximate representations of the aerosol mixing state, and to develop parameterizations intended to improve simulations by simpler aerosol schemes. This section describes the ways that I have analyzed particle-resolved model findings to evaluate and improve less detailed aerosol models.

3.3.1 Sensitivity analysis

Many of the analysis techniques described in this dissertation involve simulating a series of sensitivity simulations. In some cases, I evaluate the sensitivity of a given property to a single variable. For example,

Chapter 4 describes an analysis evaluating the sensitivity of CCN activity by particle from diesel exhaust, after aging in the atmosphere, to their size and composition at emission. The sensitivity to the assumed size distribution and to the assumed composition are each evaluated independently.

In other studies, I apply techniques to identify the variables that most influence a specific depend variable under a range of atmospheric conditions. For example, Chapter 5 describes a regression analysis to identify the independent variables that most affect changes in CCN activation by BC-containing particles. In this study, I varied multiple independent variables, exploring all combinations of input parameters. In studies that explore even more independent variables (Chapters 6 and 8), I sampled the independent variable space using latin hypercube sampling. Latin hypercube sampling is a method for generating a representative set of parameter values from a much large collection of parameter combinations. In the modeling studies described in this dissertation, processes may be sensitive to a large number of independent variables. Assigning only the range over which each parameter is to be varied and the number of total simulations, Latin hypercube sampling produces a small number of simulations from the variable space. The goal of this type of sampling approach is to reduce the overall number of simulations, while still varying a large number of input parameters.

3.3.2 Error estimation

Chapters 8 describes an analysis of error from approximate representations of aerosol composition, where error is defined as the difference between the approximate mixing state representation and the benchmark particle-resolved representation. Similarly, Chapter 7 evaluates the error in modeled absorption by BC if the representation of particle composition is simplified or if water uptake is neglected.

In this dissertation, differences are quantified using the normalized mean factor bias or the normalized mean factor error, as described in Yu et al. (150). In both cases, the prediction $\hat{Y}$ is compared with the "true" value Y. The normalized mean factor bias is given by:

$$\text{Normalized mean factor bias} = \frac{\sum_{i=1}^{n}(\hat{Y}_i - Y_i)}{\sum_{i=1}^{n} Y_i} \tag{3.12}$$

where Y_i is the prediction of some dependent variable for data set i using one approach and $\hat{Y}_i$ is the prediction of the same independent variable for the same data set using a different approach. In one study describe here, Y represents predictions using a benchmark approach, the particle-resolved model, and $\hat{Y}$ represents predictions using an approximate approach, and ϵ_Y can be interpreted as a mean error from the approximation. In other cases, Y is not assumed to be a more accurate prediction than $\hat{Y}$, and ϵ_Y represents

only a mean difference between the two quantities.

The normalized mean bias indicates whether the prediction $\hat{Y}$ overestimates or underestimates Y, but does not indicate the overall magnitude of error. For this reason, the normalized mean factor error is presented, in addition to the mean bias, where the normalized mean factor error is defined as:

$$\text{Normalized mean factor bias} = \frac{\sum_{i=1}^{n} |\hat{Y}_i - Y_i|}{\sum_{i=1}^{n} Y_i} \tag{3.13}$$

where $\bar{Y}$ is the mean across all values Y_i.

This study also involves several applications of regression analysis, which are described in the next sections. Agreement between relationships generated through parametric and nonparametric regression were evaluated using the coefficient of determination R^2:

$$R^2(s) = 1 - \frac{\sum_{i=1}^{N_{\text{test}}} \left(Y_i - \hat{Y}_i\right)^2}{\sum_{i=1}^{N_{\text{test}}} \left(Y_i - \bar{Y}_i\right)^2}. \tag{3.14}$$

3.3.3 Identification of governing independent variables

In this dissertation, nonparametric regression analysis was applied to identify the combination of independent variables that most affect specific aerosol processes and properties. Using this approach, I identified the environmental conditions that most affect the timescale for BC-containing particle to age by condensation and coagulation (Chapter 5) and the bulk aerosol properties that most affect BC's light absorption. In the nonparametric regression analyses described here and the parametric regression analyses described in the next section, regression data was separated into testing and training sets to prevent over fitting the data. The procedure for applying nonparametric regression to identify governing variables is as follows: 1) select a set of candidate variables to test, 2) perform the regression on data in the training set to predict the dependent variable as a function of the candidate dependent variables, and 3) evaluate the prediction using the data in the testing set. The combination of independent variables that most affect the value of the dependent variable are identified from the regression that yields the greatest value for R^2.

3.3.4 Parameterization development

I show that, in some cases, aerosol properties simulated by the particle-resolved model can be represented through simple parameterizations that are suitable for global models. Based on the variables identified

through nonparametric regression, I constructed parameterizations according to a particular functional form. The parametric relationships were developed based on linear or nonlinear regression of model data in the training set. The parameterizations were then evaluated with R^2, using data from the testing set.

Chapter 4

Sensitivity of CCN activity to particle characteristics at emission

4.1 Introduction

This study falls under the broad objective to improve the scientific understanding of the factors that influence aerosol aging. In this case, I focus on aging with respect to changes in the cloud condensation nuclei activity of primary aerosol, in general. BC-containing particles are one type of primary particles. Primary particles are especially important in determining the aerosol number budget (22; 129; 112) and the associated increase in CCN concentrations (106; 128). Although many of the microphysical properties governing CCN activity have been identified, there remains a lack of quantitative connection between particles as emitted and their ultimate effect on CCN concentrations. In particular, a deeper understanding of the rates and dominant factors governing transition between fresh emissions and CCN-active particles would enable effective parameterizations for global models. This work evaluates the sensitivity of primary particles' CCN activity to their size and composition at emission, and we evaluate how this sensitivity depends on the cloud supersaturation level and aging conditions near the emission source. We focus on particles emitted from a particular source, diesel engines, because they represent an important number fraction of particle emissions (83) and because their CCN activity is important to understand their net forcing (132; 23). The lessons drawn from this particle type are also applicable to other hydrophobic primary aerosols.

Modeling studies at the global scale show that carbonaceous aerosols have a strong influence on cloud radiative properties (23; 8; 57; 128; 75) and that assumptions about particle characteristics at emission are a key uncertainty (8; 128; 75). For example, (75) compared the cloud radiative effects of fossil fuel and biomass burning aerosol emissions in six global models. On average, cloud microphysical effects led to a negative forcing approximately equal in magnitude but opposite in sign to the direct forcing by particles emitted from these sources. Biomass burning aerosol exerted a more negative indirect forcing than aerosol emissions from fossil fuels, which the authors attributed in part to differences in the microphysical properties of particles originating from these two sources. In these studies, biomass burning particles were initially more hygroscopic than fossil fuel particles, and, in some cases, biomass burning particles were emitted with a larger

mean diameter. However, the geographic distribution of particle emissions also differs for biomass and fossil fuel sources. Cloud responses to particle emissions vary regionally because of variation in environmental conditions, so it is unclear whether differences in cloud response from biomass and fossil fuel emissions are caused by differences in particle microphysical properties or by differences in the regional distribution of each source.

These global modeling studies included a number of cloud processes and were conducted on large spatial scales, with only a limited representation of aerosol properties, so these studies have not isolated the factors to which cloud-aerosol interactions are most sensitive. In this work, we complement the broad findings of global models by simulating the evolution of aerosols near the emission source using a detailed aerosol model that resolves the composition of each simulated particle. This work evaluates how aging conditions and environmental supersaturation levels affect the relationship between primary aerosol emissions and the number concentration of atmospheric CCN. We examine how two important aging processes, condensation and coagulation, affect the CCN activity of primary particles as a function of time after emission. The relative impact of these processes depends on particle size and composition, and we elucidate this behavior with sensitivity studies. The results of this sensitivity analysis can be used to identify the degree of detail in particulate emission properties required to predict CCN activity. In addition, this analysis will lead to a mechanistic understanding of how emissions affect CCN, cloud droplet number, and, ultimately, cloud forcing.

Most of this chapter was published as a manuscript in the Journal of Geophysical Research (45).

4.2 Simulation of urban plume with particle-resolved model

We simulate aerosol aging with a detailed aerosol microphysical model to evaluate how particle characteristics at emission and environmental conditions near the emission source influence CCN concentrations and aerosol removal by nucleation scavenging. We considered three factors:

1. size and composition of freshly emitted particles,
2. conditions for aging by condensation and coagulation near the emission source, and
3. water vapor supersaturation at which CCN activity is evaluated.

PartMC-MOSAIC (151; 115), as described in Chapter 3, was used to simulate a series of scenarios of an air parcel advected. In each case, the air parcel is advocated through a large urban area based on the idealized plume scenario described in (115), with conditions similar to Los Angeles. The simulations started

Table 4.1: Aerosol Emissions and Initial Conditions for Base Case Simulation (115). The quantity κ_{emit} is the hygroscopicity parameter assigned to particles at emission.

Initial/Background	N (m^{-3})	D_{gm} (μm)	σ_{g}	Composition by Mass	κ
Aitken Mode	3.2×10^9	0.02	1.45	50% $(NH_4)_2SO_4$, 50% POA	0.325
Accumulation Mode	2.9×10^9	0.116	1.65	50% $(NH_4)_2SO_4$, 50% POA	0.325
Emissions	$\dot{N}_{\text{emit}}$ ($\text{m}^{-2}\text{s}^{-1}$)	$D_{\text{gm,emit}}$ (μm)	σ_{g}	Composition by Mass	κ_{emit}
Meat cooking	9×10^6	0.0865	1.9	100% POA	0.001
Diesel vehicles	1.6×10^8	0.05	1.7	30% POA, 70% BC	3×10^{-4}
Gasoline vehicles	5×10^7	0.05	1.7	80% POA, 20%BC	8×10^{-4}

at 6:00 am, at which time the parcel contained only background gas and aerosol, and received gas and aerosol emissions from 6:00 am until 6:00 pm. After 6:00 pm, all emissions were discontinued until the simulation ended at 6:00 am the following morning. The parcel was mixed with background air according to a fixed dilution rate, and the temperature and mixing height varied according to a prescribed diurnal profile. The relative humidity varied as a function of temperature. The temperature peaked at 300 K in the middle afternoon, corresponding to a minimum relative humidity of 55%. At night the temperature decreased to 290 K, and the relative humidity increased to 95%. Time series for selected trace gases and meteorologic conditions are given in (115).

The size distribution and composition assigned to background and emitted particles in the baseline scenario are given in Table 5.1, including number-based geometric mean diameter ($D_{\text{gm,emit}}$) and standard deviation ($\sigma_{\text{g,emit}}$), the mass composition, and the effective hygroscopicity parameter (κ_{emit}) corresponding to that composition. The background aerosol consisted of Aitken and accumulation modes and was composed of $(NH_4)_2SO_4$ and POA. Three sources of carbonaceous aerosols were emitted: (1) diesel vehicle emissions, (2) gasoline vehicle emissions, (3) and meat cooking emissions. Although particles from diesel exhaust are the focus of this study, the other two sources were included to simulate a more realistic composition of urban aerosol. In this base case scenario, the number-based emission strength from diesel particulate emissions far exceeded number-based emission from any other source (Table 5.1). The size distribution parameters and composition of particle emissions were based on measurements from (72), (73), and (40), respectively. The initial gas concentrations and gas emissions were adapted from the southern California Air Quality Study of (151). This plume scenario is not meant to represent any particular episode but was chosen to analyze changes in the aerosol mixing state under conditions simple enough that the dominant aging processes could be understood.

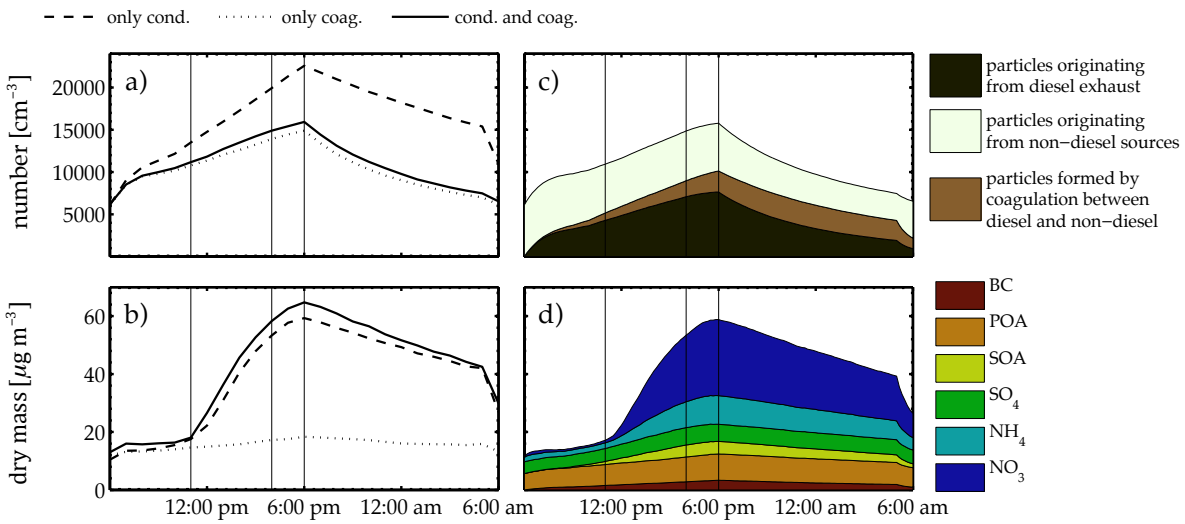

Figure 4.1: Evolution of (a) overall aerosol number concentration and (b) overall aerosol mass concentration for simulations representing different processes and, for only the simulation including both condensation and coagulation, the evolution of (c) aerosol number different classes of particles and (d) mass of aerosol species. Vertical lines show the time periods outlined in Table 4.2.

4.3 Evolution of CCN activity in a single emission scenario

We first present results from a baseline emission scenario in order to illustrate the distinct roles of condensation and coagulation in altering the hygroscopic properties of particle emissions. Later, we show how differences in particle characteristics at emission influence their CCN activity after hours of aging. We determined the relative impact of each aging mechanism by comparing simulations under three limiting cases: 1) including condensation without coagulation, 2) including coagulation without condensation, and 3) including both condensation and coagulation. We then build on this analysis in Section 4.4.1 to determine how each aging mechanism alters the sensitivity of CCN activity to the characteristics of primary aerosol at emission.

The temporal evolution of the aerosol number concentration and dry mass concentration is shown in Figures 4.1.a and 4.1.b, respectively, for each set of aging conditions. The particle number concentration changed by primary aerosol emissions, dilution with background air, and coagulation. Aerosol emissions and dilution also affect the aerosol mass concentration, which also evolves by condensation and evaporation of semi-volatile substances. These processes all vary throughout the day.

The diurnal variation in aging conditions consisted of four key time periods, which are outlined in Table 4.2. Early in the simulation (6:00 am–11:00 am), particle emissions caused an increase in the number concentration and freshly emitted particles aged primarily by coagulation. The middle of the day (11:00 am–4:00 pm) was characterized by rapid condensation of ammonium nitrate, produced through photochemical

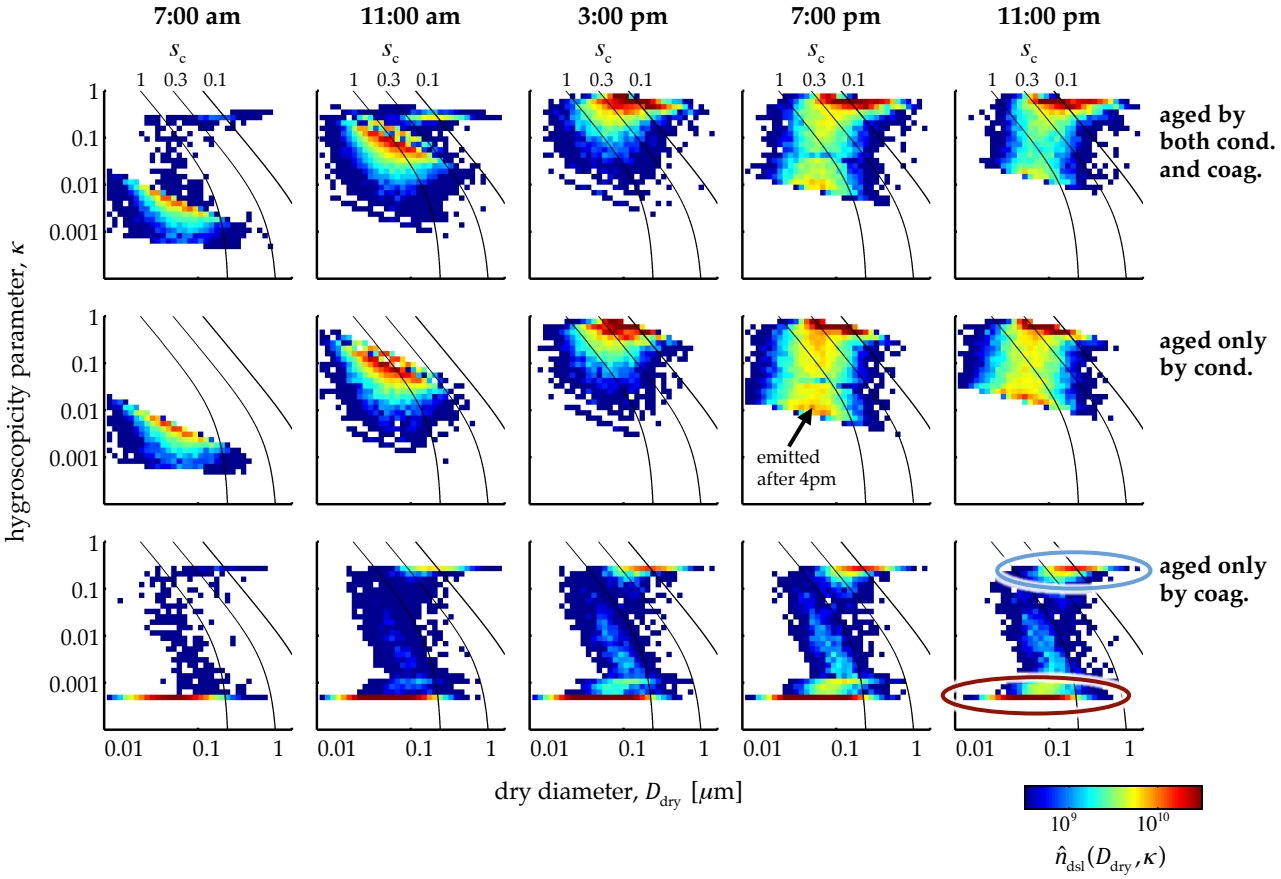

Figure 4.2: Two-dimensional normalized number distribution of diesel particles $\hat{n}_{\mathrm{dsl}}(D_{\mathrm{dry}}, \kappa)$ shows how changes in size and hygroscopicity affect particles' critical supersaturation s_{c} (indicated by superimposed lines). The contribution of each aging mechanism to the full simulation (top row) is shown through comparisons between rows. The majority of particles acquire hygroscopic coating by condensation (middle row), but some are instantaneously encompassed in CCN-active particles through coagulation events (indicated by the blue circle). In the absence of condensation (bottom row), many particles remain unmodified throughout the simulation (indicated by the red circle). See Section 4.3.1 for further explanation.

reactions. Particles emitted after this period of rapid aging by condensation, but before emissions ceased, (4:00 pm–6:00 pm) did not experience rapid aging by condensation, so they remained hydrophobic unless they participated in a coagulation event. Dilution and coagulation were the dominant processes acting at night (6:00 pm–6:00 am), after emissions were discontinued and at a time when aging by condensation was slow.

In this scenario, particles originating from diesel exhaust contributed a large fraction of the aerosol number concentration, shown in Figure 4.1.c. The total number concentration is separated into three classes: 1) particles formed by coagulation between particles originating from diesel exhaust and particles originating from non-diesel sources, 2) particles emitted from diesel exhaust that had not coagulated with particles from other sources, and 3) particles originating from non-diesel sources that had not coagulated with particles from diesel exhaust. Categories 1 and 2 demonstrate how diesel particles influence the particle population and are the focus of this work. We refer to particles in categories 1 and 2 as "diesel particles", meaning particles that contain at least one particle originating from diesel exhaust. Note that category 1 includes only particles formed by inter-coagulation between particles from diesel and non-diesel sources, so particles formed by coagulation between two particles from diesel exhaust are placed in category 2 and those formed by coagulation between particles from the background or non-diesel emission sources are placed in category 3.

The mass concentration increased by approximately 50% from 6:00 am until 6:00 pm because of primary particle emissions (BC and POA), shown in Figure 4.1.d. The urban area simulated in this study contained high concentrations of nitric acid and ammonia, an average of 12 ppb and 1.7 ppb, respectively, leading to rapid formation of ammonium nitrate in simulations that include condensation. The aerosol mass concentration increased by more than a factor of three during the afternoon if condensation was simulated, from approximately 20 μg m^{-3} at 12:00 pm to approximately 70 μg m^{-3} at 6:00 pm. Therefore, although coagulation was a key process influencing the aerosol number concentration, condensation was the most important process influencing the aerosol mass concentration. Beyond the 24 hours, the number concentration was a factor of two greater when coagulation was not simulated (dashed line), and the mass concentration was underestimated by a factor of two at this time when condensation was neglected (dotted line).

4.3.1 Susceptibility to nucleation scavenging as a function of supersaturation

Changes in particle characteristics that influence CCN activity are shown through a series of probability density distributions in Figure 4.2. The effective hygroscopicity parameter and critical supersaturation are computed according to the approach described in Section 3.2.1. At each time, the normalized two-

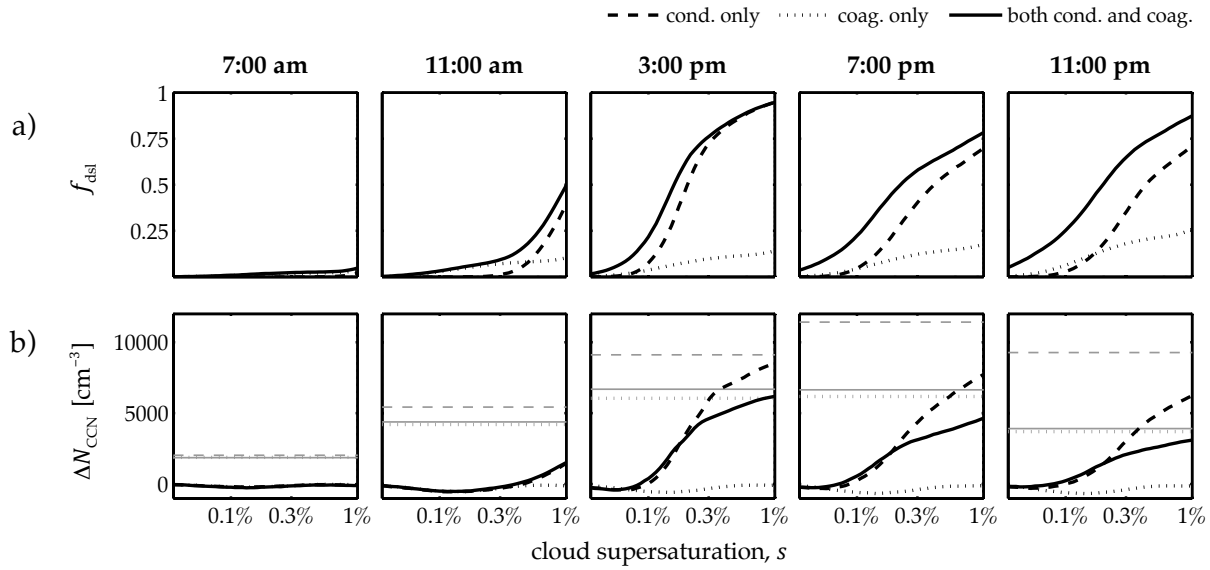

Figure 4.3: Evolution of (a) number fraction of diesel particles susceptible to nucleation scavenging, f_{dsl}, and (b) difference in CCN concentrations between simulations with and without diesel emissions, ΔN_{CCN}. The change in number concentration is indicated by the horizontal grey lines in Figure 4.3.b

Table 4.2: Time periods representing aging regimes

time	characteristics
6:00 am–11:00 am	fresh particle emissions, slow aging by condensation
11:00 am–4:00 pm	fresh particle emissions, rapid aging by condensation of ammonium nitrate
4:00 pm–6:00 pm	fresh particle emissions continue after condensational aging slows
6:00 pm–6:00 am	no particle emissions, slow aging by condensation

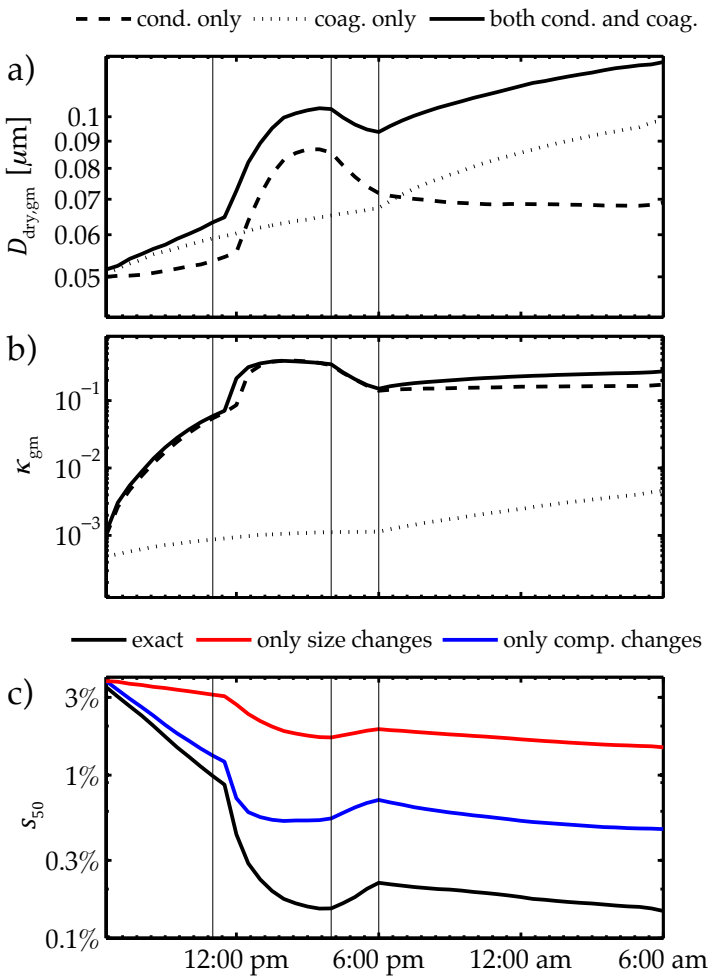

Figure 4.4: For each set of aging conditions, evolution of diesel particles' (a) geometric mean diameter and (b) geometric mean hygroscopicity parameter. For simulations including both condensation and coagulation, evolution of (c) supersaturation at which 50% of diesel particles become CCN active for exact PartMC-MOSAIC results (black line), assuming particles size changes but not their composition (red line), and assuming their composition changes but not their size (blue line). Vertical lines show the time periods outlined in Table 4.2.

dimensional distribution $\hat{n}_{\mathrm{dsl}}(D_{\mathrm{dry}}, \kappa)$ is shown for each set of aging conditions. The unnormalized distribution $n_{\mathrm{dsl}}(D_{\mathrm{dry}}, \kappa)$ is defined as:

$$n_{\mathrm{dsl}}(D_{\mathrm{dry}}, \kappa) = \frac{\partial^2 N_{\mathrm{dsl}}(D_{\mathrm{dry}}, \kappa)}{\partial \log D_{\mathrm{dry}} \partial \log \kappa}, \tag{4.1}$$

where $N_{\mathrm{dsl}}(D_{\mathrm{dry}}, \kappa)$ is the cumulative number distribution with respect to D_{dry} and κ. Because we compare particle populations with very different number concentrations, it is useful to use the normalized number distribution $\hat{n}_{\mathrm{dsl}}(D_{\mathrm{dry}}, \kappa)$:

$$\hat{n}_{\mathrm{dsl}}(D_{\mathrm{dry}}, \kappa) = \frac{n_{\mathrm{dsl}}(D_{\mathrm{dry}}, \kappa)}{\int_{-\infty}^{\infty} \int_{-\infty}^{\infty} n_{\mathrm{dsl}}.(D_{\mathrm{dry}}, \kappa) d \log D_{\mathrm{dry}} d \log \kappa} \tag{4.2}$$

The individual contributions of condensation and coagulation are shown through comparisons between the simulation that includes both aging mechanisms (top row of Figure 4.2) and simulations in which each mechanism operated alone (middle and bottom rows of Figure 4.2). The state of diesel particles is shown every four hours from 7:00 am until 11:00 pm. The selected times were chosen to show how particle properties change during the key time periods outlined in Table 4.2.

Curves of constant s_{c} for T =293.15 K are plotted as a function of D_{dry} and κ in Figure 4.2. Particles that would be CCN-active at a specified supersaturation s are those with $s_{\mathrm{c},i} \leq s$. Crossing the lines of constant s_{c} from left to right means particles transition from CCN-inactive to CCN-active at that s. For the particle concentrations simulated in this paper, a cloud supersaturation of $s = 0.1\%$ is consistent with updraft velocities of 0.2–0.5 m s^{-1} (stratus clouds), and $s = 0.6\%$ is consistent with updraft velocities of 2–5 m s^{-1} (convective clouds).

Each aging mechanism caused the evolution of the particle population to proceed in a different way. An hour after emissions started (7:00 am), most diesel particles were too small and hydrophobic to activate at any $s < 1\%$. When particles aged only by condensation, $D_{\mathrm{dry},i}$ and κ_i increased incrementally over time as particles accumulated secondary aerosol coating, shown in the middle row of Figure 4.2. Photochemical production of secondary aerosol between 11:00 am and 4:00 pm caused rapid condensational aging during these hours. Particles emitted after 4:00 pm did not experience this rapid daytime aging and, consequently, remained small and hydrophobic with high values for $s_{\mathrm{c},i}$ throughout the night, shown in the middle row of Figure 4.2.

Without condensation $D_{\mathrm{dry},i}$ and κ_i were altered only for particles that participated in coagulation events, shown in the bottom row of Figure 4.2. Because we assume that particles coagulate by Brownian motion, coagulation events were most likely between the largest and smallest particles in the distribution. The smallest of the diesel particles were often incorporated into much larger background particles through such

coagulation events, forming a mode of diesel particles with κ_i approximately the same as the background (blue circle in Figure 4.2). These combined particles were often CCN-active at low values of s, enabling the removal of the small diesel particle contained in the combined particle through nucleation scavenging. The particles that did not participate in coagulation events maintained their initial hygroscopic properties throughout the simulation, shown by the mode of particles in the bottom row of Figure 4.2 that maintain $\kappa = 3 \times 10^{-4}$ throughout the entire simulation (red circle in Figure 4.2).

As particles increase in size (greater $D_{\mathrm{dry},i}$) and hygroscopicity (greater κ_i), they become more susceptible to CCN activation and wet removal. The number fraction of diesel particles that are able to activate into CCN (f_{dsl}) is shown as a function of cloud supersaturation in Figure 4.3.a. The value of $f_{\mathrm{dsl}}(s)$ at a specific s is the portion of particles with $s_{\mathrm{c}} \leq s$, corresponding to particles above that s_{c} line in Figure 4.2. Because f_{dsl} is related to the time-dependent number concentration of diesel particles, the same value of f_{dsl} at different times could have a very different effect on the number concentration of CCN.

Freshly emitted particles were CCN-active only at very high supersaturation levels ($s > 1\%$), but their CCN activity increased as they aged by condensation and coagulation. Condensation of semi-volatile substances between 11:00 am and 3:00 pm caused $s_{\mathrm{c},i}$ to decrease for all diesel particles (Figure 4.2), enabling their activation and removal under a greater range of cloud supersaturation levels. For simplicity, we discuss changes in the f_{dsl} spectrum using a single value, the supersaturation required to activate 50% of particles (s_{50}). While f_{dsl} at a specific time and supersaturation indicates the portion of particles that could be removed at that supersaturation (Figure 4.3.a), the quantity s_{50} provides information on the f_{dsl} curve with only a single value by indicating the supersaturation level needed to activate most of the diesel particles. In simulations including condensation alone (dashed lines) s_{50} decreased from $s_{50} \approx 1\%$ at 11:00 am to $s_{50} \approx 0.3\%$ at 3:00 pm. On the other hand, a small portion of diesel particles combined with hygroscopic particles through coagulation events, increasing $f_{\mathrm{dsl}}(s)$ at $0.1\% < s < 1\%$ in simulations including coagulation without condensation (dotted lines of Figure 4.3.a).

4.3.2 CCN concentrations as a function of supersaturation

Although the changes in particle hygroscopic properties presented in Section 4.3.1 increased particles' susceptibility to nucleation scavenging, in this section we show that, even after several hours of aging, particle emissions do not always increase the number concentration of CCN. Changes in CCN concentrations from particle emissions depended strongly on aerosol dynamics near the emission source. We evaluated the contribution of diesel emissions to overall CCN concentration (N_{CCN}) by comparing N_{CCN} between simulations with and without diesel emissions. The difference in CCN concentrations, ΔN_{CCN}, is shown in Figure 4.3.b

for each set of aging conditions. Diesel emissions caused an increase in the aerosol number concentration, regardless of aging conditions, but only in certain cases did this increase in aerosol number correspond to an increase in N_{CCN}.

In the previous section, we showed that diesel particles often become encompassed in highly hygroscopic particles through coagulation events, increasing their susceptibility to removal through nucleation scavenging at $s < 0.2\%$. However, these small diesel particles do not form distinct CCN if they are incorporated in particles that were CCN-active prior to the coagulation event. Unless condensation occurred, diesel particles that did not coagulate with background particles remained too hydrophobic to increase N_{CCN} at any $s < 1\%$ (Figure 4.3.b). At high supersaturation values ($s > 0.2\%$), diesel emissions caused the greatest increase in N_{CCN} in the presence of condensation and the absence of coagulation, suggesting that diesel particles experience sufficient growth by condensation to form new CCN at these high values of s. At low supersaturation thresholds ($s < 0.2\%$) N_{CCN} was nearly the same for simulations with or without diesel emissions, indicating that diesel emissions did not influence N_{CCN} at these low values of s.

4.3.3 Relative importance of changes in size versus composition

As discussed in Section 4.3.1, the changes in CCN activation are the result of simultaneous changes in particles' dry diameter and hygroscopicity parameter. The evolution of diesel particles' geometric mean diameter ($D_{\mathrm{dry,gm}}$) and geometric mean hygroscopicity parameter (κ_{gm}) are shown in Figures 4.4.a and 4.4.b, respectively. Changes in particle hygroscopicity were driven almost entirely by condensation (Figure 4.4.b), while both condensation and coagulation were important in determining diesel particles' size distribution (Figure 4.4.a).

For the simulation including both condensation and coagulation, the relative importance of changes in size and composition on CCN activity are compared in Figure 4.4.c. The supersaturation at which 50% of particles activate, s_{50}, is shown for 1) the population of diesel particles simulated by PartMC-MOSAIC, 2) the same particles but retaining their emitted composition and applying the modeled change in size, and 3) the same particles but retaining their emitted size with the modeled change in composition.

For the exact particle population from PartMC-MOSAIC (black line), s_{50} is approximately 3% at the start of the simulation, indicating that most particles are too hydrophobic to activate at relevant supersaturation levels. As particles increased in size (Figure 4.4.a) and hygroscopicity (Figure 4.4.b), s_{50} rapidly decreased. By 3:00 pm, s_{50} was less than 0.2% (black line), corresponding to the shift in f_{dsl} shown in Figure 4.3.a. If only changes in size were included (red line), s_{50} was an order of magnitude higher than for the exact simulation. On the other hand, if only particles' composition was modified, s_{50} was over-predicted by a

Table 4.3: Parameters assigned to diesel emissions in analysis of sensitivity to emission size distribution. The quantity $s_{50,\mathrm{emit}}$ is the supersaturation at which 50% of freshly emitted particles activate.

	size distribution parameters		composition				
Simulation	$D_{\mathrm{gm,emit}}$ (μm)	$\dot{N}_{\mathrm{emit}}$ ($\mathrm{m^{-2}s^{-1}}$)	BC	POA	SO_4	κ_{emit}	$s_{50,\mathrm{emit}}$
S1	0.025	1.28×10^9	70%	30%	0%	3×10^{-4}	8.3%
S2	**0.05**	$\mathbf{1.6{\times}10^8}$	**70%**	**30%**	**0%**	$\mathbf{3{\times}10^{-4}}$	**3.9%**
S3	0.1	2×10^7	70%	30%	0%	3×10^{-4}	1.9%
S4	0.2	2.5×10^6	70%	30%	0%	3×10^{-4}	0.9%

Table 4.4: Parameters assigned to diesel emissions in analysis of sensitivity to emission composition

	size distribution parameters		composition				
Simulation	$D_{\mathrm{gm,emit}}$ (μm)	$\dot{N}_{\mathrm{emit}}$ ($\mathrm{m^{-2}s^{-1}}$)	BC	POA	SO_4	κ_{emit}	$s_{50,\mathrm{emit}}$
C1	**0.05**	$\mathbf{1.6{\times}10^8}$	**70%**	**30%**	**0%**	$\mathbf{3{\times}10^{-4}}$	**3.9%**
C2	0.05	1.6×10^8	68.6%	29.4%	2%	6.8×10^{-3}	2.3%
C3	0.05	1.6×10^8	63%	27%	10%	6.5×10^{-2}	1.3%
C4	0.05	1.6×10^8	35%	15%	50%	3.2×10^{-1}	0.6%

factor of three (blue line). Both changes in size and hygroscopicity must be included to model CCN activity, and changes in hygroscopicity are particularly important.

In summary, condensation caused the critical supersaturation of the majority of particles to decrease and, thereby, increased the number fraction susceptible to nucleation scavenging at high supersaturation thresholds ($s > 0.2\%$). The particles that aged by condensation also tended to increase N_{CCN}. On the other hand, coagulation increased particles' susceptibility to removal through nucleation scavenging at low s ($s < 0.1\%$), but diesel emissions did not lead to an increase in N_{CCN} at any $s < 1\%$ if aged by coagulation alone.

4.4 Sensitivity of CCN activity to particle size and composition at emission

The properties of primary aerosol particles are determined partly by aging in the atmosphere, as discussed in the previous section, and partly by their characteristics at emission. In this section, we explore to what extent particle properties at emission influence their CCN activation properties after aging. We present a series of sensitivity simulations in which we varied the size distribution and composition of the particles at emission. Because the overall mass emission rate is typically better constrained than the assumed particle size distribution and composition, we performed and compared simulations for which the mass emission rate was the same, but the microphysical properties of individual particles were varied.

Results are presented for two sets of simulations, outlined in Tables 4.3 and 4.4. In scenarios S1–S4

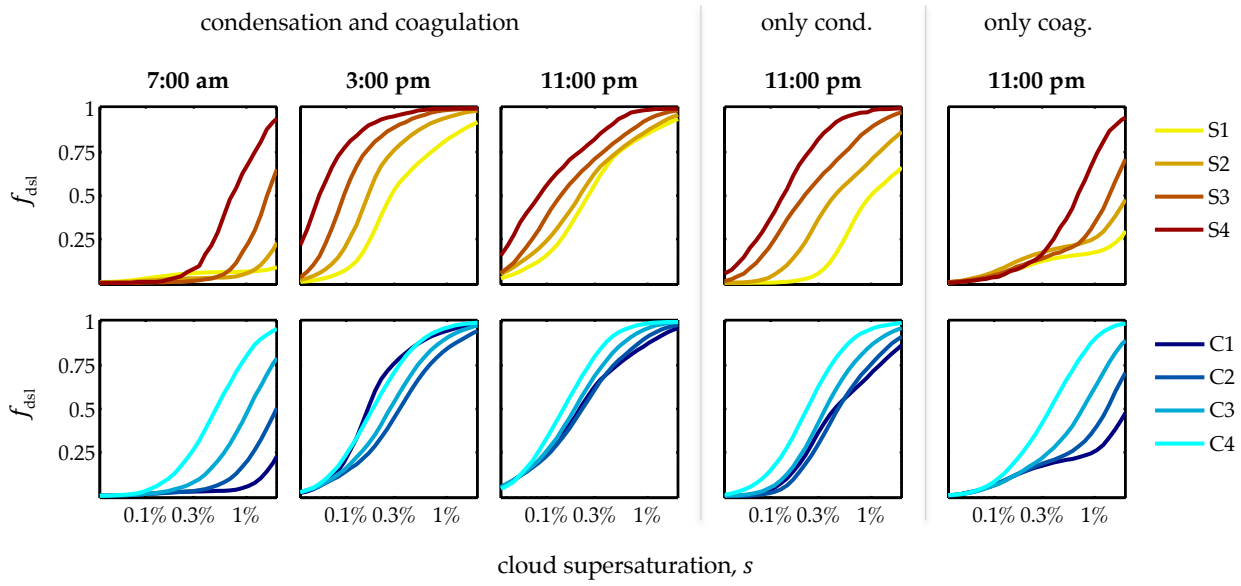

Figure 4.5: Fraction of particles susceptible to nucleation scavenging, f_{dsl}, as a function of cloud supersaturation s. Shown at 7:00 am, 3:00 pm, and 11:00 pm for simulations including both condensation and coagulation, and only at 11:00 pm for simulations of condensation only and coagulation only.

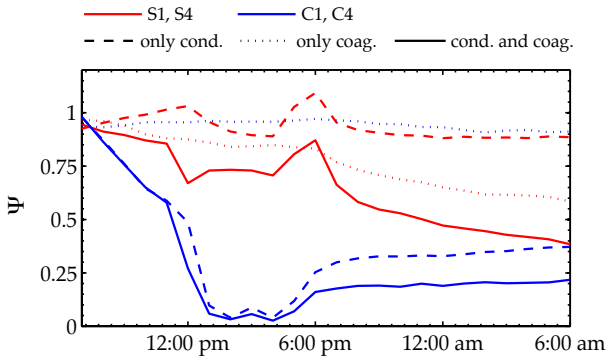

Figure 4.6: Time series of sensitivity parameters Ψ_{S} and Ψ_{C}. Differences between S1 and S4 are shown by red lines, illustrating the change in sensitivity to particles' emission size distribution, and differences between C1 and C4 are shown by blue lines, indicating the sensitivity to particles' composition at the time of emission. Results are shown for simulations including only the effects of condensation (dashed lines), only the effects of coagulation (dotted lines), and both condensation and coagulation (solid lines).

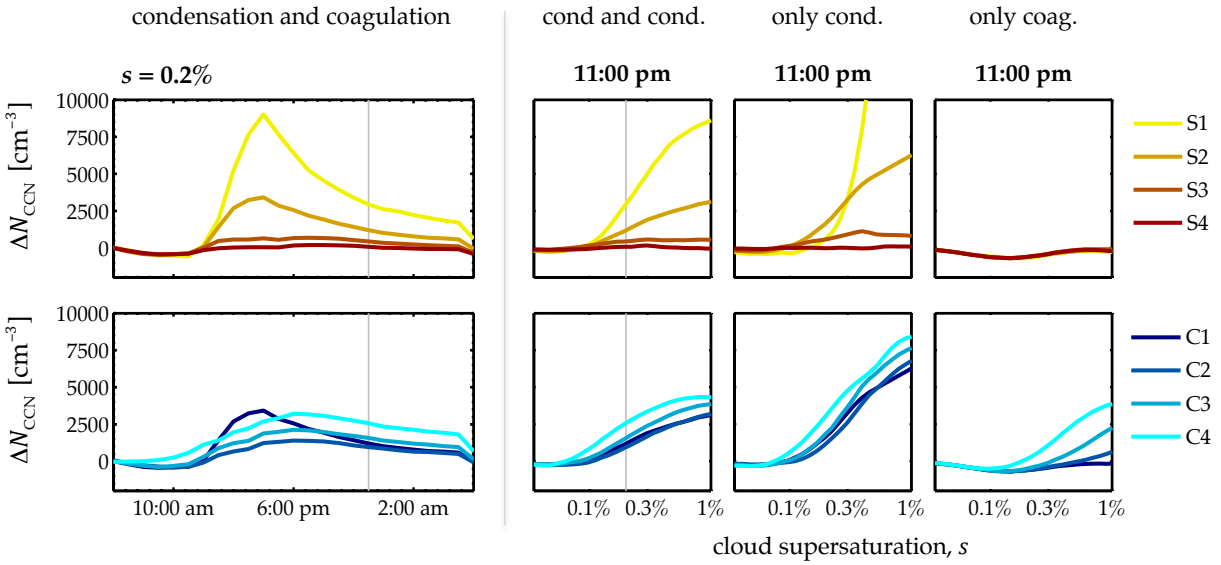

Figure 4.7: Difference in CCN concentrations between simulations with and without diesel emissions, ΔN_{CCN}, for scenarios S1–S4 (top) and C1–C4 (bottom). Results are shown as a function of time for a single cloud supersaturation, $s = 0.2\%$, for simulations including both condensation and coagulation and are shown as a function of supersaturation at a single time, 11:00 pm, for all aging conditions.

(Table 4.3) diesel particles were emitted with the same composition in all scenarios (70% BC, 30% POA), and the emission size distribution was varied. To maintain the same mass emission rate while changing the particle size distribution, the number emission rate was varied accordingly. For example, doubling the geometric mean diameter of diesel emissions ($D_{\mathrm{gm,emit}}$) reduced the number emission rate ($\dot{N}_{\mathrm{emit}}$) by a factor of 8. In scenarios C1–C4 (Table 4.4), diesel emissions had the same size distribution in all four scenarios, and particle composition at emission was varied. Increasing the SO_4 content of emitted particles corresponded to an increase in their effective hygroscopicity parameter at emission (κ_{emit}). A particle's critical supersaturation for CCN activation ($s_{\mathrm{c},i}$) decreases as $D_{\mathrm{dry},i}$ or κ_i increases. Scenarios S2 and C1 are identical, corresponding to the baseline scenario that was presented in Section 4.3.

4.4.1 Sensitivity of nucleation scavenging to particle characteristics at emission

The fraction of diesel particles able to activate into CCN, $f_{\mathrm{dsl}}(s)$, is shown for scenarios S1–S4 and C1–C4 in Figure 4.5. As in the base case scenario, particles activated into CCN more easily after aging by condensation and coagulation. The temporal evolution of f_{dsl} at $s = 0.3\%$ is shown in the left panel of Figure 4.5 for simulations including both condensation and coagulation. At a single time, 11:00 pm, results are shown as a

function of supersaturation for each set of aging conditions. If differences between f_{dsl} at some s are large, then particles' susceptibility to CCN activation and their subsequent removal depends strongly on differences in emitted particle properties between scenarios at that s. We quantify how each aging mechanism affects differences in CCN activity between scenarios using a single value, the supersaturation required to activate 50% of the particle population (s_{50}).

Scenarios S1–S4

The evolution of $f_{\mathrm{dsl}}(s)$ is shown for S1–S4 in Figure 4.5.a. All other factors being equal, particles with large diameters (e.g., S4) are able to activate at lower values of s than particles with small diameters (e.g., S1). Values for $f_{\mathrm{dsl}}(s)$ at 7:00 am show the characteristics of diesel particles when all emissions are fresh. The temporal evolution of $f_{\mathrm{dsl}}(s)$ was influenced by the same processes outlined in Table 4.2.

In all scenarios S1–S4, CCN-activity increased for all particles as they aged by condensation (11:00 am–4:00 pm). Condensational aging caused the greatest changes in $f_{\mathrm{dsl}}(s)$ for any given scenario, but, in the absence of coagulation, f_{dsl} for $0.1\% < s < 1\%$ remained sensitive to particles' emission size distribution after aging. In simulations that included coagulation without condensation, a portion of particles were encompassed in large background particles that were CCN-active at $s < 0.1\%$, but many particles remained unaltered and hydrophobic. Aerosol properties evolved most rapidly and differences in CCN activity were smallest when the effects of both condensation and coagulation were included. In the simulations including both processes, the median critical supersaturation s_{50} initially ranged from 0.7% (S4) to 5.9% (S1) and decreased to the range of 0.08% (S4) to 0.18% (S1) after 24 hours. Differences in s_{50} are discussed in further detail in Section 4.4.1

Scenarios C1–C4

Although coagulation was important for decreasing the sensitivity of f_{dsl} to particles' emission size, condensation was the dominant process influencing sensitivities to particles' initial composition. At 7:00 am, when all diesel particles were fresh, f_{dsl} for C1–C4 was determined by particles' properties at emission, and s_{50} ranged from 0.5% to 3%. Particles that were initially hydrophobic (scenario C1) were unable to activate except in highly supersaturated clouds, but particles with substantial hygroscopic coating were CCN-active at lower values of s. Particle size and effective hygroscopicity parameter κ_i increased as they accumulated hygroscopic coating through condensation, and values of κ_i increased more rapidly when diesel emissions were initially hydrophobic (C1) than for particles emitted with some hygroscopic coating (C2–C4). By the time the simulations ended at 6:00 am the following morning, s_{50} ranged from 0.1–0.2%, regardless of parti-

cles' initial hygroscopicity. In these simulations, s_{50} decreased to lower values for particles emitted without any SO_4 coating (C1) than particles emitted with 2% or 10% SO_4 by mass (C2 or C3, respectively) because of more ammonium nitrate forming on the particles without SO_4 coating, which are dry particles. The additional ammonium nitrate formation on these particles occurs because the current version of MOSAIC neglects the Kelvin effect for dry particles, since the values for surface energies for the species of interest are unknown. The relative humidity varies throughout the day, starting at 95% and then dropping quickly as the simulation proceeds. Particles emitted early in the morning that initially contain some inorganic coating (C2–C4) take up water at these high values of RH, and ammonium nitrate formation later in the day is influenced by the Kelvin effect for these particles. Particles emitted without any inorganic coating (C1) remained dry throughout the morning, and ammonium nitrate condensed more quickly on these particles starting at 11:00 am because the Kelvin effect were neglected.

When coagulation was the only mechanism at work, f_{dsl} depended strongly on particles' initial composition throughout the simulation. Only particles that participated in coagulation events were altered under these conditions, so particles that did not coagulate maintained their initial hygroscopic properties throughout the simulation. The smallest emitted particles were likely to coagulate with much larger pre-existing particles, increasing f_{dsl} at $s \approx 0.1\%$ in simulations including coagulation without condensation. Although aging by coagulation did ultimately reduce the dependence of s_{50} on particles' initial composition, in the absence of condensation many particles remained unaffected after hours of aging.

Sensitivity of median critical supersaturation to particle characteristics at emission

As discussed in Sections 4.4.1 and 4.4.1, the critical supersaturation at which 50% of particles activate, s_{50}, decreased in each scenario, indicating a shift in the f_{dsl} curve toward lower supersaturation levels and an increase in particles' susceptibility to nucleation scavenging. If differences in s_{50} between scenarios are large at some time, the supersaturation at which the majority of emitted particles activate depends strongly on particle characteristics at emission. We quantify how difference in s_{50} at emission ($s_{50,\mathrm{e}}$) affect differences in s_{50} throughout the simulation using the quantity Ψ. For example, Ψ is defined for scenarios S1-S4 as:

$$\Psi_{\mathrm{S}} = \left| \frac{\left[s_{50}\right]_{\mathrm{S4}} - \left[s_{50}\right]_{\mathrm{S1}}}{\left[s_{50,\mathrm{emit}}\right]_{\mathrm{S4}} - \left[s_{50,\mathrm{emit}}\right]_{\mathrm{S1}}} \right|. \tag{4.3}$$

The corresponding sensitivity for scenarios C1 and C4 is given by Ψ_{C}. The end members of the scenarios (S1 and S4, C1 and C4) are always used when computing Ψ.

The quantity s_{50} varies with time and depends on the emission scenario and the aging conditions, whereas $s_{50,\mathrm{emit}}$ is a constant for each emission scenario and is independent of the aging conditions. If $\Psi_{\mathrm{S}} = 1$, values

for s_{50} differ between scenarios S1 and S4 as much as they did at the time of emission, although values for s_{50} may have decreased in each case. The other extreme, $\Psi_S = 0$, suggests that there is no difference in s_{50} between scenarios S1 and S4 and that particle emission properties do not influence their removal through nucleation scavenging after particles are processed in the atmosphere. The sensitivities Ψ_S or Ψ_C, therefore, indicate the degree to which differences in $s_{50,e}$ translate to differences in s_{50} after aging.

Figure 4.6 shows the time series for Ψ_S (red lines) and Ψ_C (blue lines). These quantities were computed for each set of processing conditions. Values for Ψ_S and Ψ_C were lowest at all times when both processes were included, and simulations of each mechanism acting alone show which process was most influential in altering variability in s_{50} between scenarios.

Early in the morning, values Ψ_S and Ψ_C were nearly equal to 1, indicating that the spread in s_{50} had not changed relative to $s_{50,\mathrm{emit}}$. Photochemical reactions led to a period of rapid aging by condensation from 11:00 am until 4:00 pm. During this time, the original difference in hygroscopicity between diesel particles in C1 and C4 was eliminated after particles were coated with condensing aerosol, causing Ψ_C to decrease to nearly 0 between 2:00 pm and 4:00 pm (solid and dashed blue lines). Although differences in chemical composition were rapidly eradicated by condensation, differences in size (quantified by Ψ_S) were altered much more slowly and were affected mostly by coagulation. Values for Ψ_S remained greater than 0.9 when coagulation was not included (dashed red line), but Ψ_S decreased to 0.25 after 24 hours of simulation if coagulation was included in addition to condensation (solid red line).

Coagulation was also important in altering the composition of particles emitted after sunset. Particles emitted after photochemical reactions ceased did not acquire a hygroscopic coating through condensation, so s_{50} varied more between C1–C4 at 6:00 pm ($\Psi_C = 0.2$) than at 4:00 pm ($\Psi_C \approx 0$) for scenarios including only condensation or both condensation and coagulation (solid and dashed blue lines). If the effects of coagulation were included in addition to condensation, Ψ_C decreased to 0.1 by 6:00 am the following morning (solid blue line), otherwise Ψ_C remained at the value of 0.2 until the simulation ended (dashed blue line).

In summary, the degree to which differences in particle microphysical properties at emission affect the mean CCN activation properties depends on the aging conditions near the emission source. Condensation rapidly altered particles' composition, such that s_{50} was insensitive to differences in particle composition at the time of emission ($\Psi_C \approx 0$). On the other hand, coagulation caused differences in s_{50} to decrease between particles emitted with different size distributions. As a result, coagulation caused Ψ_S to decrease to 0.35 after 24 hours under conditions of rapid aging by both condensation and coagulation, whereas $\Psi_S \approx 1$ throughout the simulation if particles aged only by condensation.

4.4.2 Sensitivity of CCN concentrations to particle characteristics at emission

Section 4.4.1 focused only on particles originating from diesel exhaust in order to evaluate the susceptibility of these particles to removal through nucleation scavenging. We now consider the entire particle population, including those from other sources, to evaluate differences in absolute CCN concentrations (ΔN_{CCN}) between simulations with and without diesel emissions. The temporal evolution of ΔN_{CCN} is shown at $s = 0.3\%$ for simulations including both condensation and coagulation in the left panel of Figure 4.7. For each set of aging conditions, results are shown as function of supersaturation at a single time, 11:00 pm, in the right panel of Figure 4.7. These figures show how differences in aging conditions near the emission source affect the response in N_{CCN} to variation in particles' initial size distribution (S1–S4) and composition (C1–C4).

Scenarios S1–S4

In scenarios S1–S4, total mass emission rates were identical, but the size distribution was varied, and particle number emission rates were adjusted accordingly. Although changes in the emission size distribution strongly influenced the aerosol number concentration, only under specific aging conditions did this increase in aerosol number lead to an increase in N_{CCN}. Diesel emissions did not strongly influence N_{CCN} at low supersaturation thresholds ($s < 0.2\%$), regardless of particle characteristics at emission or aging conditions near the emission source (right panel of Figure 4.7). At high supersaturation thresholds, fine particle emissions (S1–S2) caused large changes in N_{CCN}, but required condensation aging to do so. In all cases, ΔN_{CCN} was not proportional to the change in aerosol number. For example, decreasing $D_{\mathrm{gm,emit}}$ from the base case value of 0.05 μm (S2) to 0.025 μm (S1) corresponded to an increase in the number emission rate in scenario S1 by a factor of 8 and an increase in the number concentration by as much as a factor of 4, but N_{CCN} differed at most by a factor of 2 at even the highest values of s shown. Some emitted particles were lost through coagulation events, and others did not age sufficiently by condensation to activate. If the effects of coagulation were neglected, N_{CCN} differed by a factor of 6 between scenarios S4 and S1 at high supersaturation thresholds (e.g. $s = 1\%$).

Fine particle emissions increased N_{CCN} less efficiently at low supersaturation threshold (e.g., $s = 0.1\%$), so there was less variability in ΔN_{CCN} between scenarios S1–S4 at low s compared to high s. When the effects of coagulation were not simulated, emissions of the smallest diesel particles caused N_{CCN} to decrease by as much as 1000 cm^{-3} relative to simulations without diesel emissions. Particles present in high number concentrations competed for condensing aerosol, so a decrease in the aerosol number concentration by coagulation actually enhances the effects of condensation. If both processes were simulated, emissions of fine particles resulted in a 500 cm^{-3} increase in N_{CCN} relative to simulations without diesel emissions.

Therefore, although coagulation depletes the aerosol number concentration, causing a decrease in N_{CCN} at high values of s, the reduction in particle surface area by coagulation results in faster aging by condensation, causing an increase in N_{CCN} relative to simulations without coagulation at low values of s. In the absence of condensation, $\Delta N_{\mathrm{CCN}} \approx 0$ for all s shown, regardless of particles' emission size distribution, so N_{CCN} was insensitive to diesel emissions for all $s < 1\%$.

Scenarios C1–C4

Mass and number emission rates were the same for all scenarios C1–C4, so differences in N_{CCN} between scenarios were caused only by differences in per-particle solubility. After only a few hours of aging, diesel emissions caused an increase in N_{CCN} at $s > 0.1\%$ in all scenarios C1–C4. As established in Section 4.4.1, particle CCN activation properties became less sensitive to their initial composition after hours of aging by condensation, and as a result N_{CCN} differed by less than 20% between scenarios C1–C4 for any $0.1\% < s < 1\%$.

4.5 Conclusions

This study evaluates the importance of particles' emission size distribution and composition in predicting their CCN activity as particles undergo aging in the atmosphere. We also compared the relative importance of the two aging processes, condensation and coagulation, and quantified how these findings depend on the environmental supersaturation at which CCN activity is evaluated. The results were first presented for a single emission scenario in Section 4.3, in which particles were emitted with characteristics representing particles from diesel exhaust. We then analyzed how particles' size and composition at emission affect their CCN activity in Section 4.4.

The size distribution and composition of emitted particles affected their removal and their influence on CCN concentrations only under specific aging conditions. When evaluated at $s < 0.2\%$, diesel emissions yield little increase in N_{CCN}, regardless of particle characteristics at emission. At these low supersaturation thresholds ($s < 0.2\%$), N_{CCN} differed by at most 5% between simulations with and without diesel emissions, as opposed to a factor of two difference in N_{CCN} at $s > 0.2\%$ for certain aging conditions. Therefore, N_{CCN} was sensitive to particles' emission characteristics only at $s > 0.2\%$, and under these conditions changes in N_{CCN} depended strongly on the aging mechanisms at work. Under regimes of rapid aging by condensation, N_{CCN} at $s > 0.2\%$ depended more strongly on particles' emission size distribution than on their composition at emission. On the other hand, if condensation was negligible, then particle emissions did not increase

N_{CCN} at any s below 1% and N_{CCN} was insensitive to particle properties at emission.

It is difficult to compare our process-level analysis, which isolates the influence of emission properties and environmental characteristics as causes of changing CCN on small scales, with global modeling results, which integrate changes over many conditions. Nevertheless, our results are broadly consistent with global modeling studies that evaluate the sensitivity of CCN concentrations to particle emissions. (128) compared global model predictions of CCN against measurements, and showed that carbonaceous aerosols must be included to adequately predict global CCN concentrations. We showed that particle emissions led to a two-fold increase when environmental supersaturation was high enough ($s > 0.2\%$), but we add the finding that CCN concentrations are less affected at low s ($s < 0.2\%$) or in the absence of condensation. (75) showed that changes in CCN concentrations from particle emissions depended on particles' emission source, suggesting a sensitivity of CCN concentrations to particle microphysical properties at emission. Our results are consistent with these global modeling results for environmental supersaturations above 0.2% when particles are aged under conditions of rapid secondary aerosol production, but we also find that N_{CCN} is insensitive to particle characteristics at emission at low supersaturations or in the absence of condensation.

Where particle emissions did cause N_{CCN} to increase, there was a stronger sensitivity to the emission size distribution than the emission composition, consistent with global modeling studies that have also identified the size distribution of aerosol emissions as a key uncertainty in the prediction of aerosol number concentrations and the associated CCN (106; 112). We showed that although varying the size distribution at emission caused large differences in the original aerosol number concentration, changes in N_{CCN} were always smaller than changes in aerosol number.

The composition of particle emissions did not strongly influence their CCN activity if particles were emitted prior to a rapid condensation event, which is consistent with measurements. For example, although the effective hygroscopicity parameter κ of fresh biomass burning emissions is known to differ between fuel types, (41) showed that variability in κ decreased after particles aged by formation of secondary aerosol in a smog chamber. (39) showed that CCN activity of particles in remote regions depends strongly on particles' size distribution and is rather insensitive to particles' composition, consistent with the rapid changes in aerosol composition caused by condensation in this work. (42) modeled the CCN activity of aerosols measured at varying distances from pollution sources and found that far from emission sources, CCN concentrations could be modeled with reasonable accuracy assuming the aerosol is a full internal or external mixture, but near the emission source a more complex representation of aerosol mixing state was needed for agreement between measured and modeled CCN. Similarly, a different modeling study using PartMC-MOSAIC (155) found that CCN activity could be modeled with high accuracy using a size-resolved rather than particle-

resolved representation of the mixing state after only a few hours of aging by condensation. Consistent with these findings, we show that after a few hours of aging particles' CCN activation properties were more influenced by their initial size distribution than their initial composition. Differences in composition are important only near the emission source as long as particles experience a period of intense secondary aerosol formation.

In this study, we evaluated sensitivities of CCN activity within 24 hours after emission to particle characteristics at emission, a first step in isolating the importance of including particle microphysical properties in aerosol emission inventories. A complete evaluation of the influences of primary aerosol characteristics on CCN concentrations would include additional factors: the effects of differing environmental conditions, the evolution of particle characteristics after the 24 hours of simulation, and the effects of heterogeneous reactions, such as photochemical oxidation and N_2O_5 hydrolysis.

In summary, CCN concentrations were sensitive to particle microphysical properties at emission only under specific aging conditions. In all cases presented here, the number of CCN at $s < 0.2\%$ was insensitive to particles' emission size and composition. At $s > 0.2\%$, diesel emissions did increase CCN concentrations, and in this regime the number concentration of CCN was far more sensitive to particles' emission size than to composition. Only in the absence of secondary aerosol formation did differences in particles' initial composition influence their CCN activity after aging.

Chapter 5

Explaining variance in black carbon's aging timescale

5.1 Introduction

Chapter 4 focused on the sensitivity of primary particles' cloud condensation nuclei (CCN) activity, after particles have aged in the atmosphere, to their size and composition at emission, considering limiting aging conditions and a range of supersaturation levels. Here, we focus not on the characteristics of the particles, but rater the characteristics of the chemical environment to which they are exposed. Again, we assess changes in CCN activation by emitted particles, but focusing on the factors that drive this transformation.

In addition to being important for estimating particles influence on CCN concentrations, as was discussed in Chapter 4, changes in CCN activation by initially insoluble primary aerosol types, such black carbon (BC), is important for predicting aerosol removal. The dominant removal mechanism of BC mass from the atmosphere is wet deposition (35), with one important pathway being the activation of BC-containing particles into cloud condensation nuclei (CCN) and their subsequent removal if the cloud precipitates. While freshly emitted BC-containing particles are too small and hydrophobic to activate (85; 144), changes in particle characteristics, termed "aging", often increase the particles' susceptibility to cloud droplet nucleation and wet removal (46; 19; 159), so these processes must be included in global models.

The simplest representation of aging classifies BC mass as either hydrophobic or hydrophilic, such that hydrophilic BC is susceptible to removal by wet deposition and hydrophobic BC is not. In this framework, BC is transferred from the hydrophobic (fresh) category to the hydrophilic (aged) category according to a first-order aging timescale (34; 36; 74). Global models apply a fixed aging timescale of 1–3 days. Global modeling studies have shown that estimates of BC's climate forcing are sensitive to the assumed aging timescale (76), but its value is not well constrained. While some climate models have been moving toward aerosol modules that represent aerosol aging using several interacting modes (5; 9; 147; 87), the practice of using a fixed aging timescale is still widespread (66; 25; 118).

To improve upon using one constant value for the aging timescale, several studies have developed parameterizations of BC's aging timescale that vary with environmental conditions. (82) developed a parameter-

ization of black carbon aging by condensation that depended on the condensation rate of sulfuric acid and overall BC surface area. They showed that, by allowing for slower aging in the winter, their parameterization was better able to represent seasonal variability in black carbon transport to the Arctic. (101) extended this approach and developed a parameterization of aging timescales based on simulations with a box model. Their parameterization predicted the rate for BC to transition from a hydrophobic class to a hydrophilic class, expressed as a function of the mass-normalized coating rate and on parameters of the fresh BC size distribution. (113) showed that timescales for aging by coagulation decrease with the overall aerosol number concentration, which they parameterized using a simple power law, and this parameterization was applied by (36). (107) parameterized size-resolved coagulation rates as a first-order loss process that depends on the overall size distribution. In an analysis of aging timescales in a specific urban environment using a particle-resolved model, (114) showed that timescales for particles to transition from CCN-inactive to CCN-active varied diurnally due to variations in condensation aging rates. Because the timescale from (114) is based on changes in particle CCN activity, it quantifies changes in particle characteristics that these first-order aging models are meant to represent.

This study builds on the work of (114) to generalize how the CCN-based aging timescale varies with scenario-specific properties. Unlike other aerosol schemes, which simplify the representation of particle composition, the particle-resolved model tracks the composition of each simulated particle and is, therefore, uniquely suited to study the impact of aging on per-particle CCN activity. The focus of this paper is to identify the set of independent variables that best explain variance in BC's aging timescale for a large collection of simulations. Using the independent variables identified in this study, we will later introduce a simple aging parameterization for use in global models.

Most of this research has been published as a manuscript in Atmospheric Chemistry and Physics (44).

5.2 Extracting aging timescales from particle-resolved model output

In a first-order model of aging, particles transition from fresh to aged according to an aging timescale, τ_{aging}. In this framework, a criterion must be applied to distinguish fresh and aged particles. Particle CCN activity at a specified environmental supersaturation is the aging criterion applied in this work, so the aging timescale indicates changes in particles' susceptibility to removal by wet deposition. We define aged particles as those that are activated at a specified environmental supersaturation, and fresh particles are CCN-inactive at that

Table 5.1: Aerosol Emissions and Initial Conditions for Baseline Simulation

Initial/Background	N (m^{-3})	D_{gm} (μm)	σ_{g}	Composition by Mass
Aitken Mode	9×10^8	0.02	1.45	50% $(NH_4)_2SO_4$, 50% SOA
Accumulation Mode	7.5×10^8	0.116	1.65	50% $(NH_4)_2SO_4$, 50% SOA
Emissions	$\dot{N}_{\mathrm{emit}}$ ($\mathrm{m}^{-2}\mathrm{s}^{-1}$)	$D_{\mathrm{gm,emit}}$ (μm)	σ_{g}	Composition by Mass
Meat cooking	9×10^6	0.0865	1.9	100% POA
Diesel vehicles	3.2×10^7	0.05	1.7	30% POA, 70% BC
Gasoline vehicles	1×10^7	0.05	1.7	80% POA, 20%BC

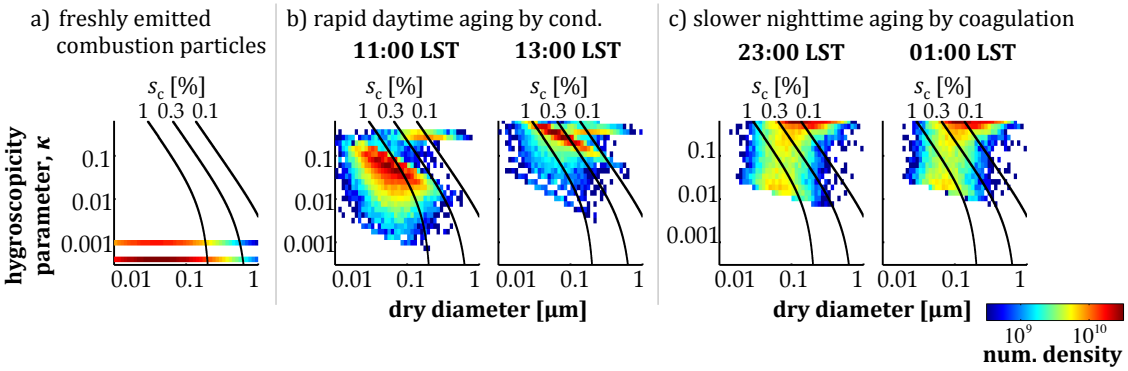

Figure 5.1: Two-dimensional probability density distribution shows changes in particle properties. As particles increase in size (horizontal axis) and hygroscopicity (vertical axis), they are able to activate at lower critical supersaturation thresholds (superimposed lines). a) Freshly emitted particles are hydrophobic, with $\kappa = 3 \times 10^{-4}$ and $\kappa = 8 \times 10^{-4}$ for diesel and gasoline, respectively. b) During the daytime, particles age rapidly by condensation of semi-volatile substances that are produced through photochemical reactions. c) At night, condensation aging is slow, and particles age only by coagulation.

supersaturation threshold. The first-order aging model is given by:

$$\left[\frac{dN_{\mathrm{fresh}}}{dt}\right]_{\mathrm{aging}} = -\frac{1}{\tau_{\mathrm{aging}}} N_{\mathrm{fresh}}, \tag{5.1}$$

where N_{fresh} is the number concentration of fresh particles.

Before discussing the full set of sensitivity simulations in Section 5.2.3, we describe the particle-resolved simulation of aerosol dynamics in a baseline scenario and show how the aging timescale is used to quantify changes in per-particle CCN activity. The particle-resolved model is described in Section 5.2.1, and the κ-Köhler model (104) for computing CCN activity from the PartMC-MOSAIC data is discussed in Section 5.2.2. We discuss methods for computing aging timescales from the particle-resolved model output in Section 5.2.3.

Table 5.2: Gas-phase Initial Conditions and EmissionsThe emissions represent area emissions and are averaged over the 12-hour emission period. for Baseline Simulation

MOSAIC Species	Symbol	Initial Mole Fraction (ppb)	Emissions (nmol $m^{-2}s^{-1}$)
Nitric oxide	NO	0.1	15.9
Nitrogen dioxide	NO_2	1	0.84
Nitric acid	HNO_3	1.0	
Ozone	O_3	50	
Hydrogen peroxide	H_2O_2	1.1	
Carbon monoxide	CO	21	291.3
Sulfur dioxide	SO_2	0.8	7.53
Ammonia	NH_3	0.5	6.11
Hydrogen chloride	HCl	0.7	
Methane	CH_4	2200	
Ethane	C_2H_6	1.0	
Formaldehyde	HCHO	1.2	1.68
Methanol	CH_3OH	0.12	0.28
Methyl hydrogen peroxide	CH_3OOH	0.5	
Acetaldehyde	ALD2	1.0	0.68
Paraffin carbon	PAR	2.0	96
Acetone	AONE	1.0	1.23
Ethene	ETH	0.2	7.3
Terminal olefin carbons	OLET	2.3×10^{-2}	2.42
Internal olefin carbons	OLEI	3.1×10^{-4}	2.42
Toluene	TOL		4.04
Xylene	XYL	0.1	2.41
Lumped organic nitrate	ONIT	0.1	
Peroxyacetyl nitrate	PAN	0.8	
Higher organic acid	RCOOH	0.2	
Higher organic peroxide	ROOH	2.5×10^{-2}	
Isoprene	ISOP	0.5	0.23
Alcohols	ANOL		3.45

5.2.1 Particle-resolved simulation of aerosol aging

I simulated 288 plume scenarios with PartMC-MOSAIC, varying meteorological conditions, emissions of gases and particles, and the background number concentration, with further description given in Section 5.2.3. The atmospheric composition and environmental conditions differed between the scenarios, but the general structure of all simulations was the same. In each case, we simulated a well-mixed air parcel that is advected over and away from large urban area. All scenarios started at 06:00 LST, at which time the parcel contained only background gas and aerosol without any freshly emitted particles. During transport over the urban area, the parcel received gas and aerosol emissions from 06:00 LST until 18:00 LST, after which all emissions ceased. In these scenarios, we simulate a well-mixed boundary layer during the day, and the parcel is assumed to be in the residual layer at night. The temperature, mixing height, and relative

Table 5.3: Hygroscopicity parameter assigned to aerosol species

aerosol species	κ_i	citation
NO_3	0.65	(32); (133); (104)
SO_4	0.65	(32); (133); (104)
NH_4	0.65	(32); (133); (104)
SOA	0.1	(108)
BC	0	(105)
POA	0.001	(105)

humidity were held constant. Before discussing the full set of scenarios in Section 5.2.3, we show changes in CCN activity and the diurnal evolution of aging timescales in a baseline scenario. For this baseline scenario, Table 5.1 outlines background aerosol number concentration, aerosol emission intensity, and size distribution and composition information for both background and emitted aerosols. The background concentration and emission intensity of gas-phase species are provided in Table 5.2.

5.2.2 κ-Köhler model for computing CCN activity

We determined aging timescales from the particle-resolved results by tracking changes in CCN activity over two consecutive time steps. A particle's ability to activate cloud formation depends on its dry diameter $D_{\mathrm{dry},i}$ and its hygroscopicity parameter κ_i. The equilibrium saturation ratio (S_i) over an aqueous droplet is computed through the κ-Köhler model (77; 104), as described in Chapter 3. We denote the critical saturation ratio at which a particle activates and forms a cloud droplet with $S_{\mathrm{c},i}$ and the critical supersaturation as $s_{\mathrm{c},i} = \big(S(D_{\mathrm{c},i}) - 1\big) \times 100$.

Figure 5.1 shows the two-dimensional number density distribution as a function of the particle dry diameter ($D_{\mathrm{dry},i}$) and the particle hygroscopicity parameter (κ_i), as describe in Chapter 4. Only particles containing BC are shown in this figure. In the scenarios presented in this study, all BC originated from diesel or gasoline exhaust. Choosing a certain environmental supersaturation threshold allows us to classify the particles as fresh or aged. For example, all particles to the left of the line for $s_{\mathrm{c},i} = 1\%$ are considered "fresh" for environmental supersaturations of 1% or lower, and all particles to the right of the line for $s_{\mathrm{c},i} = 1\%$ are considered "aged" at supersaturations above 1%.

The number distributions corresponding to fresh emissions, prior to any aging, are shown in Figure 5.1.a, and changes in the distribution during two time periods are shown in Figures 5.1.b and 5.1.c. Freshly emitted combustion particles are small and hydrophobic, with geometric mean diameter $D_{\mathrm{dry,gm}} = 0.5$ μm and with a hygroscopicity parameter of $\kappa = 3 \times 10^{-4}$ or $\kappa = 8 \times 10^{-4}$ for particles from diesel or gasoline, respectively. Therefore, most BC-containing particles are initially unable to activate at any environmental supersaturation

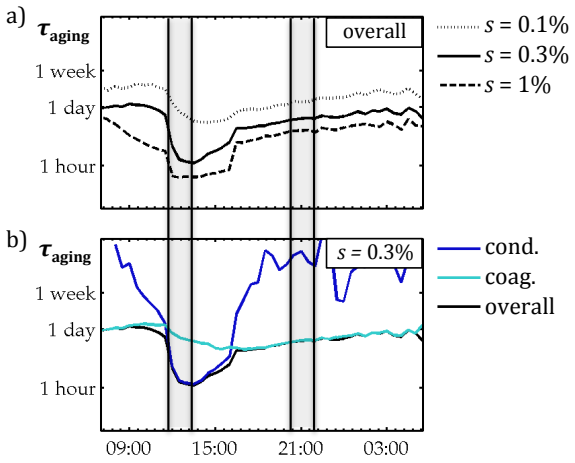

Figure 5.2: For a single scenario, overall aging timescale for $s = 0.1\%$, $s = 0.3\%$, and $s = 1\%$ in Figure 5.2.a and the overall, condensation, and coagulation aging timescales for $s = 0.3\%$ in Figure 5.2.b. The shaded regions show how the value of the aging timescale reflects changes in per-particle characteristics, which correspond to Figure 5.1. Short aging timescales correspond to rapid increases in particle size and hygroscopicity (Figure 5.1.b), and long aging timescales correspond to slow changes in particle properties (Figure 5.1.c)

$s < 1\%$ (lines in Figure 5.1.a). As $D_{\mathrm{dry},i}$ and κ_i for individual particles increase by condensation and coagulation, their critical supersaturation $s_{\mathrm{c},i}$ for CCN-active decreases, shown by particles crossing the lines of constant critical supersaturation in Figure 5.1. Secondary aerosol forms through photochemical reactions during the day, causing rapid changes in particles' size and hygroscopicity. At night aging by condensation rates are slow, so coagulation is the dominant aging mechanism. This diurnal variation in aging rates is consistent with observations (116; 24). We define particles that "age" over a specific time period as those that transition from CCN-inactive to CCN-active, that is the particles that move from below a supersaturation line (CCN-inactive) at time t to above supersaturation line (CCN-active) at $t + \Delta t$.

5.2.3 CCN-based aging timescale

For the entire particle population, this change in the particle properties is quantified using the first-order aging timescale defined in Equation 5.1. Because the time period Δt is short relative to the timescale τ_{aging}, Equation 5.1 can be approximated as:

$$\left[\frac{dN_{\mathrm{fresh}}}{dt}\right]_{\mathrm{aging}} \approx -\frac{\Delta N_{\mathrm{f}\to\mathrm{a}}}{\Delta t}, \tag{5.2}$$

where $\Delta N_{\mathrm{f}\to\mathrm{a}}$ is the number of discrete particles that transition from fresh at time t to aged at time $t + \Delta t$, calculated from changes in the number of fresh particles. In this study, aging timescales are computed over

a time step $\Delta t = 10$ minutes. Combining Equations 5.1 and 5.2, the aging timescale is computed as:

$$\tau_{\text{aging}}(t, s) \approx \Delta t \frac{N_{\text{fresh}}(t, s)}{\Delta N_{\text{f}\to\text{a}}(t, t + \Delta t, s)}. \tag{5.3}$$

We refer to this aging timescale as the "bulk aging timescale" because it corresponds to the entire fresh particle population, and the term $\Delta N_{\text{f}\to\text{a}}$ includes all particles that transition from fresh to aged, regardless of their size. Later, we will introduce an analogous "size-resolved aging timescale". Further details on the derivation of the bulk aging timescale, including number balances for all processes affecting aging, are given in (114).

The temporal evolution of the timescale is shown for the baseline scenario in Figure 5.2.a at $s = 0.1\%$, $s = 0.3\%$, and $s = 1\%$. The aging timescale is a simple metric for quantifying the effects of changes in per-particle size and hygroscopicity that are shown in Figure 5.1, and the gray shading in Figure 5.2.a corresponds to the time periods shown in Figure 5.1. Particles must become highly hygroscopic to activate into cloud droplets at low s (e.g. $s = 0.1\%$) but require less processing to become CCN at higher values of s (e.g. $s = 1\%$), so the aging timescale tends to be shorter for higher values of s.

Any particle that transitions from fresh at t to aged at $t + \Delta t$ does so either by coagulation with a large, hygroscopic particle or by accumulating sufficient condensing material to become hygroscopic. The overall aging timescale τ_{aging} can be represented as the combination of separate timescales for aging by condensation τ_{cond} and by coagulation τ_{coag}:

$$\frac{1}{\tau_{\text{aging}}(t, s)} = \frac{1}{\tau_{\text{cond}}(t, s)} + \frac{1}{\tau_{\text{coag}}(t, s)}. \tag{5.4}$$

The contribution of condensation and coagulation to the overall aging timescale is shown by separate timescales for aging by condensation (τ_{cond}) and coagulation (τ_{coag}) at $s = 0.3\%$ in Figure 5.2.b. We computed the coagulation and condensation aging timescales by counting the number of particles that transition from fresh to aged after participating in a coagulation event, $\Delta N_{\text{f}\to\text{a,coag}}$, or that age only by condensation, $\Delta N_{\text{f}\to\text{a,cond}}$. Then, we applied Equation 5.3 to find the corresponding condensation and coagulation aging timescales. Figure 5.2.b shows that the overall aging timescale is shortest during the day (e.g. 1 h at $s = 0.3\%$) due to rapid condensation of semi-volatile substances, and it is considerably longer at night (e.g. 24 h at $s = 0.3\%$), when coagulation is the dominant aging mechanism. The temporal evolution of τ_{aging} and τ_{cond} are shown for multiple supersaturation levels in (114).

Table 5.4: Input parameters varied in the ensemble of sensitivity simulations. Scenarios corresponding to the baseline conditions are indicated in bold. All combinations of scenarios were included in the full ensemble of 288 simulations.

input parameter	scenario name	values assigned
gas-phase emissions	$\mathbf{G_1}$	baseline gas emissions
	G_2	increase SO_2 emissions by 200% and turn of NH_3 emissions
	G_3	increase SO_2 emissions by 300%
	G_4	increase SOA precursor emissions by 200% and turn off NH_3 emissions increase selected SOA-precursors by 100%
black carbon emissions	$\mathbf{BC_1}$	baseline diesel and gasoline emissions
	BC_2	increase diesel and gasoline emissions by a factor of five
	BC_3	increase diesel and gasoline emissions by a factor of ten
background aerosol	$\mathbf{BG_1}$	baseline background aerosol concentration
	BG_2	decrease background aerosol concentration by 45%
relative humidity	$\mathbf{RH_1}$	95%
	RH_2	50%
meteorological conditions	$\mathbf{M_1}$	5° N, July 19, 303 K
	M_2	5° N, January 5, 303 K
	M_3	40° N, July 19, 298 K
	M_4	40° N, January 5, 275 K
	M_5	60° N, July 19, 293 K
	M_6	60° N, January 5, 263 K

5.3 Ensemble of particle-resolved model scenarios

The aging timescales shown in Figure 5.2 are limited to only one scenario, and aging rates vary with local conditions. For example, the number concentration and size distribution of background particles affect coagulation rates and, thereby, the coagulation aging timescale. In order to identify the set of independent variables that best explain variance in BC's aging timescale under a range of atmospheric conditions, we simulated aerosol dynamics in a series of plume scenarios and extracted aging timescales for each scenario. As we will show, the environmental properties that affect aerosol dynamics varied diurnally and differed between scenarios, causing the aging timescale to range from less than an hour (a large portion of particles age per time interval) to longer than a week (few particles age per time interval).

The input parameters that were varied between the scenarios are shown in Table 5.4. These input parameters were selected to produce a range of environmental conditions, consistent with observations described by (65) and references therein. Simulations were performed using every combination of input parameters given in Table 5.4, leading to a total of 288 scenarios. In each scenario, aerosol concentrations and particle characteristics varied throughout the 24-hour simulation. The conclusions in this study are based on these simulations of urban air masses.

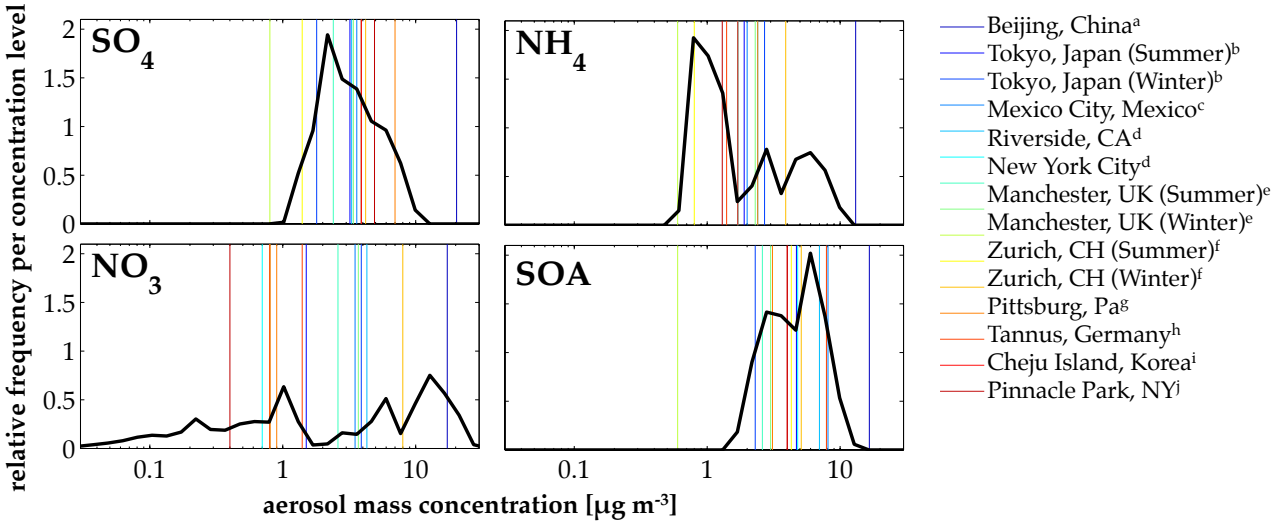

Figure 5.3: Probability density function of aerosol mass species in simulations (black line in each graph) show that model cases represent variation in atmospheric conditions from ambient observations (vertical colored lines). Probability density functions include all output time steps in the full ensemble of sensitivity simulations.

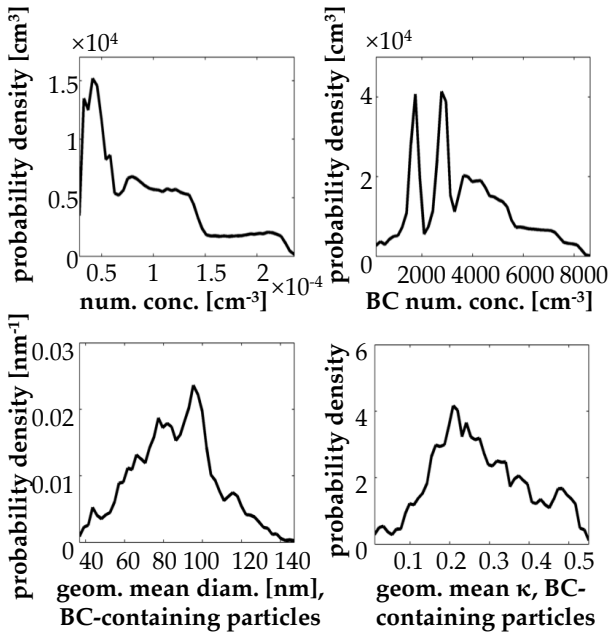

Figure 5.4: Probability density function of a) total aerosol number concentration, b) total number concentration of BC-containing particles, c) geometric mean diameter of BC-containing particles, and d) geometric mean hygroscopicity parameter of BC-containing particles.

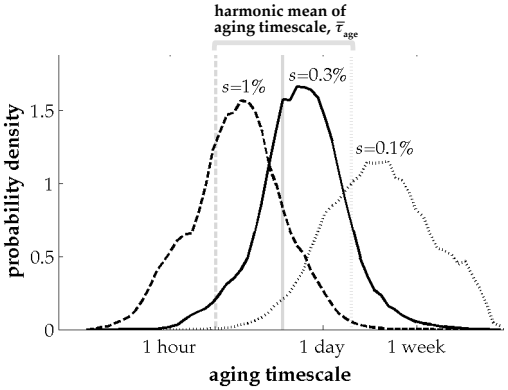

Figure 5.5: Probability density function of aging timescales for the full ensemble of sensitivity simulations, computed at three environmental supersaturation levels: $s = 0.1\%$, $s = 0.3\%$, and $s = 1\%$.

Figure 5.3 shows the distribution of aerosol mass concentration for selected aerosol species for all scenarios simulated with PartMC-MOSAIC (black lines) and corresponding ambient observations compiled by (65) (vertical colored lines). The range of conditions simulated in the ensemble of scenarios is representative of the distribution in concentrations observed in these urban areas. The distribution in the number concentration of all particles and of BC-containing particles are shown in Figure 5.4.a and 5.4.b, respectively. The size and composition of BC-containing particles also varied over the course of an individual simulation, as we showed in Figure 5.1. Variation in the geometric mean diameter and in the geometric mean hygroscopicity parameter of BC-containing particles across all simulations are shown in Figures 5.4.c and 5.4.d, respectively. Figures 5.3 and 5.4 were constructed from data at 10-minute intervals in each of the 288 simulations, corresponding to 41,000 time steps.

Variance in the aging timescale is shown by the probability density distribution in Figure 5.5, which includes each 10-minute time interval in each of the 288 simulations. Distributions are shown for timescales computed at $s = 0.1\%$, $s = 0.3\%$, and $s = 1\%$. The supersaturation threshold s specifies the degree of change in particle properties required to classify a particle as aged, and timescales tend to decrease as s increases. In the following sections, we show that most of the variance in black carbon's aging timescale at a specific s is explained by only a few key variables.

5.4 Nonparametric regression analysis to quantify explained variance

Black carbon's aging timescale ranges from minutes to weeks (Figure 5.5), depending on local conditions and characteristics of BC-containing particles. We evaluated how well different combinations of independent

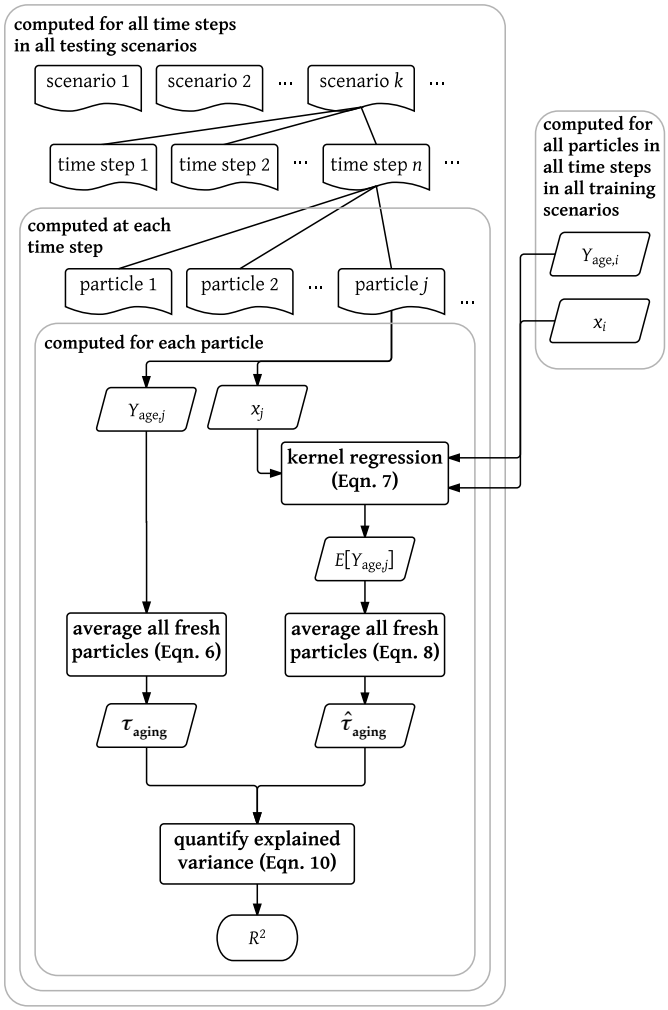

Figure 5.6: Procedure for applying kernel regression to predict black carbon's aging timescale and quantifying the portion of variance explained by that prediction, shown for a hypothetic input variable x.

Table 5.5: Candidate variables included in the regression analysis.

symbol	description	type
D	wet diameter	particle-level
D_{dry}	dry diameter	particle-level
κ	hygroscopicity parameter	particle-level
$\varepsilon_{\mathrm{BC}}$	mass fraction BC	particle-level
$\varepsilon_{\mathrm{SOA}}$	mass fraction SOA	particle-level
$\varepsilon_{\mathrm{inorg}}$	mass fraction inorganic aerosol	particle-level
N	overall aerosol number concentration	population-level
A_{wet}	aerosol surface area concentration	population-level
$\dot{V}_{\mathrm{cond}}$	secondary aerosol formation rate, volume	population-level
$\dot{f}_{\mathrm{cond}}$	secondary aerosol flux, $\dot{V}_{\mathrm{cond}}/A_{\mathrm{wet}}$	population-level
$\dot{m}_{\mathrm{cond}}$	secondary aerosol formation rate, mass	population-level
κ_{cond}	hygroscopicity parameter of secondary aerosol	population-level
N_{CCN}	number concentration of CCN-active particles	population-level
N_{large}	num. conc. of particles with $D > 100$ nm	population-level
$N_{\mathrm{CCN,large}}$	num. conc. of CCN-active particles with $D > 100$ nm	population-level

variables explain variance in black carbon's aging timescale by comparing predictions of aging timescales from nonparametric regression with exact aging timescales from PartMC-MOSAIC. A nonparametric regression was chosen, rather than a parametric regression, because we do not know a priori the shape of the predictor surface.

The procedure in applying a nonparametric regression is as follows: 1) select a set of candidate independent variables to test; 2) use most (90% of simulations) of the data as the training set to find the expected value of the aging timescale as a function of the independent variables, as will be explained below; 3) evaluate this expected aging timescale using the rest of the data (10% of simulations), called the testing set. The timescale from the regression is assessed by how well it predicts the values of the aging timescale in the testing set, represented by R^2. The purpose of this exploration is to find the independent variables that explain most of the variance in the aging timescale, indicated by the largest value of R^2. To ensure that our conclusions did not depend on the choice of scenarios, we repeated the analysis several times with randomly chosen testing and training sets and verified that R^2 was insensitive to the specific choice of testing and training sets.

5.4.1 Kernel density regression applied to particle-resolved model data

Figure 5.6 shows how the regression analysis is applied in this study. For all times in all simulations in the testing set, a particle that is fresh at time t may age between t and some later time $t + \Delta t$ or it may remain fresh over that time period. Because these two events are mutually exclusive, this aging behavior in PartMC-MOSAIC may be represented by a binary variable $Y_{\mathrm{age},j}(t, t + \Delta t, s)$, where $Y_{\mathrm{age},j} = 1$ if the

particle ages between t and $t+\Delta t$ and $Y_{\mathrm{age},j} = 0$ if it remains fresh. The aging timescale at each model time step can then be computed as the average of $Y_{\mathrm{age},j}$ across all fresh BC-containing particles:

$$\tau_{\mathrm{aging}}(t,s) = \Delta t \frac{N_{\mathrm{p,fresh}}}{\sum_{i=1}^{N_{\mathrm{p,fresh}}} Y_{\mathrm{age},j}(t, t+\Delta t)}, \tag{5.5}$$

which is equivalent to Equation 5.3, computed from $N_{\mathrm{p,fresh}}$ individual particles over a specific model time step.

Alternatively, the expected probability that a fresh particle will age, given its characteristics or the aging conditions that it experiences, can be estimated from a nonparametric regression. We applied the kernel density regression introduced by (143) and (97). The expected value of $Y_{\mathrm{age},j}$ for a specific particle in the testing set is predicted using the kernel density regression, using information about the candidate variable x_j only. The candidate variable x_j may be a particle-level characteristic, which varies between particles and, for a specific particle, varies over time (e.g. particle wet diameter). The candidate variable x_i may also be a characteristic of the environment, which varies over time but, at a specific time, is the same for all particles (e.g. aerosol number concentration). All candidate variables explored in this study are outlined in Table 5.5. In this section, we show how the nonparametric regression can be applied to evaluate variance explained by a single candidate variable at a time. Later, we show how this analysis can be extended to evaluate combinations of independent variables.

At each time step in each simulation of the testing set, the expected value of $Y_{\mathrm{age}}(t, t+\Delta t, s)$ for each particle was computed as a weighted average of $Y_{\mathrm{age},i}(t, t+\Delta t, s)$ for millions of individual particles in the training set. Values for $Y_{\mathrm{age},i}(t, t+\Delta t, s)$ in the training set are weighted according to the kernel function $K_h(x - x_i)$, where x is the independent variable of interest. The expected value of $Y_{\mathrm{age}}(t, t+\Delta t, s)$ is given by:

$$E\left[Y_{\mathrm{age}} \middle| x_j(t), \Delta t, s\right] = \frac{\sum_{i=1}^{N_{\mathrm{p,train}}} K_h(x_j(t) - x_i) Y_{\mathrm{age},i}}{\sum_{i=1}^{N_{\mathrm{train}}} K_h(x_j(t) - x_i)}, \tag{5.6}$$

where x_i is the value of the independent variable for each particle in the training set, x_j is the value of the independent variable for the target variable in the testing set, and $N_{\mathrm{p,train}}$ is all particles in the training set, including all time steps in all simulations.

Analogous to Equation 5.5, the expected value of the aging timescale at a specific model time step,

$\hat{\tau}_{\text{aging}}(t,s)$, is then computed as the average of $E\big[Y_{\text{age}}\big|x_j(t),\Delta t,s\big]$ across all BC-containing particles:

$$\hat{\tau}_{\text{aging}}(t,s) = \Delta t \frac{N_{\text{p,fresh}}}{\sum_{j=1}^{N_{\text{p,fresh}}} E[Y_{\text{age}}|x_j(t),\Delta t,s]}. \tag{5.7}$$

In Section 5.4.1, we provide further explanation on the inclusion of particle-level characteristics in the prediction of $\hat{\tau}_{\text{aging}}$.

In this study we used a Gaussian kernel function with standard deviation h:

$$K_h\big(x_j(t)-x_i\big) = \frac{1}{\sqrt{2\pi}h}\exp\left(-\frac{(x_j(t)-x_i)^2}{2h^2}\right). \tag{5.8}$$

The kernel function $K_h(x_j(t)-x_i)$ defines the weight applied to each model timescale $\tau_{\text{age,i}}$ to compute the expected timescale $\hat{\tau}_{\text{age}}$, such that timescales for conditions similar to the conditions of the target point are weighted most heavily in the regression. The regression function predicted by the kernel regression depends on the prescribed value for h, where larger h results in smoother regression functions. We applied Silverman's rule of thumb to select the value for h (124), such that h depends on the number of independent variables, the standard deviation of each independent variable, and the total number of data points in the testing set.

If the candidate variable x strongly affects the value of the aging timescale, the expected aging timescale $\tau\hat{\text{aging}}, j$ will accurately represent the actual aging timescale $\tau_{\text{aging},j}$, assuming a suitable kernel bandwidth h is applied in the kernel regression. Aging rates scale with the inverse of the aging timescale, so we quantified the variance explained by the regression function, R^2, in terms of $1/\tau_{\text{aging}}$:

$$R^2(s) = 1 - \frac{\displaystyle\sum_{j=1}^{n_{\text{test}}} N_{\text{fresh},j}(s)\left(\frac{1}{\hat{\tau}_{\text{aging},j}(s)} - \frac{1}{\tau_{\text{aging},j}(s)}\right)^2}{\displaystyle\sum_{j=1}^{n_{\text{test}}} N_{\text{fresh},j}(s)\left(\frac{1}{\hat{\tau}_{\text{aging},j}(s)} - \frac{1}{\bar{\tau}_{\text{aging}}(s)}\right)^2}, \tag{5.9}$$

where $\tau_{\text{aging},j}$ is the timescale from PartMC-MOSAIC for each data point in the testing set, $\hat{\tau}_{\text{aging},j}$ is the expected timescale from the regression for each data point in the testing set, $\bar{\tau}_{\text{aging}}$ is the harmonic mean of the aging timescales across all data points in the testing set, and N_{test} is the number of data points in the testing set, where the data points include all time steps in all scenarios.

5.4.2 Inclusion of particle-level variables in the kernel regression

To illustrate our approach for including particle-level variables, we demonstrate the regression procedure using the wet diameter as the independent variable x. The resulting regression surface is a size-dependent

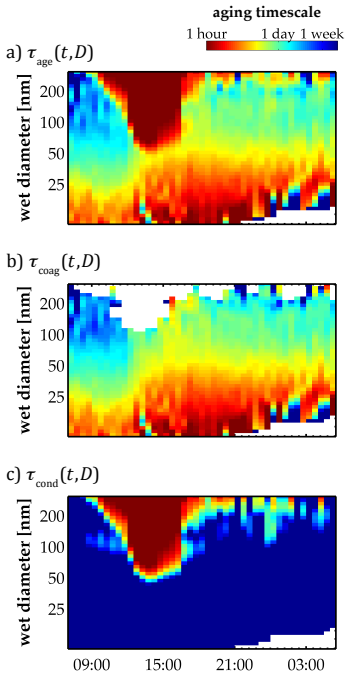

Figure 5.7: For baseline scenario, a) overall size-dependent aging timescale, b) condensation aging timescale, and c) coagulation aging timescale. Values are shown for $s = 0.3\%$.

timescale, which gives insight into the importance of aging processes as a function of particle wet diameter. For a given set of environmental conditions, some particles are more likely to age than others, and we find that a particles' tendency to age depends on their characteristics just prior to the aging period. We evaluated how aging rates vary with a number of per-particle characteristics, such as particles' diameter at emission, their dry diameter at the time when aging is evaluated, or their hygroscopicity parameter when aging is evaluated. We found that for given environmental conditions, per-particle aging rates were most correlated with the wet diameter of fresh (CCN-inactive) particles; that is, values of R^2 were greatest for regression functions that included the time-varying wet size distribution of fresh BC-containing particles.

It is therefore useful to introduce a size-resolved aging timescale that accounts for differences in aging rates between particles of different sizes. Size-resolved aging timescales were computed at each time t and supersaturation s using the kernel regression described in Section 5.4.1. The expected value of Y_{age} for a particle in the testing set with wet diameter $D_j(t)$ was computed as the weighted average of $Y_{\text{age},i}$ for rest particles the training set $i = 1, ..., N_{\text{p,train}}$, computed at a specific t and s:

for a particle in the testing set of wet diameter D_j was

$$E\left[Y_{\text{age}}|D_j(t),\Delta t,s\right]=\frac{\sum_{i=1}^{N_{\text{p,train}}}K_{h_D}(D_j(t)-D_i)Y_{\text{age},i}}{\sum_{i=1}^{N_{\text{p,train}}}K_{h_D}(D_j(t)-D_i)}, \tag{5.10}$$

where the kernel weighting function $K_h(D_j(t)-D_i)$ is a Gaussian (Equation 5.8), such that fresh particles with D_i similar to the target diameter D_j are weighted most heavily in the regression. The size-resolved aging timescale can also be defined for a continuous size distribution of fresh particles $n_{\text{fresh}}(t,D,s)$. Similar to Equation 5.7, the size-resolved aging timescale, $\tau_{\text{aging}}(D)$, is computed as a function of $E\left[Y_{\text{age}}|D\right]$ and the time step Δt:

$$\tau_{\text{aging}}(t,D,s)=\frac{\Delta t}{E\left[Y_{\text{age}}|D(t),\Delta t,s\right]}. \tag{5.11}$$

For a particle-resolved population of fresh particles $j=1,...,N_{\text{p,fresh}}$, where each particle has a unique wet diameter D_j, the bulk, population-level aging timescale can be estimated as the average of $E\left[Y_{\text{age}}|D_j(t),\Delta t,s\right]$ across all $N_{\text{p,fresh}}$ particles, as given in Equation 5.7 using $x_j=D_j$. Equivalently, the population-level aging timescale can be computed through the average of the continuous size-resolved aging timescale $\tau_{\text{aging}}(D,t,s)$, weighted by the size distribution of fresh particles $n_{\text{fresh}}(D,t,s)$: integration of the continuous size-resolved aging timescale $\tau_{\text{aging}}(D,t,s)$ over all D, continuous size distribution of fresh particle $n_{\text{fresh}}(D,t,s)$ as the average of $\tau_{\text{aging}}(D,t,s)$ across all D, weighted by the size distribution of fresh particles $n_{\text{fresh}}(D,t,s)$:

$$\tau_{\text{aging}}(t,s)^{-1}=\frac{\int_0^\infty \tau_{\text{aging}}(t,D,s)^{-1}n_{\text{fresh}}(t,D,s)dD}{\int_0^\infty n_{\text{fresh}}(t,D,s)dD}. \tag{5.12}$$

By this relationship, the bulk aging timescale under a specific set of environmental conditions also varies with the size distribution of CCN-inactive (fresh) BC.

The temporal evolution of the size-resolved aging timescale is shown for the baseline scenario in the middle column of Figure 5.7 for $s=0.3\%$. The contributions of coagulation (Figure 5.7.b) and condensation (Figure 5.7.c) to the overall aging timescale (Figure 5.7.a) are shown by the separate size-resolved timescales for each process. The dominant mechanism driving the aging timescale depends on the time of day and the particle size.

A comparison between Figures 5.7.a and 5.7.c shows that condensation was the dominant process driving diurnal variation in the size-resolved aging timescale. This diurnal pattern in condensation aging conditions is reflected in the bulk aging timescale shown in Figure 5.2. The bulk condensation aging timescale was shorter than 4 h during the day for this scenario, and this was the dominant process affecting aging rates

at this time. However, Figure 5.7.c shows that these rapid transitions from CCN-inactive to CCN-active occurred only for the largest ($D > 50$ nm) fresh particles, although condensation also caused an increase in D for smaller fresh particles. The coagulation aging timescale, on the other hand, was short for the smallest fresh particles and varied only slightly over the course of the simulation.

5.4.3 Combining particle-level and population-level variables in kernel regression

In this study, we performed a series of multivariate kernel regressions to identify the combination of independent variables that best explain variance in black carbon's aging timescale. In many cases, we extracted aging timescales that depend both on characteristics of individual particles, such as D, and on properties of entire particle populations or the environment, such as the overall aerosol number concentration N. One advantage of this approach is that both particle-level variables and population-level variables can be included in the prediction of $Y_{\text{age},j}$. For example, the expected value of $Y_{\text{age},j}$ for a particle with diameter D_j that is exposed to an aerosol number concentration N_j is computed with the bivariate kernel regression:

$$E\big[Y_{\text{age}}|D_j, N_j\big] = \frac{\sum_{i=1}^{N_{\text{p,train}}} K_{h_D}(D_j(t) - D_i) K_{h_f}(N_j(t) - N_i) Y_{\text{age},i}}{\sum_{i=1}^{N_{\text{p,train}}} K_{h_D}(D_j(t) - D_i) K_{h_f}(N_j(t) - N_i)}. \tag{5.13}$$

The overall aging timescale for a particular size distribution exposed to a specific number concentration is the computed as the sum across individual particles (Equation 5.7) or, equivalently, by integrating over the size distribution (Equation 5.12). Equation 5.13 can easily be generalized to three or more independent variables.

5.5 Independent variables that best explain variance in aging timescales

We found that most variance in the aging timescale is explained by only a few independent variables. Explained variance R^2 is shown different combinations of independent variables as a function of the environmental supersaturation s at which CCN activity is evaluated. For all supersaturation levels, 90% of variance in the coagulation aging timescale (Figure 5.8.a) was explained by regression predictions that included the size distribution of fresh BC-containing particles and the number concentration of large, CCN-active particles ($N_{\text{CCN,large}}$). Three variables were needed to explain 85% of variance in the condensation aging timescale

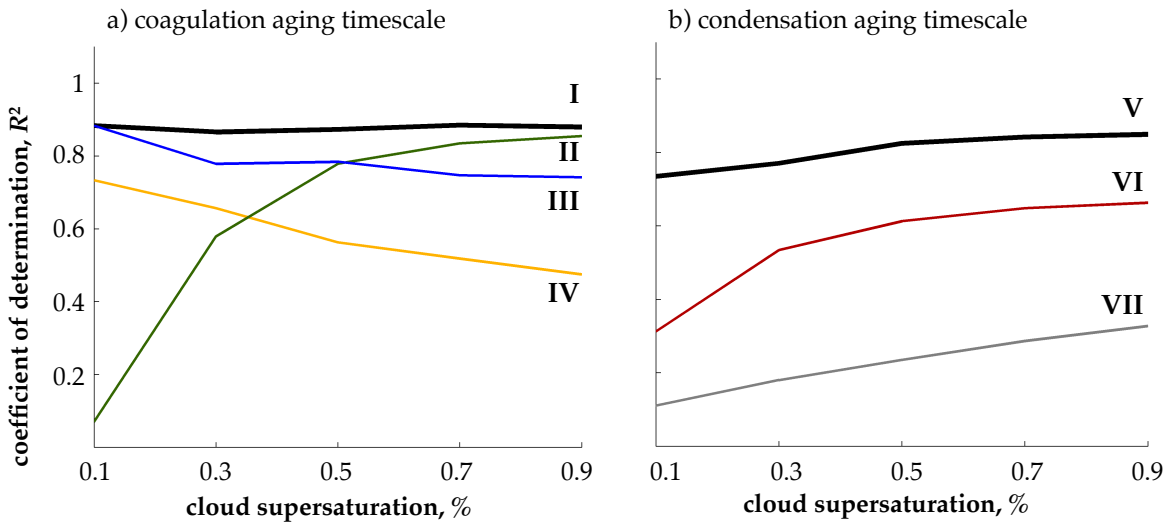

Figure 5.8: Coefficient of determination R^2 for a) coagulation and b) condensation timescales as a function of supersaturation for selected combinations of independent variables, where the combination of variables that explain most of the variance are shown by the black lines in each graph. Regression analyses on the coagulation aging timescales are shown for four combinations of independent variables: (I) including wet diameter, D, of fresh BC-containing particles and the number concentration of large ($D > 100$ nm), CCN-active particles, $N_{\mathrm{CCN,large}}$, (II) including D of fresh BC-containing particles and the number concentration of large particles, N_{large}, rather than $N_{\mathrm{CCN,large}}$, (III) including D of fresh particles and the number concentration of CCN-active particles, N_{CCN}, rather than $N_{\mathrm{CCN,large}}$, and (IV) including $N_{\mathrm{CCN,large}}$ but without including D of fresh BC-containing particles. Regression analyses on the condensation aging timescale are shown for three combinations of independent variables: (V) including secondary aerosol flux, $\dot{f}_{\mathrm{cond}}$, the hygroscopicity of secondary aerosol, κ_{cond}, and D of fresh BC-containing particles, (VI) including $\dot{f}_{\mathrm{cond}}$ and κ_{cond} but without including D of fresh BC-containing particles, and (V) including $\dot{f}_{\mathrm{cond}}$ and D of fresh BC-containing particles but without including κ_{cond}. For all s, approximately 90% of variance in coagulation aging timescale is explained by two independent variables (black line in Figure 5.8.a), and 80% of variance in condensation aging timescale is explained by three independent (black line in Figure 5.8.b).

(Figure 5.8.b): the size distribution of fresh BC ($n_{\text{fresh}}(D)$); the flux of secondary aerosol ($\dot{f}_{\text{cond}}$), defined as the volume condensation rate of semi-volatile substances per particle surface area density; and the effective hygroscopicity parameter of secondary aerosol (κ_{cond}), where κ_{cond} is the volume-weighted average of κ for condensing semi-volatile species. The size distribution of fresh BC was included in each case by determining a regression for the size-resolved aging timescale before computing the bulk aging timescale according to Equation 5.12. Only 10-15% of variance remains unexplained, indicating that variables other than $n_{\text{fresh}}(D)$, $\dot{f}_{\text{cond}}$, κ_{cond}, and $N_{\text{CCN,large}}$ also weakly taffect the value of the aging timescale.

Figure 5.8 shows the explained variance R^2 as a function of s for the independent variables that best explain variance in the coagulation and condensation aging timescales. Approximately 90% of variance in the coagulation aging timescale was explained by regressions in terms of $n_{\text{fresh}}(D)$ and $N_{\text{CCN,large}}$ (black line of Figure 5.8.a). Brownian coagulation events are most likely to occur between large and small particles, so the coagulation aging timescale decreases when there are more particles that are CCN-active and are also large enough to be good coagulation partners. The smallest fresh particles are likely to coagulate with large background particles, where we found the threshold for "large" to be $D > 100$ nm by identifying the threshold that resulted in the highest R^2. A regression computed in terms of the number concentration of large particles (green line of Figure 5.8.a), rather than the number concentration of large and CCN-active particles, gave $R^2 \approx$85% at high supersaturation thresholds ($s > 0.8\%$) but $R^2 < 10\%$ at low supersaturation thresholds ($s < 0.1\%$). This is because not all particles with $D > 100$ nm are CCN-active at $s = 0.1\%$, but nearly all particles that are CCN-active at this low s have $D > 100$ nm. On the other hand, if the independent variable was the number concentration of CCN-active particles (blue line of Figure 5.8.a), rather than the number concentration of large and CCN-active particles, $R^2 \approx 90\%$ for timescales at low supersaturation thresholds ($s < 0.1\%$) and $R^2 \approx 70\%$ at high supersaturation thresholds ($s > 0.8\%$). Only by considering the number concentration of particles that are both CCN-active and large, $N_{\text{CCN,large}}$ were we able to explain variance in the coagulation aging timescale at all supersaturation levels. If the size distribution of fresh BC was neglected, R^2 ranged from 40% to 60%, depending on the supersaturation threshold (yellow line of Figure 5.8.a).

While the expected aging timescale computed in terms of $n_{\text{fresh}}(D)$, $\dot{f}_{\text{cond}}$, and κ_{cond} (black line of Figure 5.8.b) explained greater than 80% of variance in the condensation aging timescale, R^2 was less than 60% for regressions that did not include $n_{\text{fresh}}(D)$ (red line). Only 10-30% of variance was explained if κ_{cond} was not included in the regression (grey line). If $\dot{f}_{\text{cond}}$ was not included, $R^2 \approx 0\%$ for all s, regardless of the other variables included in the regression (not shown). This suggests, not surprisingly, that the condensation rate is the key variable driving aging by condensation, but the condensation aging timescale also depends

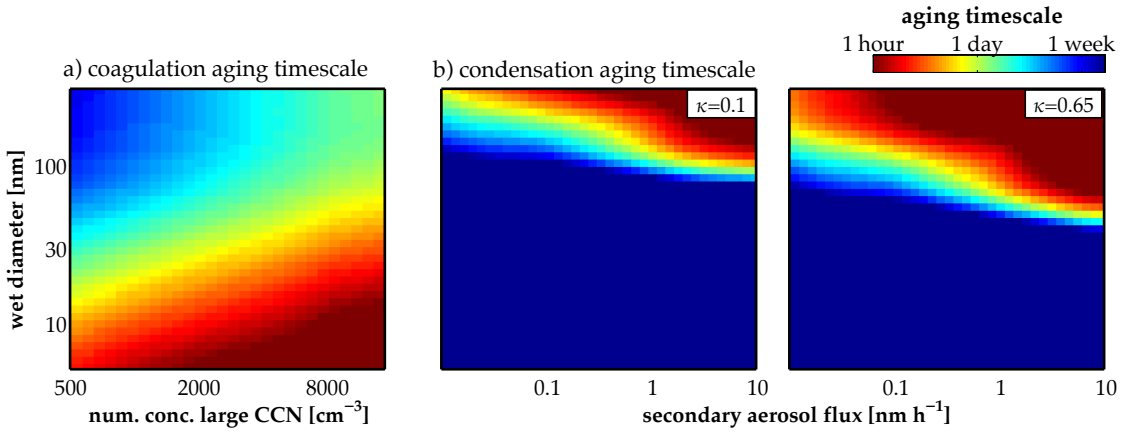

Figure 5.9: Coagulation aging timescale as a function of wet diameter and number of large, CCN-active particles (Figure 5.9.a) and condensation aging timescale as a function of wet diameter, secondary aerosol flux, and hygroscopicity of secondary aerosol (Figure 5.9.b). Results are shown for a threshold supersaturation s of 0.3%.

strongly on the hygroscopicity of condensing aerosol κ_{cond} and on the size distribution of fresh particles $n_{\text{fresh}}(D)$.

5.5.1 Aging timescales as a function of governing parameters

The regression surfaces $\hat{\tau}_{\text{coag}}(N_{\text{CCN,large}}, D)$ and $\hat{\tau}_{\text{cond}}(\dot{f}_{\text{cond}}, \kappa_{\text{cond}}, D)$ are shown in Figures 5.9.a and 5.9.b, respectively. Figure 5.9.a shows that timescales for aging by coagulation range from hours to weeks. The coagulation aging timescale decreases with the number concentration of "large", CCN-active particles ($N_{\text{CCN,large}}$) and, for a given $N_{\text{CCN,large}}$, small BC-containing particles are more likely to age by coagulation than large BC-containing particles. On the other hand, condensation aging timescales are shortest for the largest fresh particles and, for these particles, the condensation aging timescale tends to decrease as $\dot{f}_{\text{cond}}$ or κ_{cond} increase. The two panels of Figure 5.9.b show $\hat{\tau}_{\text{cond}}$ as a function of $\dot{f}_{\text{cond}}$ and D for secondary aerosol with differing hygroscopicity, $\kappa_{\text{cond}} = 0.65$ on the left, representing secondary inorganic aerosol, and $\kappa_{\text{cond}} = 0.1$ on the right, representing secondary organic aerosol.

5.5.2 Sensitivity of aging timescale to aging conditions

In this section we apply the regression surfaces shown in Figure 5.9 to selected example cases to demonstrate how aging conditions and the fresh particle size distribution affect particle aging rates. Figure 5.10 shows how aging rates by condensation and coagulation can be reconstructed as a function of the size distribution of fresh particles (Figure 5.10.a) and the size-resolve aging timescale (Figure 5.10.b). We compare lognormal

Table 5.6: Bulk aging timescale for two fresh particle size distributions under different aging regimes. Condensation, coagulation, and overall aging timescales are given for $s = 0.3\%$. We assumed lognormal size distributions of fresh BC with a geometric standard deviation of 1.7.

input variables			expected aging timescale		
			$s = 0.3\%$		
D_{gm} [nm]	$\dot{f}_{\mathrm{cond}}$ [nm h^{-1}]	$N_{\mathrm{CCN,large}}$ [cm^{-3}]	$\hat{\tau}_{\mathrm{cond}}$ [h]	$\hat{\tau}_{\mathrm{coag}}$ [h]	$\hat{\tau}_{\mathrm{age}}$ [h]
30	0.01	500	460	17	16
60	0.01	500	44	40	20
30	1	500	18	17	9
60	1	500	2.8	40	2.6
30	0.01	10,000	460	5	5
60	0.01	10,000	44	6	5.4
30	1	10,000	18	2.6	2.2
60	1	10,000	2.8	6	2

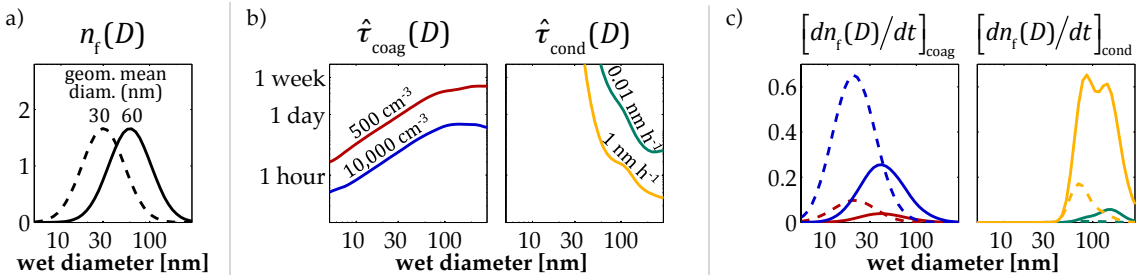

Figure 5.10: Rate at which particles of specific size transition from fresh to aged (Figure 5.10.c) depends on size distribution of fresh BC (Figure 5.10.a) and size-resolved aging timescale (Figure 5.10.b). Results are shown at $s = 0.3\%$, where the size-resolved aging timescale under different conditions are determined from the regression function in Figure 5.9. The line colors in Figure 5.10.c correspond to the aging conditions shown in Figure 5.10.b, and the line style in Figure 5.10.c correspond to the size distributions shown in Figure 5.10.a.

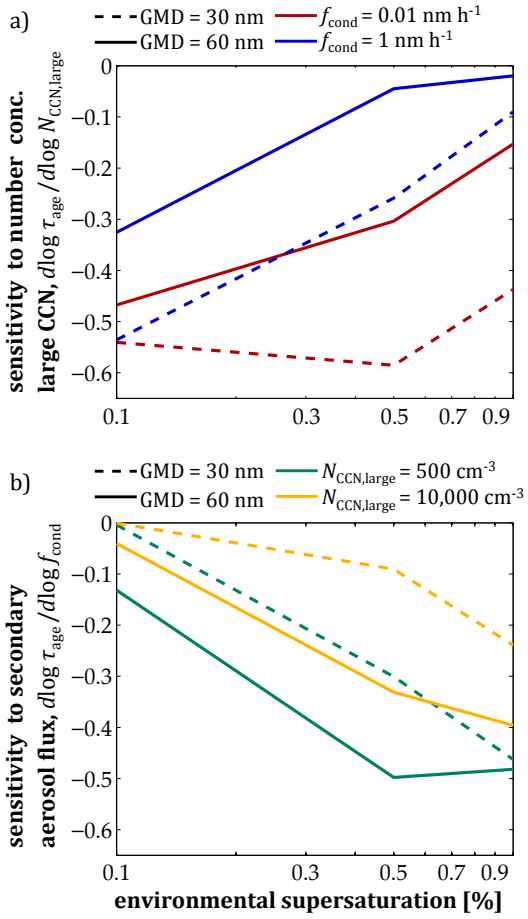

Figure 5.11: Sensitivity of aging timescale to a) $N_{\mathrm{CCN,large}}$ and b) $\dot{f}_{\mathrm{cond}}$ as a function of supersaturation level, expressed as the logarithmic derivative of the timescale with respect to each variable. The value of $d\log \tau_{\mathrm{age}}/d\log N_{\mathrm{CCN,large}}$, for example, indicates the relative change in τ_{age} to a relative change in $N_{\mathrm{CCN,large}}$. Shown for the size distributions and aging conditions in Figure 5.10.

size distributions with geometric mean diameter (D_{gm}) of 30 nm (dashed line of Figure 5.10.a) and 60 nm (solid line of Figure 5.10.a). Timescales were computed for limiting environmental conditions, indicated by line colors in Figure 5.10.b): slow coagulation aging ($N_{\mathrm{CCN,large}} = 500$ cm^{-3}, red line) or fast coagulation aging ($N_{\mathrm{CCN,large}} = 10,000$ cm^{-3}, blue line) and slow condensation aging ($\dot{f}_{\mathrm{cond}} = 0.01$ nm h^{-1}, green line) or fast condensation aging ($\dot{f}_{\mathrm{cond}} = 1$ nm h^{-1}, yellow line). Size-resolved aging timescales are taken from the regression surfaces in Figure 5.9 for these values of $\dot{f}_{\mathrm{cond}}$ and $N_{\mathrm{CCN,large}}$, assuming $\kappa_{\mathrm{cond}} = 0.65$ in both cases. Then, the rate at which particles of a given size transition from fresh to aged (Figure 5.10.c) is computed as the product of $n_{\mathrm{f}}(D)$ and $1/\tau_{\mathrm{age}}(D)$. Figure 5.10.c shows aging rates for particle distributions with $D_{\mathrm{gm}} = 30$ nm (dashed lines) and $D_{\mathrm{gm}} = 60$ nm (solid lines) under these limiting environmental conditions that promote rapid (blue lines) or slow (red lines) aging by coagulation and rapid (yellow lines) or slow (green lines) aging by condensation.

For these two size distributions (Figure 5.10.a) and different combinations of aging conditions (Figure 5.10.b), bulk aging timescales at $s = 0.3\%$ were computed according to Equation 5.12, and the results are given in Table 5.6. The combinations of environmental conditions are as follows: 1) rapid condensation aging (yellow lines in Figure 5.10.b) and slow coagulation aging (red lines), 2) slow condensation aging (green lines) and rapid coagulation aging (blue lines), 3) slow aging by both condensation and coagulation, and 4) rapid aging by both condensation and coagulation.

The sensitivity of the bulk aging timescales to $\dot{f}_{\mathrm{cond}}$ and $N_{\mathrm{CCN,large}}$ depends strongly on the environmental supersaturation s, as shown in Figure 5.11. At each supersaturation, sensitivities are quantified as a logarithmic derivative, or relative change in τ_{age} to a relative change in $\dot{f}_{\mathrm{cond}}$ or $N_{\mathrm{CCN,large}}$. Negative values oft his metric indicate that increasing $N_{\mathrm{CCN,large}}$ or $\dot{f}_{\mathrm{cond}}$ corresponds to a decrease in τ_{aging}.

While τ_{aging} is most sensitive to $N_{\mathrm{CCN,\ large}}$ at low supersaturation levels, τ_{aging} shows the greatest sensitivity to $\dot{f}_{\mathrm{cond}}$ at high supersaturation levels. At low supersaturation levels, τ_{aging} is insensitive to $\dot{f}_{\mathrm{cond}}$ if the distribution contains a higher fraction of small particles ($D_{\mathrm{gm}} = 30$ nm), regardless of conditions for aging by coagulation. If particles are large (D_{gm}=60 nm), τ_{aging} at this low s is τ_{aging} sensitive to $\dot{f}_{\mathrm{cond}}$ only under conditions of slow aging by coagulation. At $s = 1\%$, τ_{aging} is sensitive to $\dot{f}_{\mathrm{cond}}$ in all cases, regardless of the fresh particle size distribution or conditions for aging by coagulation. Coagulation aging is relatively more important at low supersaturation compared to high supersaturation thresholds. Consistent with this fact, Figure 11a shows that the sensitivity of the aging time scale to $N_{\mathrm{CCN,large}}$ generally decreases as s increases. The magnitude of the condensational flux $\dot{f}_{\mathrm{cond}}$ impacts the sensitivity towards $N_{\mathrm{CCN,large}}$. Environments with lower $\dot{f}_{\mathrm{cond}}$ result in a larger sensitivity to $N_{\mathrm{CCN,large}}$.

5.6 Discussion

Global models that employ first-order aging models assume a fixed timescale of 1–3 days, but observations show that aging timescales can be as short as a few hours in polluted areas (157). Other modeling studies have suggested parameterizations that account for this variation in aging conditions. (113) evaluated aging timescales in a mesoscale model and parameterized timescales for aging by coagulation as a function of the overall number concentration. (107) developed an analytical expression that accounts for decreases in the number concentration of primary aerosol through coagulation events; for emitted particles of a specific size, the coagulation loss rate was computed by integrating the coagulation kernel over the entire background size distribution. However, the regression analysis applied in the current study reveals that 90% of the variance in the coagulation aging timescale can be explained using a relatively simple representation of the background size distribution. We showed that the variation in the size-resolved aging timescales can be attributed to the number concentration of particles that are both large ($D > 100$ nm) and CCN-active. Other characteristics of the background size distributions are not needed.

(101) developed a parameterization of the condensation aging timescale based on results from a box model, and, similar to the present study, computed aging timescales based on changes in CCN activity. However, unlike the present study, (101) did not consider differences in the hygroscopic properties of the condensing material, and their aging timescale varied with the mass condensation rate per total BC mass concentration. In contrast, the regression analysis in the present study reveals that the volume condensation rate per overall aerosol surface area is the variable that best explains variance in BC's condensation aging timescale, which is consistent with laboratory studies (157; 70). The present work also differs from (101) in the representation of the aerosol size distribution. Whereas (101) parameterized bulk aging timescales for lognormal size distributions, we presented a size-resolved aging timescale that can be applied to any arbitrary size distribution.

As in all relationships for BC's aging timescale, the value of the aging timescale depends strongly on the criterion used to distinguish fresh and aged particles. Particle activation at a specific environmental supersaturation is the aging criterion applied in this study, representing changes in particle characteristics that most affect their susceptibility to wet deposition. Table 5.6 shows that the value of the aging timescale depends strongly on the criterion supersaturation at which CCN activation was evaluated, consistent with (114) and (101). Further, the relative importance of condensation versus coagulation as aging processes also depends on the supersaturation threshold.

5.7 Conclusions

This study identifies the minimal set of independent variables needed to explain variance in black carbon's aging timescale. We simulated the evolution of gases and aerosols in a series of urban scenarios with the particle-resolved model PartMC-MOSAIC and extracted time-dependent aging timescales based on the rate at which individual particles transition from CCN-inactive to CCN-active at a specified environmental supersaturation. The value of the aging timescale spanned orders of magnitude, depending on local environmental conditions and the supersaturation threshold at which CCN activity was evaluated. Aging timescales were shorter than an hour under conditions of rapid secondary aerosol formation, but on the order of days in the absence of secondary aerosol precursors. Condensation aging timescales exhibited more variation than coagulation aging timescales, and the relative importance of each aging mechanism depended on the size range of particles to be aged. We performed a non-parametric regression analysis on model data from 288 scenarios in order to identify the independent variables with which aging timescales are best correlated and quantified the portion of variance explained by regressions in terms of these variables. This paper is the groundwork for the development of aging parameterizations suitable for use in global models.

To our knowledge, this is the first study to apply a regression analysis to identify the minimal set of parameters needed to explain variance in black carbon aging rates. After evaluating a number of independent variables, we found that the flux of secondary aerosol, the hygroscopicity of secondary aerosol, and the size distribution of CCN-inactive (fresh) BC-containing particles were the minimal set of parameters needed to explain 80% of variance in the condensation aging timescale. On the other hand, 90% of variance in the coagulation aging timescale was explained by only two variables: the size distribution of fresh BC-containing particles and the number concentration of particles that are both large ($D > 100$ nm) and CCN-active. This work distills the complex interactions captured by the particle-resolved model to a few input variables, all of which are tracked by existing global climate models, and is a first step toward developing physically-based parameterizations of aerosol aging.

Chapter 6

Black carbon absorption at the global scale is affected by particle-scale diversity in composition

6.1 Introduction

Whereas Chapters 4 and 5 focused on identifying variables that most affect cloud condensation nuclei activity by particles containing black carbon (BC), here I identify factors that must be included to adequately represent light absorption by BC. One challenge in representing BC in global models is accounting for the microphysical particle details that affect light absorption and radiative transfer within these large models. Within individual particles, BC is mixed with other aerosol components to varying degrees (120; 81; 53), depending on the emission source (127; 135; 85; 54) and the extent of atmospheric processing (144; 146; 67; 142; 24). Models predict strong enhancement in light absorption by BC that is coated with non-absorbing aerosol components (59; 8; 27). However, recent ambient observations find only weak enhancement in light absorption by coated BC (21).

This discrepancy in modeled and observed light absorption indicates that the characteristics of BC-containing particles assumed in atmospheric models do not adequately represent real BC-containing particles found in the atmosphere. Models track limited information about the particle size distribution (11; 9), and often assume that, within each particle, BC forms a sphere and non-BC components form a uniform coating (59; 16). Models also approximate the representation of particle composition (145; 52; 56; 103; 11), assuming identical composition for particle of the same size (145; 56) or for particles of the same type (88; 11; 9). Whereas other studies have evaluated error in model-derived absorption from unrealistic representations of particle configuration (2; 122), this study focuses on error in modeled absorption from unrealistic representations of particle composition.

Treatments of aerosol composition vary between global models, from simple mass-based representations (25; 118), which do not track any information about particle size or composition, to modal (88; 11; 9) and sectional (145; 56) schemes, which simulate the evolution of the aerosol size distribution but assume that particles within the same mode or of the same size have the same composition. Because even the most sophisticated global models are not able to track characteristics of individual particles (9; 60), it

has not been possible to explore how microscale particle details influence macroscale radiative effects. In this study we apply a unique aerosol model that fully resolves the composition of individual particles, making it possible to evaluate how knowledge of particle-level composition impacts light absorption by BC. In particular, we compare 1) absorption enhancement by BC using particle-resolved composition and 2) absorption enhancement by BC using average composition across the population. Absorption enhancement (E_{abs}) is defined as the absorption by mixed BC-containing particles relative to absorption by the same amount of BC in pure, uncoated particles. We show that oversimplifying the representation of particle composition leads to overestimation in predicted absorption enhancement.

In order to identify factors affecting light absorption by BC, we performed a nonparametric regression on a series of simulations to identify the key independent variables that most affect E_{abs}. Through this nonparametric analysis we derived a relationship for E_{abs} as a function of population-averaged composition, computed by averaging across all BC-containing particles, and the environmental relative humidity, such that the relationship for E_{abs} accounts for particle-level variation in composition but depends only on variables that global models already track. Finally, we show how this nonparametric relationship can be exploited for use in global models to improve predictions of absorption by black carbon in climate simulations.

The results of this study will be published as a manuscript, likely in Geophysical Research Letters.

6.2 Modeling absorption by BC in individual particles

The particle-resolved model PartMC-MOSAIC (115; 151) was used to simulate realistic distributions of per-particle composition for populations of BC-containing particles. We considered 100 urban scenarios, varying gas and aerosol emissions, background aerosol concentrations, and meteorological conditions. PartMC-MOSAIC tracks the chemical composition of thousands of individual particles as they evolve by condensation of semi-volatile substances, coagulation between particles, aerosol emissions, and dilution with background air. This study presents simulations of 100 scenarios, which were constructed by sampling a large variable space using latin hypercube sampling. The input parameters that define this variable space are given in Table 6.1. PartMC version 2.1.4 was used for the simulations in this paper (available at: http://lagrange.mechse.illinois.edu/partmc/). Although the simulation settings differed, the structure of the scenarios was the same. In all scenarios, simulations started at 6:00 am, at which time air parcel contained only background air. From 6:00 am until 6:00 pm particles and gases were emitted into the air parcel. All emissions were discontinued at 6:00 pm, but all other processes continued until the simulations ended at 6:00 am the following day. As the simulations proceeded, we computed optical properties for BC populations

Table 6.1: Input variables assigned in sensitivity scenarios

environmental variable	**value**
temperature [K]	253 to 313
relative humidity	0% to 99%
boundary layer height [m]	200 to 500
dilution rate [$m^{-3}s^{-1}$]	1×10^{-5} to 2×10^{-5}
latitude range	0°N to 80°N
day of year	Jan. 1 to Dec. 31
aerosol characteristic	**value**
emission rate [kg m^{-2} s^{-1}]	1×10^{-12} to 1×10^{-11}
portion from biomass burning	0% to 70%
combustion particles from diesel	0% to 100%
background conc. [kg m^{-3}]	2×10^{-11} to 2×10^{-8}
portion back. in large mode	95% to 99%
aerosol type	**geo. mean dia. [nm]**
emitted from gasoline	70 to 100
emitted from diesel	70 to 100
emitted from biomass burning	100 to 200
small background	20
large background	116
emitted gas species	**rate [nmol m^{-2} s^{-1}]**
Ammonia	2×10^{-10} to 2×10^{-8}
Nitrogen oxide	6.4×10^{-11} to 6.4×10^{-8}
Nitrogen dioxide	3.36×10^{-12} to 3.36×10^{-9}
Sulfur dioxide	1×10^{-10} to 1×10^{-8}
Acetaldehyde	5.2×10^{-11} to 5.2×10^{-9}
Formaldehyde	5.2×10^{-11} to 5.2×10^{-9}
Ethene	6×10^{-10} to 6×10^{-8}
Terminal olefin carbons	1.94×10^{-10} to 1.94×10^{-8}
Internal olefin carbons	1.94×10^{-10} to 1.94×10^{-8}
Toluene	3.2×10^{-10} to 3.2×10^{-8}
Xylene	1.92×10^{-10} to 1.92×10^{-8}
Acetone	1×10^{-10} to 1×10^{-8}
Paraffin carbon	7.6×10^{-9} to 7.6×10^{-7}
Isoprene	1.86×10^{-11} to 1.86×10^{-9}
Methanol	2.28×10^{-11} to 2.28×10^{-9}
Alcohols	2.76×10^{-10} to 2.76×10^{-8}

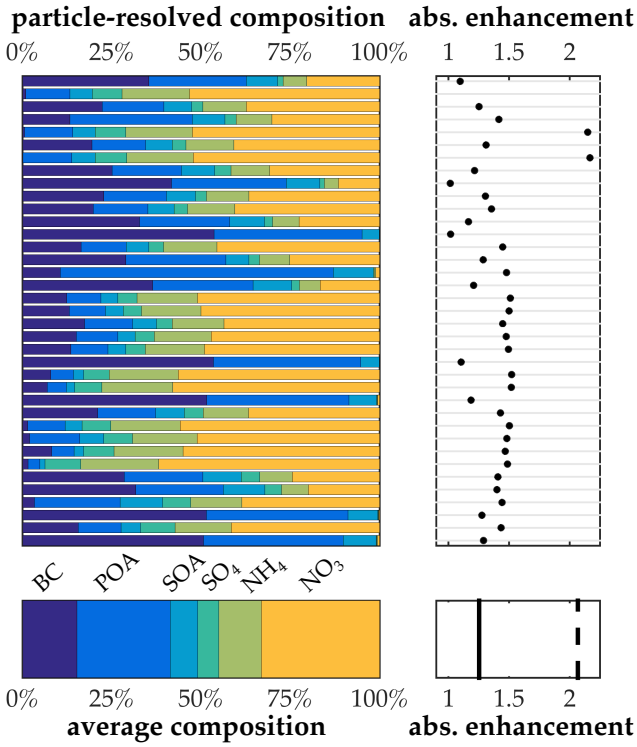

Figure 6.1: (a) Per-particle composition for subset of particles in a single population and (b) average composition of all-BC containing particles in that same population. (c) Per-particle absorption enhancement is computed from particle-resolved model data. (d) Overall absorption enhancement by BC in the population is computed from particle-resolved composition (solid line) and, for the same population, assuming uniform composition (dashed line).

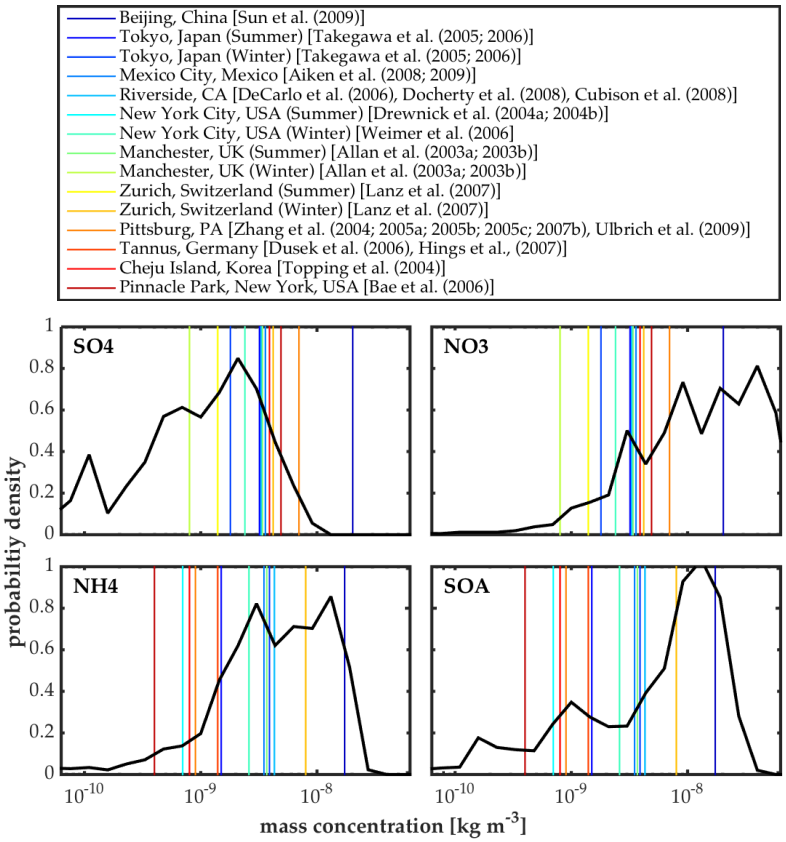

Figure 6.2: Variation in mass concentration of selected aerosol species across all simulation time steps (black line), compared with observed mass concentrations from various locations (colored vertical lines). Shows the range of aerosol concentrations from simulations corresponds covers variation in observed aerosol concentrations.

that were sampled from the scenarios periodically in order to include both fresh and aged populations. The simulations were designed to cover a range of atmospheric conditions, varying from heavily polluted conditions that promote rapid particle transformations to conditions with low gas and particle concentrations that promote slow particle transformations. Although several particle types were included in the simulations, this study focuses on the evolution of the BC-containing particles only, which originated from vehicle exhaust. These combustion particles were emitted as a mixture of BC and primary organic carbon, where the ratio of BC to organic carbon varied among simulations. After their emission, the combustion particles accumulated additional coating through condensation of semi-volatile gases and coagulation with background particles.

In the particle-resolved representation of composition, each particle is different, depending on how recently it was emitted, its composition at the time it was emitted, and the changes in composition that occurred since its emission. Applying the density for each species to the particle-resolved model output yields the volume of each species k contained in particle i, denoted $v_{1,k}$. Each particle is then represented by a vector

$\mathbf{v}_i = [v_{1,i}, ...v_{k,i}, ..., v_{A-1,i}]$, and the overall dry volume, $V_{\mathrm{d},i}$, of a given particle is given by:

$$V_{\mathrm{d},i} = \sum_{k}^{A-1} v_{i,k}. \tag{6.1}$$

The wide variation in per-particle composition represented by the particle-resolved model is illustrated in Figure 6.1a. Figure 6.1a shows a subset of particles sampled from a population of thousands of BC-containing particles, taken from a single scenario at a single time. From this particle-resolved model output, absorption by each individual particle was modeled as a function of its composition, the number of BC inclusions that it contains, and the environmental relative humidity. Rather than applying the simplified approximation that BC exists at the core in the center of each BC-containing particle, as in the widely-used core-shell approximation, we modeled particles using the dynamic effective medium approximation (**?** 63). Under this approximation, each particle is assumed to contain one or more randomly-distributed BC inclusions, where changes in number of inclusions through coagulation events are tracked by the particle-resolved model.

Absorption by BC populations from PartMC-MOSAIC are compared with the same population, but modeled assuming uniform composition across BC-containing particles. Under the uniform mixture approximation, each particle is represented by the vector $\tilde{\mathbf{v}}_i$. The amount of each species k in each particle i is adjusted such that the volume fraction of each species is the same for all particles, while the amount of BC in each particle is the same as in the particle-resolved representation:

$$\tilde{v}_{i,k} = v_{\mathrm{b},i} \frac{\sum_j^{N_{\mathrm{BC}}} v_{k,j}}{\sum_j^{N_{\mathrm{BC}}} v_{\mathrm{b},j}} \tag{6.2}$$

The overall dry volume under the particle-resolved representation, $\tilde{V}_{\mathrm{d},i}$, is computed from Equation 6.1, but using the composition vector $\tilde{\mathbf{v}}_{i,k}$ rather than $\mathbf{v}_{i,k}$.

Water uptake by each particle was modeled as a function of particle-level composition and the environmental relative humidity (RH) using the κ-Köhler model (104). As described in Chapter 3, the wet volume V_i is computed for each particle at each environmental relative humidity (RH) by applying the κ-Köhler model (104), which depends on the volume V_{d} and the effective hygroscopicity parameter κ_i of each particle. In the particle-resolved case, κ_i is computed from the composition predicted by PartMC-MOSAIC. Similarly, the effective hygroscopicity corresponding to the average composition, denoted $\tilde{\kappa}_i$, is computed in the same way as κ but using the composition from the uniform mixture approximation, $\tilde{\mathbf{v}}_i$. In order to explore all possible combinations of coating thickness and hygroscopicity, for each particle we considered ranges in κ for various aerosol species, as outlined in Table 6.1. Note that because particle wet volume depends on RH,

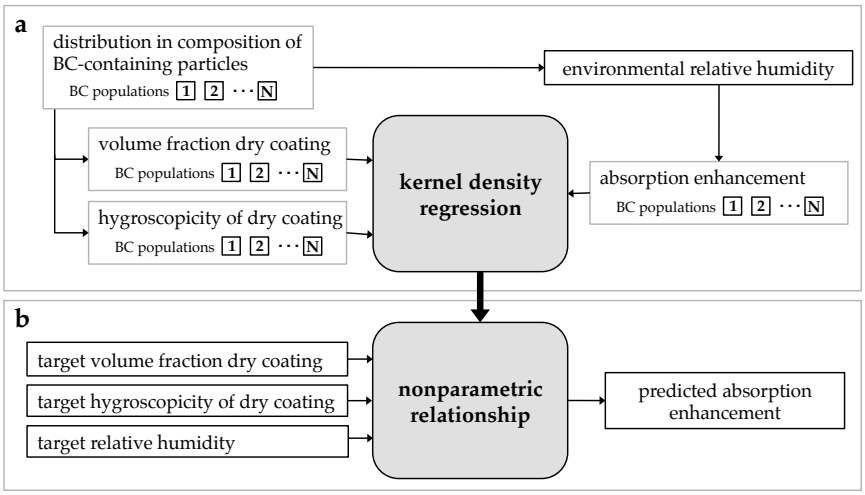

Figure 6.3: Procedure for applying nonparametric regression to particle-resolved model data in order to derive a relationship for absorption enhancement as a function of population-level variables.

Table 6.2: The range in values for κ assigned in simulations in Chapter 6, chosen based on (104) and references therein.

aerosol species	κ
NO_3	0.65–0.75
SO_4	0.65–0.75
NH_4	0.65–0.75
SOA	0.1–0.3
BC	0
POA	0.001–0.1

E_{abs} also depend on RH.

The absorption cross-section $\sigma_{\text{abs},i}$ of each particle i is computed using Mie theory, treating each BC-containing particle as an effective medium using the Dynamic Effective Medium Approximation (DEMA), as described in Chapter 3. The Mie model takes as inputs the wet volume V_i and the effective relative permittivity ϵ_i, which is computed from DEMA. Applying this DEMA model introduced by (31) and later applied to cloud droplets by (63), the effective relative permittivity ϵ_i for each particle $i = 1, ..., N_{\text{BC}}$ is computed as a function of the total volume of each particle (V_i), the volume of BC contained in each particle ($V_{\text{b},i}$), the relative permittivity of black carbon ($\epsilon_{\text{b},i}$), and the relative permittivity of each particle's non-BC coating ($\epsilon_{\text{c},i}$). The absorption cross section of particles under the uniform mixture approximation, $\tilde{\sigma}_{\text{abs},i}$, is computed in a similar manner, but using $\tilde{V}_i$ rather than V_i.

Enhancement in light absorption by BC within an individual particle i is then given by:

$$E_{\text{abs},i} = \frac{\sigma_{\text{abs},i}}{\sigma_{\text{core,abs},i}}. \tag{6.3}$$

Absorption enhancement by BC within individual particles is shown for RH=50% in Figure 6.1.b, corresponding to the particle composition shown in Figure 6.1.a. Within the same population absorption enhancement by BC within an individual particle from approximately one (no enhancement) to greater than two, depending on the particle's particular size and composition.

We define population-level absorption enhancement as the average absorption enhancement across all particles, each weighted by the uncoated absorption cross section. Absorption enhancement at the population-level, considering the all BC-containing particles, is computed from the particle-level data as:

$$E_{\text{abs}} = \frac{\sum_i^{N_{\text{BC}}} \sigma_{\text{abs},i}}{\sum_i^{N_{\text{BC}}} \sigma_{\text{abs,core},i}}, \tag{6.4}$$

where $\sigma_{\text{abs},i}$ is the absorption coefficient of each BC-containing particle $i = 1, ..., N_{\text{BC}}$, and $\sigma_{\text{abs,core},i}$ is the absorption coefficient by the same amount of BC but as a single, uncoated core.

Most aerosol models do not fully resolve diversity in particle composition. Instead, many simplified aerosol models track one or more separate populations of BC-containing particles but assume uniform composition across all particles within each population (131; 9; 5). Population-level absorption enhancement under the uniform mixture approximation is computed from the sum over $\tilde{\sigma}_{\text{abs},i}$ for all particles in the population:

$$\tilde{E}_{\text{abs}} = \frac{\sum_i^{N_{\text{BC}}} \tilde{\sigma}_{\text{abs},i}}{\sum_i^{N_{\text{BC}}} \sigma_{\text{abs,core},i}}, \tag{6.5}$$

Population-level absorption enhancement from PartMC-MOSAIC is shown by the solid line in Figure 6.1.d, and is 1.3 at RH=50%. Although a subset of only 30 particles is shown in Figures 6.1.a and 6.1.b, the overall absorption enhancement in Figure 6.1.d was computed from the thousands of BC-containing particles in the population. On the other hand, if the amount of BC in each particle is assumed to be the same as in the particle-resolved case but all BC-containing particles are assumed to have the average composition (Figure 6.1.b), we find E_{abs} greater than 2 (dashed line in Figure 6.1.d), overestimating modeled absorption by 50% relative to absorption derived from particle-resolved output.

This error in modeled absorption is caused by failure to capture the diversity in composition that is simulated by the particle-resolved model. Whereas the BC-containing particles simulated by the particle-resolved model are a mixture of thinly coated particles and thickly coated particles, the volume fraction of aerosol coating is the same across all BC-containing particles under the uniform mixture approximation. The largest BC inclusions, which contribute strongly to population-level absorption, tend be more thickly coated and more strongly absorbing under the uniform mixture approximation than they would be under the particle-resolved representation (not shown). For this reason, neglecting diversity in particle composition

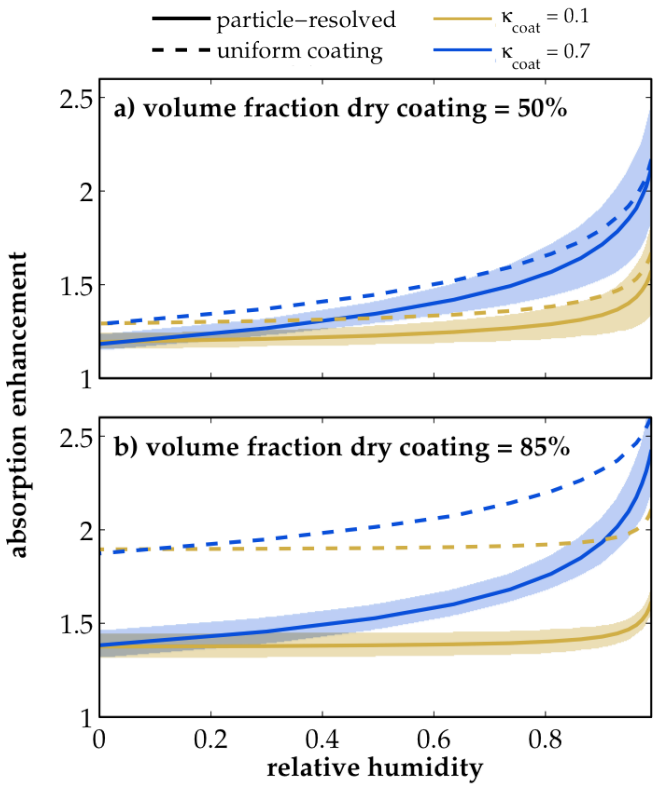

Figure 6.4: Relationship between absorption enhancement (vertical axes) and environmental relative humidity (horizontal axes), for varying average volume fraction of non-absorbing coatings (panels) and average hygroscopic parameter of the coating material (colors). Population-level absorption computed from particle-resolved composition are shown by solid lines. Shading shows the middle quartiles for the predictions, caused by differences in particle-level composition for populations that have the same average characteristics. The predictions of absorption enhancement based on particle-resolved composition (solid lines) are compared with predictions of absorption enhancement computed from uniform mixture approximation (dashed lines).

tends to cause an overestimation in modeled absorption.

6.3 Predicting population-level absorption enhancement

Most atmospheric models cannot represent particle-level absorption enhancement, but require a method to predict the overall absorption enhancement by all BC. In this section, we show how particle-resolved model simulations can be used to improve global model predictions of light absorption by BC. This section discusses a relationship, derived from particle-resolved model simulations, that predicts absorption enhancement using only variables that global models already track. The procedure for developing this relationship is shown in Figure 6.3. We constructed many scenarios, varying gas emissions, aerosol emissions, aerosol background concentrations, and meteorological conditions, and applied latin hypercube sampling (92) to sample the parameter space. The distribution in aerosol mass concentration within these simulations is shown for

selected species in Figure 6.2, which includes all time steps in all 100 scenarios. Surface observations of these aerosol species are indicated by the colored vertical lines in Figure 6.2. Figure 6.2 illustrates that aerosol concentrations simulated in the sampled scenarios represent the observed variation in surface aerosol concentrations.

We simulated a series of scenarios with PartMC-MOSAIC and computed population-level variables for N BC populations selected from various model time steps. Then, through a nonparametric regression (97; 143) on the particle-resolved model data (grey box in Figure 6.3.a), we developed a relationship for E_{abs} (grey box in Figure 6.3.b) that depends on variables that many global models already track: 1) the volume fraction of dry aerosol coating that is mixed with BC-containing particles (f_{coat}), 2) the hygroscopicity of the coating material (κ_{coat}), and 3) the environmental relative humidity (RH). The nonparametric regression predicts the expected value of E_{abs}, given the population-averaged composition. For a specific RH, values for E_{abs} were extracted from PartMC-MOSAIC scenarios at several model time steps, representing aerosol populations under a range of conditions that have been modified to varying degree. The expected value of population-level absorption enhancement, given a combination of k independent variables, is computed using the kernel density regression from (97; 143). The application of the kernel density regression to particle-resolved model data is explained in 5.

Inclusion of f_{coat}, κ_{coat}, and RH the best prediction of E_{abs} in comparison with particle-resolved model results ($R^2 = 85\%$). Other population-level variables, such as the mean refractive index of the coating or the mean diameter of BC inclusions, did no improve the fit. The average volume fraction of dry aerosol coating that is mixed with BC-containing particles and the hygroscopicity of the coating material were computed for each of the N BC populations. For varying RH, population-level absorption enhancement (e.g. solid line in Figure 6.1.d) was modeled for each of those N particle-resolved populations. The kernel density regression uses this population-level information to produce a nonparametric relationship that predicts E_{abs} as a function of the governing independent variables.

The relationship between absorption enhancement and the independent variables is shown in Figure 6.4. Absorption enhancement is shown as a function of the environmental relative humidity (horizontal axes) for populations that contain, on average, 50% dry coating by volume (top panel) and 85% dry coating by volume (bottom panel), assuming that coatings are, on average, hydrophobic ($\kappa_{\text{coat}} = 0.05$, orange) or hygroscopic ($\kappa_{\text{coat}} = 0.7$, blue), representing organic and inorganic coatings, respectively. The relationship for absorption enhancement shown here is based on the detailed distributions in particle composition simulated by PartMC-MOSAIC. This relationship allows the prediction of absorption enhancement for any value of f_{coat} or κ_{coat}, but, for simplicity, only a few combinations of f_{coat} and κ_{coat} are shown in Figure 6.4.

This nonparametric relationship, which uses only population-averaged composition information, is able to reproduce the population-level absorption enhancement with small errors. However, also shown in Figure 3 is the absorption enhancement that would be predicted by assuming each particle has the population-average composition and then calculating absorption (dashed lines). Error in modeled absorption from this simplified representation of particle composition is indicated by the difference between the solid and dashed lines.

For thinly coated particles, such as freshly emitted particles, simplifying the particle composition causes little error at all relative humidities. Comparison between the top and bottom panels demonstrates the effect of coating thickness on absorption enhancement. For the average-composition treatment (dashed lines), absorption enhancement increases as dry coating material is added to the particles, consistent with previous modeling studies (59; 27) and laboratory measurements (37). However, absorption modeled with particle-resolved composition (solid lines) gives only a weak enhancement with coating thickness at low relative humidity, consistent with ambient observations (21). This finding suggests that the diversity in composition across ambient particles leads to lower absorption than if the coating were uniformly distributed and explains why laboratory studies (37), which consider less diverse BC populations, also measure greater absorption enhancement than is observed for ambient particles.

Although E_{abs} by realistic populations is weak under dry conditions, absorption increases by as much as 50% for particles that take up water at high relative humidity. This finding suggests that high absorption enhancements may exist in humid regions of the atmosphere, even when observations taken under dry conditions do not capture this enhancement.

6.4 Estimating global-scale absorption enhancement

The relationship for absorption enhancement shown in Figure 6.4 was applied to global model fields generated by Goddard Institute for Space Studies (GISS) climate modelE (118) coupled to Multiconfiguration Aerosol Tracker of mIXing state (MATRIX) (9). MATRIX represents 16 aerosol modes, 7 of which contain black carbon. MATRIX is an aerosol scheme based on the quadrature method of moments (88) that represents the evolution of 16 aerosol modes. Operating within the general circulation climate modelE (118), MATRIX tracks two moments of each aerosol distribution, number and mass, and a single quadrature point, assuming lognormal size distributions for emissions and removal calculations. MATRIX simulates sulfate, nitrate, ammonium, aerosol water, black carbon, organic carbon, mineral dust, and sea salt within aerosol populations and evolves through nucleation, secondary aerosol formation, condensation, and coagulation. The setup of

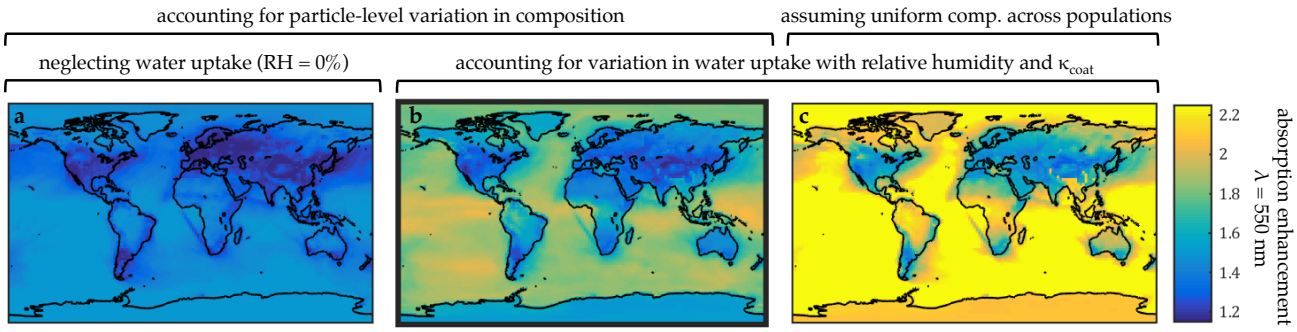

Figure 6.5: Spatial variation in absorption enhancement at the surface, computed from different representations of aerosol composition: (a) based on particle-resolved model data, assuming dry conditions (solid lines in Figure 6.4, RH=0%), (b) based on particle-resolved model data, accounting for water uptake (solid lines in Figure 6.4, RH from global model), and (c) assuming uniform composition across each BC population and accounting for water uptake (dashed lines in Figure 6.4, RH from global model).

the climate simulations discussed here are identical to (10).

Taking as inputs the relative humidity in each location, the mass concentration of BC in each mode, and the mass fraction of dry coating for each mode from GISS-MATRIX, we used the relationship shown in Figure 6.4 to estimate the global distribution in absorption enhancement by black carbon rather than applying the optics calculations from GISS-MATRIX. Spatial variation in the hygroscopicity of dry coatings (κ_{coat}) was estimated from (109). From the same climate model output, we modeled absorption enhancement assuming 1) absorption enhancement based on particle-resolved composition, but neglecting water uptake (Figure 6.5.a), 2) absorption enhancement based on particle-resolved model data and including water uptake in response to relative humidity (Figure 6.5.b), and 3) absorption enhancement based on uniform composition for BC populations, also including water uptake in response to relative humidity (Figure 6.5.c). Comparison between panels reveals that simplifying the representation of particle composition leads to overestimation of absorption enhancement in many locations (Figure 6.5.c), consistent with ambient observations (21). Using the most realistic relationship (Figure 6.5.b), based on particle-resolved composition and accounting for water uptake, the magnitude of absorption enhancement depends on the environmental relative humidity. Ambient particles are dried to RH≈50% prior to absorption measurements, so field studies are unable to observe this response in absorption enhancement to changes in relative humidity.

Figure 6.6 shows the distribution of absorption enhancement, weighted by BC mass. The dotted, solid, and dashed lines in Figure 6.6 correspond to the treatments represented in Figures 6.5.a, 6.5.b, and 6.5.c, respectively. However, Figure 6.5 includes BC mass throughout the entire atmosphere, whereas Figure 6.6 shows E_{abs} only at the surface.

Our best estimate of absorption enhancement, based on particle-resolved composition and including

aerosol water uptake (solid line in Figure 6.6), ranges from $E_{\text{abs}} = 1.1$ in some continental areas to E_{abs} greater than 2 in many marine areas, with a BC-weighted mean E_{abs} of 1.5. On the other hand, if we assume uniform composition among each BC population prior to computing absorption enhancement (dashed line in Figure 6.6), the global mean of E_{abs} is approximately 2, an overestimation of 30% in this mean value. If absorption is modeled based on particle-resolved composition, but without accounting for water uptake, absorption enhancement is underestimated in many locations (dotted line in Figure 6.6), leading to underestimation in global mean absorption enhancement by 15%.

6.5 Conclusions

Variation in particle composition within BC populations strongly affects modeled absorption. Absorption can be modeled with high accuracy using information that many global models already track when the relationship extracted form particle-resolved modeling is employed to account for diversity among particles in a single population. If particles within a population are assumed to have uniform composition, the prediction of absorption by black carbon is strongly enhanced ($E_{\text{abs}} > 2$) when BC is coated with non-absorbing aerosol, consistent with previous modeling studies (59; 27). If, instead, we account for particle-level variation in aerosol composition, weak absorption enhancement occurs at low relative humidity ($E_{\text{abs}} = 1.2 - 1.4$) that increases only slightly with the amount of coating material, consistent with ambient observations (21). Despite this limited enhancement at low relative humidity, absorption by BC is strongly enhanced at high relative humidity, increasing by more than 200% relative to dry conditions. The relationship for absorption enhancement presented in this study accounts for both particle-level variation in composition and water uptake, offering a computationally-efficient method to account for particle-level processes in existing global model frameworks.

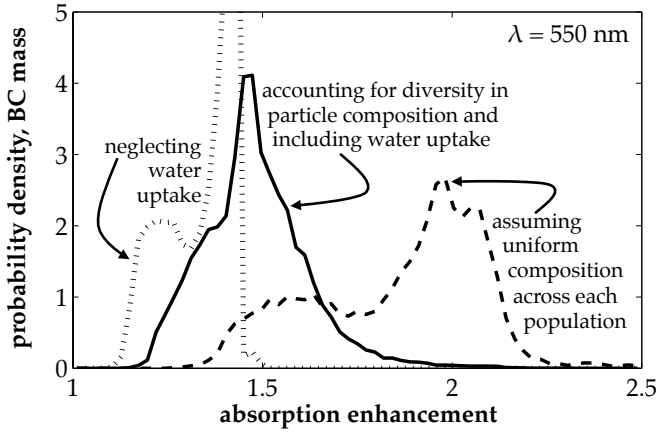

Figure 6.6: Probability density that BC mass takes on a particular absorption enhancement, for the different representations of particle composition. Solid line shows global distribution in absorption enhancement predicted from most realistic model, which accounts for water uptake and particle-level variation in composition. Absorption enhancement is underestimated if water uptake is neglected (dotted line) and is overestimated if we assume uniform composition across each BC population (dashed line).

Chapter 7

Parameterization of light absorption by BC for modal aerosol models

7.1 Introduction

Chapter 6 demonstrated that particle-level diversity across populations of particles containing black carbon (BC) must represented to adequately model light absorption by BC. However, representing this particle-level diversity in global-scale simulations is computationally challenging. In this study, we present a computationally-efficient representation of BC's absorption coefficient for modal aerosol schemes in regional-scale and global-scale models.

The absorption coefficient (b_{abs}) of an aerosol population is the integral over the absorption cross section σ_{abs} for each particle in the population, where σ_{abs} is modeled as a function of the characteristics of individual particles. In the atmosphere, particles containing black carbon exist in multicomponent aerosol particles of varied composition and morphology (78; 156), caused by variation in particle characteristics at emission(91) and by differences in their atmospheric transformations (41; 67). However, because global aerosol schemes cannot track the characteristics of individual particles, they must assume simple representations of aerosol composition (145; 56; 88; 11; 9). Global models must be able to accurately model absorption by these complex BC populations, using only limited information about particle microphysical properties.

Here we provide a parameterization of BC's absorption coefficient for use in modal and bulk aerosol models. Modal and moment-based models assume particles within the same mode or class have the same composition (88; 11; 9). To compute the absorption coefficient for the population b_{abs}, the continuous modal distribution is first separated into discrete size bins. The absorption cross section σ_{abs} is computed for representative particles within each size bin using Mie theory, assuming a simplified configuration and that all particles have identical composition. The absorption coefficient b_{abs} is then computed by integrating over the approximated values of σ_{abs} for each size bin, multiplied by the number concentration of particles in each size bin. In a previous study, we showed through comparison with a particle-resolved model, which resolves diversity within BC populations, that this simplified representation of composition leads to overestimation of black carbon's absorption enhancement by, on average, 30% (Chapter 6).

The present study builds on the work described in Chapter 6 and introduces a simple parametric relationship to compute BC's absorption coefficient. This parameterization is based on model output from the Particle Monte Carlo (PartMC) model (115) coupled to the Model for Simulating Aerosol Interactions and Chemistry (MOSAIC) (151). This parameterization predicts the absorption coefficient of populations of BC-containing particles, given the average volume fraction of dry aerosol coating for the population (f_{coat}), the hygroscopicity parameter of the coating material (κ_{coat}), the environmental relative humidity (RH), and the wavelength of light (λ). In this way, the simple parameterization approximately reproduces the absorption coefficient of BC populations as predicted by the particle-resolved model, which fully resolves particle composition, while taking as inputs only variables that modal models already track.

The results of this study will be published as a manuscript, likely in Atmospheric Chemistry and Physics.

7.2 Modeling light absorption by diverse BC populations with particle-resolved model

The relationship for BC absorption presented in this work was developed using absorption calculations on model output from PartMC-MOSAIC. Unlike other aerosol models, which approximate the representation of particle composition, PartMC-MOSAIC tracks the composition of each simulated particle. For this reason, PartMC-MOSAIC is uniquely suited to represent particle-level diversity in composition within aerosol populations. PartMC-MOSAIC tracks thousands of individual particles as their composition evolves by condensation of semi-volatile substances and coagulation with other particles.

Model output from a series of 100 scenarios was included in the regression analysis. The scenarios differed in meteorological conditions, emission rates of gas and aerosol species, background concentrations and the size distribution and composition of background and emitted particles. The full set of input parameters that were varied are outlined in Table 6.1. Scenarios were sampled from the larger variable space using Latin Hypercube sampling. The model scenarios are the same scenarios described in Chapter 6.

Similar to the approach applied in Chapter 6, the absorption cross section of each BC-containing particle was computed for aerosol populations using a combination of models as the simulations proceeded. The κ-Köhler model was used to determine water uptake as a function of relative humidity, which influences the overall amount of coating on BC-containing particles. The absorption cross section for wet particles at each relative humidity was then computed using Mie's model, which was combined with the Dynamic Effective Medium Approximation (DEMA) to estimate particle's effective refractive index. Several parametric regressions were then performed to find a relationship for BC's absorption coefficient. The results of this study

will be published as a manuscript, likely in Atmospheric Chemistry and Physics.

7.3 Parameterization of black carbon absorption

This study presents a parameterization for black carbon's absorption coefficient, which was constructed by combining three separate parameterizations. PartMC-MOSAIC scenarios were separated into randomly-selected testing and training sets. The training set, which contains most of the model data, was used to construct the parametric model. The rest of the PartMC-MOSAIC data was part of the testing set, and these scenarios were used to independently verify the parametric models. The regression coefficients for each parametric model were computed using iterative least squares estimation. Specifically, the Levenberg-Marquardt nonlinear least squares algorithm (121) was used to fit each parametric regression model.

The overall parameterization for black carbon's absorption coefficient (b_{abs}) is computed of the product of the absorption coefficient for a population of uncoated BC spheres ($b_{\text{abs,uncoat}}$) and the enhancement in absorption due to coatings (E_{abs}):

$$b_{\text{abs}} = E_{\text{abs}} b_{\text{abs,uncoat}} \tag{7.1}$$

This combined parameterization includes (1) a parameterization for the absorption coefficient for a population of uncoated BC spheres, (2) a parameterization for the enhancement in light absorption due to non-absorbing aerosol coatings, and (3) a parameterization for the further enhancement in absorption due to water uptake by the coating material in response to relative humidity. All parameterizations are expressed as a function of the wavelength of light, in addition to being functions of bulk properties of BC populations.

7.3.1 Absorption by populations of uncoated spheres

The absorption coefficient of a population of uncoated BC spheres in m^2m^{-3} is parameterized as a function of the BC mass concentration in kg m^{-3} and the wavelength of light in nm:

$$b_{\text{abs,uncoat}} = \Big(3.5 \times 10^4 - 24.5\lambda\Big) m_{\text{BC}}, \tag{7.2}$$

which indicates that the mass absorption cross section of BC in PartMC-MOSAIC depends on wavelength and very little on characteristics of the particle population, noting that in this study BC's refractive index was assumed to vary only with wavelength (e.g. Table 3.1).

Figure 7.1 shows the relationship between the absorption coefficient for uncoated spheres (vertical axis) and black carbon mass concentrations (horizontal axis). The model data from PartMC-MOSAIC that that

was used to construct the parametric relationship is shown by the colored dots, where the color indicates the wavelength of light at which $b_{\text{abs,uncoat}}$ was modeled. The parametric relationship constructed from the PartMC-MOSAIC data is shown by the colored lines.

7.3.2 Absorption by coated BC under dry conditions

When black carbon and other aerosol components exist in the same particle, model estimations find absorption by that particle is enhanced. However, in a previous modeling study we showed that absorption enhancement is overestimated if models do not account for particle-level diversity in composition. The parameterization for dry absorption enhancement ($E_{\text{abs,dry}}$) was constructed to approximately reproduce absorption predictions from particle-resolved model data. As such, this parametric expression estimates $E_{\text{abs,dry}}$ for diverse particle populations, while taking as inputs only population-level information on particle composition.

The enhancement in light absorption due to dry aerosol coatings is expressed as a function of the average volume fraction of non-BC coating material (f_{coat}) and the wavelength of light (λ):

$$E_{\text{abs,dry}} = \left(-0.05 - \frac{90}{\lambda} \right) \ln(1 - f_{\text{coat}}) + 1 \tag{7.3}$$

The relationship between dry absorption enhancement (vertical axis) and the volume fraction of dry coating f_{coat} (horizontal axis) is shown in Figure 7.2. As in Figure 7.1, model data from PartMC-MOSAIC is shown by the colored dots, and the parametric relationship is shown by the lines.

7.3.3 Absorption by coated BC under humid conditions

If BC-containing particles are coated with hygroscopic material, BC becomes more thickly coated as particles grow in response to relative humidity. This increase in coating material leads to a further increase in absorption. The response in absorption enhancement to relative humidity is included in the parameterization using an amplification factor, which depends on the environmental relative humidity and the hygroscopicity of the coating. The amplification factor was constrained to ensure that it is always greater than or equal to one. The full expression for absorption enhancement, accounting for water uptake, is given by:

$$E_{\text{abs}} = E_{\text{abs,dry}} \left[\left(\left(0.014 + \frac{12}{\lambda} \right) \ln(1-\kappa_{\text{coat}}) + \left(0.03 + \frac{92}{\lambda} \right) \ln(1-\kappa_{\text{coat}}) \ln(1-f_{\text{coat}}) \right) \ln(1-\text{RH}) + 1 \right]. \tag{7.4}$$

The overall absorption enhancement, therefore, depends on the average volume fraction of dry coating (f_{coat}), the average hygroscopicity of that coating (κ_{coat}), the environmental relative humidity (RH), and

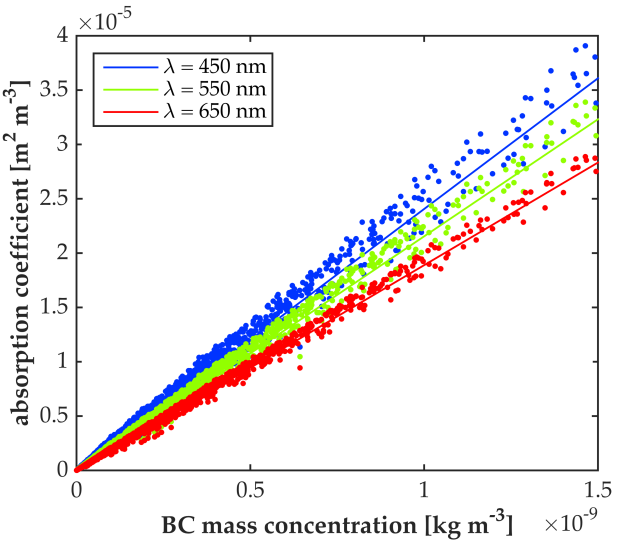

Figure 7.1: Absorption by uncoated BC spheres ($b_{\mathrm{abs,uncoat}}$) as a function of the BC mass concentration (m_{BC}), shown for different wavelengths (colors). Values for $b_{\mathrm{abs,uncoat}}$ computed directly from PartMC-MOSAIC (dots) are compared with $b_{\mathrm{abs,uncoat}}$ parameterized from Equation 7.1.

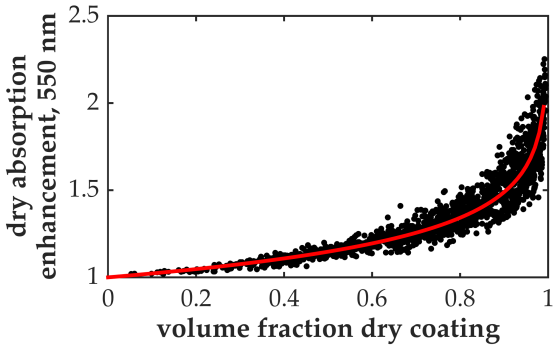

Figure 7.2: Dry absorption enhancement ($E_{\mathrm{abs,dry}}$) at $\lambda = 550$ nm as a function of the average volume fraction of dry coating (f_{coat}). Parameterization of $E_{\mathrm{abs,dry}}$ from Equation 7.3 (blue line) approximately reproduces $E_{\mathrm{abs,dry}}$ from particle-resolved model, while $E_{\mathrm{abs,dry}}$ is consistently overestimated if variation in particle composition is neglected and, instead, all BC-containing particles are assumed to have the same composition (red dots).

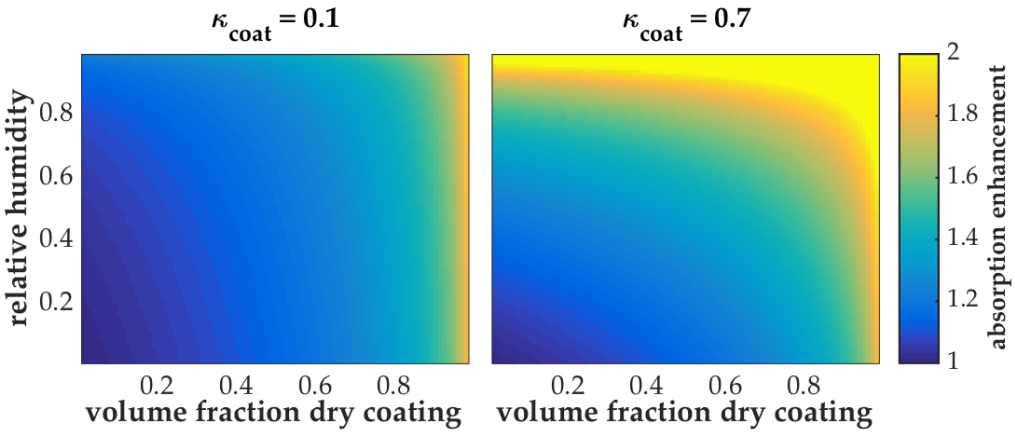

Figure 7.3: Paramterization for absorption enhancement as a function of the volume fraction of dry aerosol coating (horizontal axis) and relative humidity (vertical axis), applying two different values for the hygroscopicity of the coating. Absorption enhancement under dry conditions is the same for both graphs, shown by comparing E_{abs} at RH= 0% between the two axis. As expected, E_{abs} shows greater sensitivity to relative humidity if coated with hygroscopic aerosol (right axis) than hydrophobic aerosol (left axis).

the wavelength of light (λ). The multiplication factor accounts for the fact that the response in E_{abs} to water uptake depends on the volume fraction of dry coating, f_{coat}. If the population is, on average, thinly coated, increases in coating thickness by water uptake strongly enhance absorption. If the population is, on average, thickly coated, E_{abs} is less sensitive to further increases in coating due to water uptake.

The parameterization for E_{abs} is shown in Figure 7.3. Note that BC's absorption enhancement, E_{abs}, is equivalent to the dry absorption enhancement, $E_{\text{abs,dry}}$, if the environmental relative humidity is 0% or if the particles are coated with completely hydrophobic material ($\kappa_{\text{coat}} = 0$). On the other hand, if coatings are at least somewhat hygroscopic, absorption enhancement increases as RH increases. Similarly, at elevated relative humidities, absorption enhancement depend strongly on the hygroscopic properties of the coating material. Additionally, if particles are uncoated ($f_{\text{coat}} = 0$), $E_{\text{abs}} = 1$, and absorption enhancement is independent of RH or κ_{coat}.

7.4 Improvement in absorption estimations over models that neglect diversity in composition

The parameterization for b_{abs} described in the previous section reproduces the particle-resolved model data with high accuracy ($R^2 = 99\%$). On the other hand, absorption is consistently overestimated if particle diversity and, instead, all particles within each BC population are assumed to have identical composition, similar to the representation in modal models. Figure 7.4 shows a) the normalized mean squared error

(NMSE) and b) the mean bias in black carbon's absorption coefficient as a function of wavelength, using different approximations of aerosol properties.

Applying the full parameterization described in Equations 7.2–7.4 to PartMC-MOSAIC data in the testing set, we find only small errors in the modeled absorption coefficient. The NMSE for the parameterization ranges from 1-5% (blue line in Figure 7.4.a), depending on wavelength. On the other hand, if composition diversity within each population is neglected, as is common in modal and bulk aerosol models, NMSE ranges from 20-60% and the mean bias ranges from 20-40% (purple lines in Figures 7.4.a and 7.4.b, respectively), where the greatest errors occur at the shortest wavelengths.

Figure 7.4 also demonstrates the error caused by neglecting parts of the parameterization. If we neglect changes in absorption with coatings, and instead parameterize black carbon as uncoated using Equation 7.1, absorption enhancement is underestimated by 20-40% (yellow line in Figure 7.4.b), corresponding to a NMSE of 20-50% (yellow line in Figure 7.4.a). On the other hand, if BC is assumed to be mixed with dry aerosol components but water uptake is neglected, that applying the absorption enhancement given in Equation 7.3 and omitting Equation 7.4, absorption is underestimated by 10-22% (red line of Figure 7.4.b).

,

7.5 Conclusions

The present work introduces a simple parameterization that can be used to model absorption by BC populations in bulk and modal aerosol models. Based on model simulations by PartMC-MOSAIC, I developed a parameterization that predicts the absorption coefficient of BC populations, which adequately reproduces absorption predictions from the diverse aerosol populations simulated by PartMC-MOSAIC, but takes as inputs only variables that global models already track: 1) the mass concentration of BC, 2) the average volume fraction of dry aerosol coating, 3) the hygroscopicity of that coating, 4) the environmental relative humidity, and the wavelength of light.

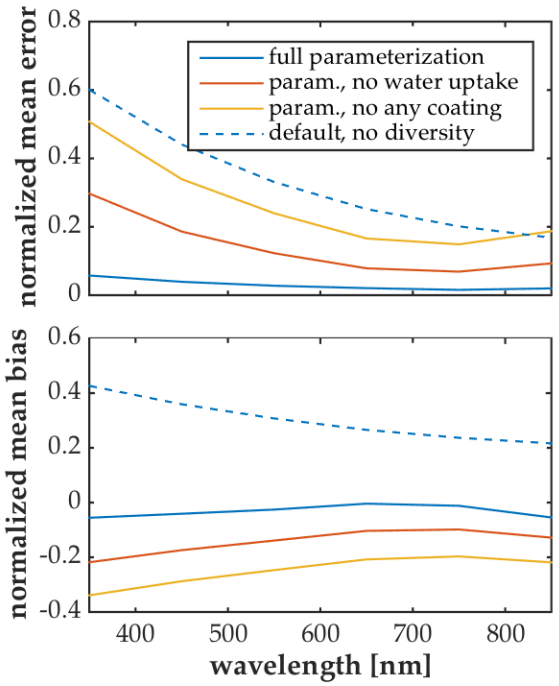

Figure 7.4: a) Normalized mean factor error and b) normalized mean factor bias in BC's absorption coefficient (b_{abs}), under different approximations, compared with absorption coefficient computed directly from PartMC-MOSAIC. Full parameterization (Equations 7.2–7.4), yields small error in b_{abs} (blue lines). If all BC-containing particles are assumed to have identical composition, absorption is overestimated (purple lines). Absorption is underestimated if BC is modeled as uncoated (orange lines) or if water uptake by dry coatings is neglected (red lines).

Chapter 8

Identifying the minimal representation of the aerosol composition

8.1 Introduction

The findings in Chapter 4–8 showed how particle composition, and changes in composition after emission, affect cloud condensation nuclei activity and aerosol absorption by BC populations. In the present study, I build on the previous findings to comprehensively evaluate error in the prediction of climate-relevant aerosol properties due to simplified representations of aerosol composition that are commonly applied in global models. Chemical transport models have moved toward including aerosol microphysical schemes that simulate aerosol evolution. The two major aerosol climate impacts depend on the optical properties and the cloud droplet activation of individual particles, which, in turn, depend on particle size, shape, and composition. These characteristics vary widely between particles at emission, and are further modified through aerosol aging processes, such as condensation of semi-volatile substances, coagulation with other particles, and photochemical reactions. Particle-scale properties cannot be resolved in global-scale simulations, so models approximate how aerosol components are distributed among individual particles. The errors in aerosol climate impacts introduced by such approximations can be large, but have not yet been well quantified. This chapter introduces a metric to address the question, "What is the minimal representation of aerosol composition required to accurately estimate the optical properties and the cloud-nucleating properties of aerosol populations?" Based on detailed particle-resolved simulations we derive a characteristic timescale of aging after which cloud condensation nuclei concentration can be accurately estimated using only the average composition of the aerosol population. To accurately calculate optical properties, in contrast, more detailed information of particle-level aerosol composition is needed, even for highly aged particle populations.

Computationally efficient representations of aerosol particles are needed for regional-scale and global-scale models of aerosol transport and fate, including those used in climate simulations. Ambient measurements show tremendous variation in composition between particles (120; 81; 53), even for particles of the same size. This reflects differences in emission sources (127; 135; 85; 54) and in the aging that each particle experiences during transport (144; 146; 67; 142; 24). This particle-level variation in aerosol composition

cannot be resolved in large-scale chemical transport models, so models approximate the manner in which aerosol components are distributed between individual particles, termed the "aerosol mixing state." It is not known to what extent mixing state needs to be tracked for accurate representation of climate-relevant properties, such as particle optical properties or their interactions with cloud droplets.

Depending on the makeup of a particular aerosol population, differences in composition between individual particles may affect prediction of direct and indirect aerosol radiative effects. For example, whereas most particles are predominantly light-scattering and cause a cooling effect on the climate, particles containing absorbing components, such as black carbon (BC), exert a warming effect on the climate. Model predictions of aerosol direct radiative effects depend not only on the overall abundance of absorbing and scattering species, but also the distribution in these species between individual particles (59; 27). Similarly, interactions between aerosols and clouds depend on the ability of individual particles to form cloud droplets, which depends on theirs size and composition. In air supersaturated with water vapor, particles may act as cloud condensation nuclei (CCN), depending on the environmental supersaturation and the characteristics of individual particles, in that large, hygroscopic particles activate more readily then small, hydrophobic particles. In some cases, resolving these differences in hygroscopic properties between particles affects estimates of CCN activity by the particle population (38; 42).

Aerosol schemes in chemical transport models track variation in particle composition to varying degrees. The simplest representations model the evolution of bulk aerosol mass without resolving any information about variation in particle composition but, rather, all particles in a given location are assumed to have the same composition (52; 58) known as the fully-internal mixture approximation (Figure 8.5a), or to contain only a single species (103; 33), known as the fully-external mixture approximation. More sophisticated aerosol schemes simulate the evolution of the aerosol size distribution while resolving limited information about the distribution in components across the particle population. For example, some models simualte the evolution of particles within separate size bins (145; 56), known as sectional models, or within separate aerosol distributions (11; 9), known as modal models, assuming that particles within a given size bin or mode have the same composition. Given the unique characteristics of black carbon, such as its strong absorption, several sectional schemes have been developed that either track separate aerosol populations (e.g. 60), where each distribution represents particles binned as a function of size, or track multivariate distributions (e.g. 102; 87), where particles are binned as a function of size and some other independent variable (e.g. BC mass fraction). Although these more complex sectional schemes resolve some information about the variation in aerosol composition between particles of the same size, even these complex schemes do not fully resolve the aerosol mixing state.

Although simplified treatments of the aerosol mixing state may not represent the composition of real ambient aerosol populations, the extent to which mixing state needs to be resolved in aerosol models has not yet been demonstrated. For example, for CCN activity of aerosol in remote or rural regions, Dusek et al. (39) showed that particle size is the dominant factor, and not aerosol mixing state. Several other studies confirmed that in regions far away from emissions sources, after all particles have aged, CCN activity can be accurately modeled if the underlying aerosol is assumed to be a full internal mixture (42). On the other hand, near emission sources the same approximation leads to overestimation in CCN concentrations (38; 42). While these observations demonstrate a change in the state of the aerosol, they do not describe the processes that led to the evolution of this mixing state.

This study, for the first time, quantifies the timescale for particles to transform from an external mixture, in which freshly emitted particles have distinct hygroscopic properties from the background, to an internal mixture, where it is appropriate to assume the same hygroscopic properties for all particles. We used the Particle Monte Carlo (PartMC) model coupled to the Model for Simulating Aerosol Chemistry and Interactions (MOSAIC), which fully resolves the aerosol mixing state, to simulate the evolution of individual particles under a range of atmospheric conditions. This particle-resolved model tracks the size and composition of individual particles as the population evolves by condensation of semi-volatile substances and particle coagulation. For different stages of the aerosol evolution, we evaluated how resolution of particle-level composition influences the prediction of aerosol optical properties and CCN activation. We show that, after particle characteristics are modified by condensation and coagulation, CCN activity can be modeled with high accuracy using simple representations of particle composition, and we quantify the timescale for aging as a function of the overall aerosol number concentration and volume condensation rate of secondary aerosol. In contrast, to simulate aerosol absorption with high accuracy particle-level variation in composition needs to be resolved. We found that resolving differences in the amount of BC between particles is important for modeling their CCN activity and, more so, their optical properties and, through this analysis, identified the minimal representation of aerosol composition.

The results of this study will be published as a manuscript, likely in the Journal of Aerosol Science.

8.2 Evolution of the aerosol mixing state

PartMC-MOSAIC was used to simulate the evolution of fresh combustion particles, which are hydrophobic and absorb solar radiation, that had recently been emitted into air parcels that contains background particles, which are hydrophilic and are purely light-scattering. In this way, the simulations were designed to analyze

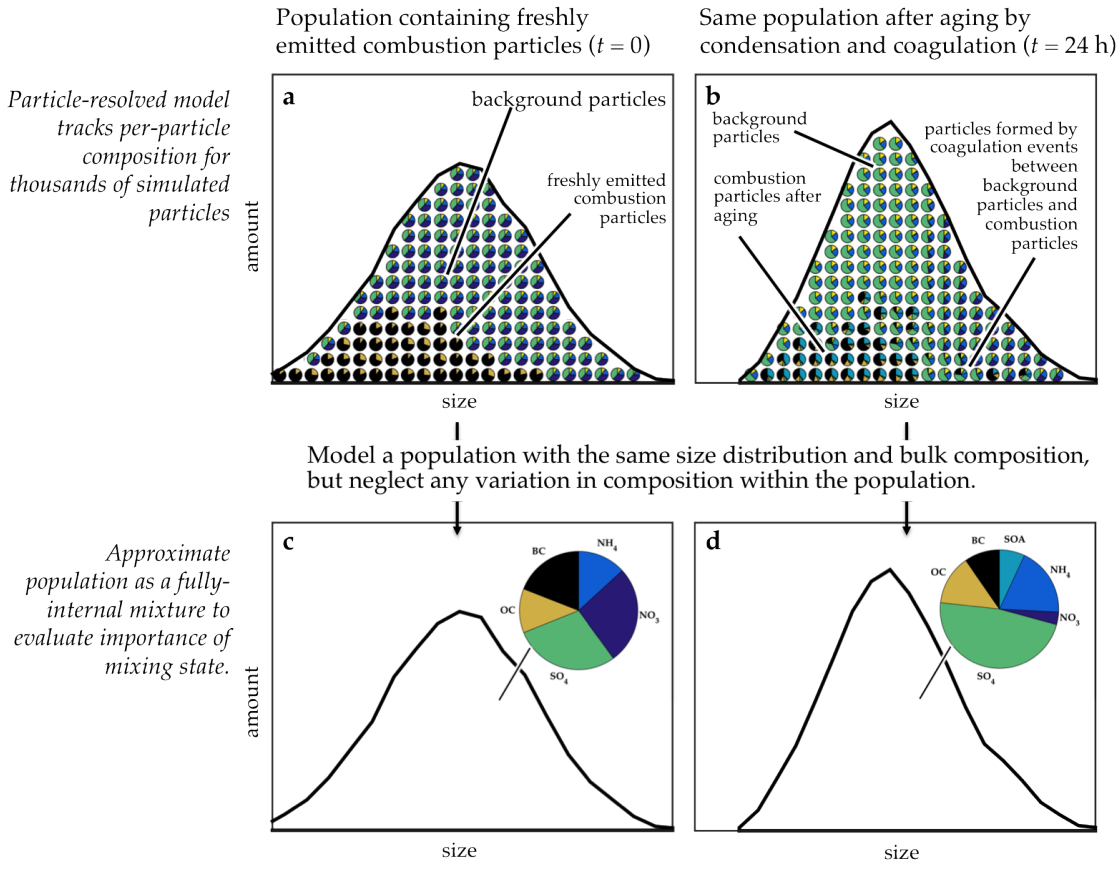

Figure 8.1: The particle-resolved model simulations started with a) an external mixture of background particles and combustion particles. As the simulation proceeds, the composition of individual particles are modified by condensation and coagulation. In addition to combustion particles and background particles, a new class of particles is formed by between these two particle types. The b) aged aerosol populations are comprised of diverse, multi-component particles. We quantify the importance of representing variability in particle composition by comparing CCN activation and optical properties computed from the particle-resolved representation (shown in a and b) with a population having the same size distribution and bulk composition, but in which all particles are assumed to have identical composition (c and d).

whether particles that are initially distinct in their optical properties and hygroscopic properties become sufficiently mixed through aging processes that their properties can be modeled without resolving particle-level detail. Further, the combination of the primary aerosol species was selected to represent aerosol in urban atmosphere, where details on the mixing state are known to be important. The combustion particles contain black and organic carbon, whereas the background particles contain organic carbon, ammonium sulfate, and ammonium nitrate, where the volume fraction of each species varies between the simulations. As the simulations proceeded, particles were modified through condensation of semi-volatile gases and coagulation between particles, processes collectively referred to as "aging", but no fresh particles were introduced after the simulation started, ensuring that all changes in aerosol composition were caused by aging only. The rates of transformation differed between scenarios, caused by variation in gas emissions, particle concentrations, and environmental conditions.

The particle evolution in a single scenario is illustrated in Figure 8.1. The simulation is initialized with two particle types, shown in Figure 8.1a. As the simulation proceeds, the composition of all particles are modified through condensation of semi-volatile substances and coagulation between particles. Coagulation between combustion particles and background particles yields a third class of particles that are distinct in composition from the two initial classes, shown in Figure 8.1b. Although the aerosol population simulated by PartMC-MOSAIC is complex, with tremendous variation in per-particle composition, it is unclear whether or not this particle-level detail influences the prediction of CCN activation and aerosol absorption. In order to evaluate the importance of the aerosol mixing state, we compare CCN concentrations and the absorption coefficient (1) modeled using the per-particle composition information from PartMC-MOSAIC (Figures 8.1a and 8.1b), which is the most detailed representation of particle composition with these quantities, (2) modeled the same population but without resolving any variation in particle-level composition and, rather, assuming the volume fraction of components within each particle is the same as the bulk average (Figures 8.1c and 8.1d).

8.3 Influence of mixing state on CCN activity

Figure 8.2 shows the number concentration of CCN as a function of the environmental supersaturation for a single particle population as it would appear immediately after the introduction of fresh particle emission (Figure 8.2a) and as it would exist after all particles have aged (Figure 8.2b). Figures 8.2c 8.2d show the amount of variability in particle hygroscopicity, caused by variation in per-particle composition, affects prediction of the CCN activity shown in Figures 8.2a and 8.2b, respectively. Each particle's critical supersaturation for CCN activation is computed as a function of its dry diameter and its hygroscopicity

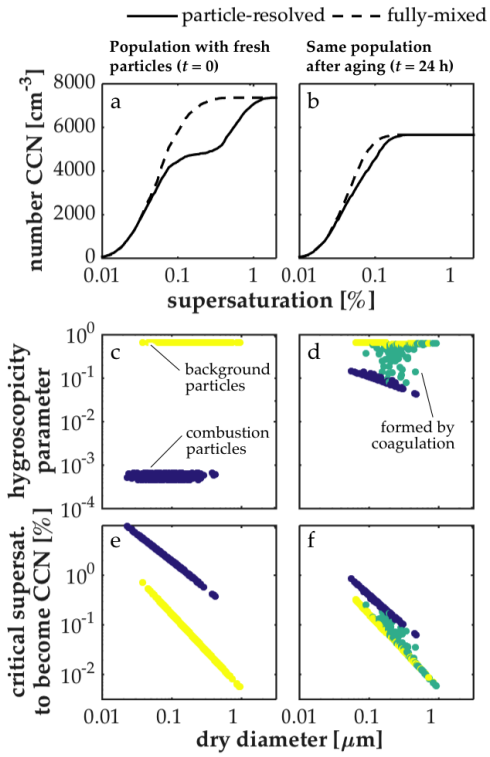

Figure 8.2: Number concentration of cloud condensation nuclei as a function of environmental supersaturation a) for a population containing freshly emitted particles, sampled at the start of the simulation ($t = 0$), and b) for the same population after all particles have aged ($t = 48$ h). The fully-internal mixture approximation does not capture the c) variability in particle hygroscopicity that is typical of air masses containing fresh emissions, so even e) particles of the same size may activate at different environmental supersaturaiton levels. After aging, d) particle hygroscopic properties are nearly uniform across the particle population, such that f) particles' critical supersaturation varies only with particle size and not due to differences in composition.

parameter (κ). The parameter κ has been determined empirically for a number of aerosol species, and the effective hygroscopicity parameter for a multi-component particle is given by the volume-weighted average of κ for its constituent species (104). Therefore, the effective κ for each particle depends on the assumed mixing state. Under the particle-resolved representation, κ freely varies between particles, whereas all particles have the same κ if they are assume to be fully mixed.

Figure 8.5a represents particle populations near emission sources, which contains a mixture of freshly emitted combustion particles and background aerosol. At the time they are emitted, combustion particles are much more hydrophobic than the pre-existing background particles (Figure 8.2c). If all particles are assumed to have uniform composition, the freshly emitted particles are modeled as being more hygroscopic than actually are, resulting in an overestimation in modeled CCN concentrations at certain cloud supersaturation levels (Figure 8.2a).

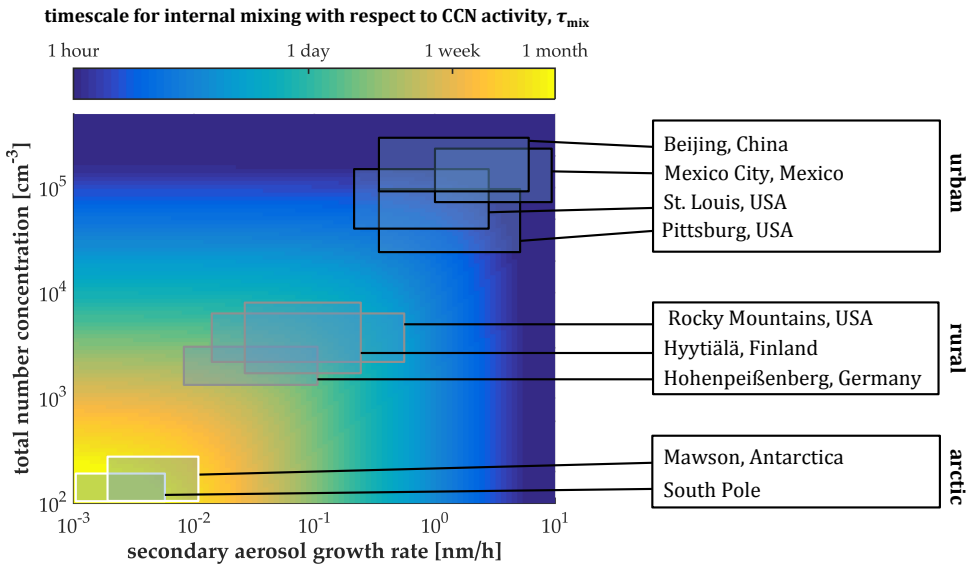

Figure 8.3: Estimated e-folding time of the error in CCN activity from the internal mixture approximation τ_{mix}. Ranges in aerosol growth rates and number concentrations that were inferred from measurements are indicated for specific locations. Values for τ_{mix} are shorter than an hour in most urban areas, indicating the particles emitted in these area become internally mixed soon after emission. Only in very remote regions, such as the Arctic, is τ_{mix} longer than a few days.

On the other hand, Figure 8.5b represents the same population of particles shown in Figure 8.5a but after all particles in the population have aged. Combustion particles increase in hygroscopicity soon after emission by condensation and coagulation, such that, in this case, after only a few hours of aging all particles had nearly the same hygroscopic properties and CCN activation depended only on particle size (Figure 8.5d). Once all particles have aged, the full internal mixture approximation (dashed line of Figure 8.5b) was sufficient for modeling CCN activity, indicating that the mixing state need not be resolved to model CCN activity by aged aerosol. This finding is consistent with observations in non-urban areas (39; 42).

8.4 Timescale for internal mixing

Similar to the case shown in Figure 8.2, across many simulations we found that error in modeled CCN concentrations from the fully-mixed approximation decayed as particles aged in the atmosphere (see Methods). We refer to the transformation in hygroscopic properties of particle emissions as aging with respect to their CCN activity. The timescale for this aging depends on characteristics of the local chemical environment, as was found in 5.

We quantified the timescale for particles to become internally mixed with respect to their CCN properties, τ_{mix} in a series of 100 particle-resolved scenarios, which were designed to cover a range of atmospheric

conditions. The range of input parameters assigned in the scenarios are given in Table 8.1. Scenarios were sampled from the large variable space using Latin Hypercube sampling.

Table 8.1: Input variables assigned in sensitivity scenarios

environmental variable	**value**
temperature [K]	253 to 313
relative humidity	0% to 99%
boundary layer height [m]	200 to 500
dilution rate [$m^{-3}s^{-1}$]	1×10^{-5} to 2×10^{-5}
latitude range	0°N to 80°N
day of year	Jan. 1 to Dec. 31
aerosol characteristic	**value**
combustion particles from diesel	0% to 100%
background conc. [kg m^{-3}]	2×10^{-11} to 2×10^{-8}
aerosol type	**geo. mean dia. [nm]**
combustion	70 to 100
background	100 to 200
emitted gas species	**rate [nmol m^{-2} s^{-1}]**
Ammonia	2×10^{-10} to 2×10^{-8}
Nitrogen oxide	6.4×10^{-11} to 6.4×10^{-8}
Nitrogen dioxide	3.36×10^{-12} to 3.36×10^{-9}
Sulfur dioxide	1×10^{-10} to 1×10^{-8}
Acetaldehyde	5.2×10^{-11} to 5.2×10^{-9}
Formaldehyde	5.2×10^{-11} to 5.2×10^{-9}
Ethene	6×10^{-10} to 6×10^{-8}
Terminal olefin carbons	1.94×10^{-10} to 1.94×10^{-8}
Internal olefin carbons	1.94×10^{-10} to 1.94×10^{-8}
Toluene	3.2×10^{-10} to 3.2×10^{-8}
Xylene	1.92×10^{-10} to 1.92×10^{-8}
Acetone	1×10^{-10} to 1×10^{-8}
Paraffin carbon	7.6×10^{-9} to 7.6×10^{-7}
Isoprene	1.86×10^{-11} to 1.86×10^{-9}
Methanol	2.28×10^{-11} to 2.28×10^{-9}
Alcohols	2.76×10^{-10} to 2.76×10^{-8}

The error in CCN concentrations from assuming a fully-mixed population decays exponentially with an e-folding time of τ_{mix}, where τ_{mix} can be parameterized as a function of local environmental variables. Based on analysis in a previous study (44), we parameterized τ_{mix} as a function of the condensational growth rate I_{cond} [nm h^{-1}], defined as the volume condensation rate of semi-volatile gases per wet surface area, and the overall number concentration N [cm^{-3}]:

$$\tau_{\text{mix}} \approx \left(k_{\text{cond}} I_{\text{cond}} + k_{\text{coag}} N \right)^{-1}, \tag{8.1}$$

such that τ_{mix} decreases as either I_{cond} or N increase. The value of the coefficients are $k_{\text{cond}} = 0.2$ nm^{-1} and $k_{\text{coag}} = 6 \times 10^{-6}$ cm^3 h^{-1}.

The regression coefficients k_{cond} and k_{coag} were estimated from linear regression. The 100 PartMC-MOSAIC scenarios were first divided into a set of 80 training scenarios, which were used to find the regression coefficients, and 20 testing scenarios, which were used to test the parametric relationship against the particle-resolve model. Equation**??** was reformulated, applying the expression for τ_{mix} from Equation 8.1:

$$\ln\left(\frac{\varepsilon(t)}{\varepsilon_0}\right) = k_{\text{cond}} \int_0^t I(t)dt + k_{\text{coag}} \int_0^t N(t)dt, \tag{8.2}$$

where the integrals over $I(t)$ and $N(t)$ are extracted from the particle-resolved model output in the training set, as are $\varepsilon(t)$ and ε_0. By this relationship, the timescale τ_{mix} represents the time $t = \tau_{\text{mix}}$ for $\varepsilon(t)$ to decrease to an e^{th} of its original value.

By this definition of aging, fresh particle emissions are those that have distinct hygroscopic properties from the background and, therefore, cannot be treated as fully-mixed with the background. After all emitted particles haves aged, under this definition of aging, variation in particle-level composition between emitted and background particles does not affect CCN activity. This first-order model with timescale τ_{mix} adequately models the transition from externally mixed populations to internally mixed populations ($R^2 = 0.8$).

Figure 8.3 shows τ_{mix} as a function of the condensational growth rate $I_{\text{cond}}(t)$ and the aerosol number concentration $N(t)$. To estimate the values of τ_{mix} expected in the atmosphere, we inferred the quantities I_{cond} and N from ambient observations in various locations. The ranges in aerosol number concentrations and growth rates were estimated from observations discussed in Kulmala et al. (79) and references therein. Average growth rates were computed from the growth rates observed during nucleation events using the diurnal and annual variation in growth rates taken fromVan Dingenen et al. (139), Spracklen et al. (129), or Tunved et al. (136), depending on the location.

If I_{cond} exceeds 1 nm h^{-1}, which is typical of many urban areas, and if no fresh particles are entering the population, the particle population becomes internally mixed within a few hours, regardless of the value for $N(t)$. Only under conditions with very slow condensational growth and low particle concentrations do particles remain externally mixed with respect to their hygroscopic properties for weeks, but these conditions occur only in remote areas that have few fresh particle emissions.

8.5 Influence of mixing state on aerosol absorption

Although, CCN concentrations can be modeled with high accuracy without any information about particle composition after all particles have aged, in this section we show that simple representations of aerosol composition lead to large error in modeled absorption. Figure 8.4 shows the absorption coefficient as a

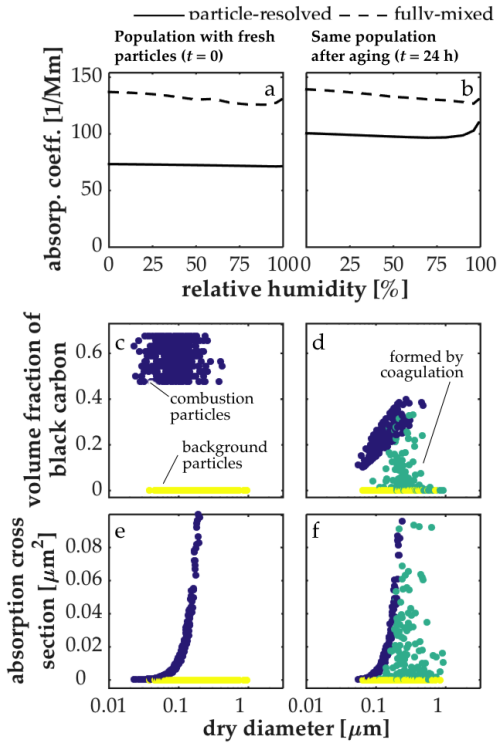

Figure 8.4: Aerosol absorption coefficient at $\lambda = 550$ nm as a function of relative humidity a) for a population containing freshly emitted particles, sampled at the start of the simulation ($t = 0$), and b) for the same population after all particles have aged ($t = 48$ h). The volume fraction of BC contained in each particle varies between individual particles if c) the population contains fresh emissions or d) if all particles have aged. This variation in the amount of absorbing material contained in each particle leads to variation in particles' absorption cross section for both e) populations containing freshly emitted particles and f) populations in which all particles have aged.

function of relative humidity for the baseline scenario, modeled using the particle-resolved (solid line) and fully-mixed (dashed line) representations. Whereas the fully-mixed approximation was sufficient for modeling CCN activity after all particles had aged for 24 hours (Figure 8.2), the fully-mixed approximation yields large error in modeled absorption even after emitted particles have aged. The influence of particle composition on absorption at the per-particle level is shown in Figures 8.4c and 8.4d, computed at a relative humidity of 50% and a wavelength of 550 nm. The variation in particle-level properties shown in Figures 8.4c and 8.4d corresponds to the population-level absorption coefficients shown in Figures 8.4a and 8.4b, respectively.

Similar to CCN activation, light absorption by an aerosol particle also depends on its size, shape, and chemical composition. Here we assume spherical particles, containing randomly-distributed BC inclusions (see Methods), and apply modeled size and composition. Although BC is strongly absorbing (117), most other aerosol components only scatter light. Further, absorption by black carbon may be enhanced if BC and non-absorbing aerosol material co-exist in the same particle (59; 16), and absorption by black carbon is further increased if particles take up water at high relative humidity (94; 64).

The simulation was initialized with a mode of particles containing BC that are strongly light-absorbing and background particles that only scatter light (Figure 8.4e). As the simulation proceeded, emitted particles coagulated with background particles, increasing absorption by the initially BC-free particles (Figure 8.4d). However, many of the background particles remained free of BC after even hours of simulation (Figure 8.4d). Treating this complex aerosol population as a fully-mixed population artificially places small amounts of black carbon in each particle and, as a result, particles that should be purely scattering are wrongly assumed to absorb light under this approximation. As a result, absorption is overestimated if complex particle mixtures are assumed to have uniform composition, even after long periods of aging in the atmosphere.

8.6 Error from common approximations of aerosol composition

The fully-mixed approximation cannot be used to accurately model CCN concentrations in populations containing fresh emissions or absorption by populations containing black carbon. In this section, we look beyond the fully-mixed approximation to evaluate how resolution of aerosol composition affects prediction of CCN concentrations and aerosol absorption. There are several ways to resolve variability in composition across the particle population. We evaluated several approximate representations of particle composition to quantify how resolving differences in composition between particles affects prediction of climate-relevant aerosol properties:

1. *fully-mixed*: assume all particles have the same composition, in that the volume fraction of the constituent aerosol species in each particle is the same as their bulk volume fraction,

2. *size-resolved*: assume particles within a given size range have the same composition, similar to sectional schemes,

3. *class-resolved*: divide the particles into three classes or modes, defined based on their source, assuming particles within a given class are fully mixed,

4. *size-and-BC-resolved*: assume particles within a bin have the same composition, where the particle population is binned by size and the volume fraction of BC contained in each particle, representing a two-dimensional sectional scheme.

The fully-mixed, size-resolved, and class-resolved representations of composition are illustrated in Figure 8.5, which shows the size distribution and pie charts of composition produced by averaging across an example particle-resolved population in different ways. In the class-resolved representation, we defined three modes based on particle source: 1) combustion particles that had not coagulated with background particles, 2) background particles that had not coagulated with background particles, and 3) particles formed by coagulation between combustion and background particles. The size- and BC-resolved representation requires more composition information than is easily shown visually; this two-dimensional sectional representation is constructed by binning particles within each size bin in the univariate sectional scheme (Figure 8.5.b) according to the volume fraction of BC contained each particle. Because each graph is derived from the same population, the overall size distribution and the bulk mass concentration of each species are the same for all representations of the mixing state, and the populations differ only in the distribution of aerosol components between individual particles.

The normalized mean factor bias (150) in CCN concentration and in the aerosol absorption coefficient for these different representations are shown in Figure 8.6.a and Figure 8.6.b, respectively, summarizing differences between fresh (yellow) and aged (blue) populations across 100 particle-resolved simulations. The error bars in Figure 8.6 show the 95% confidence bias intervals in the relative bias for each case, indicating the range in error found across the simulations.

At the start of the simulations ($t = 0$), representing populations of externally mixed combustion emissions and hygroscopic background particles, the fully-mixed and size-resolved representations of composition led to a mean overestimation in CCN concentrations by 55% and 40%, respectively, as indicated by the yellow dots in Figure 8.6.a. Only the modal representation of composition and the multivariate sectional scheme are able to capture differences in particle hygroscopic properties, which is important for populations containing fresh

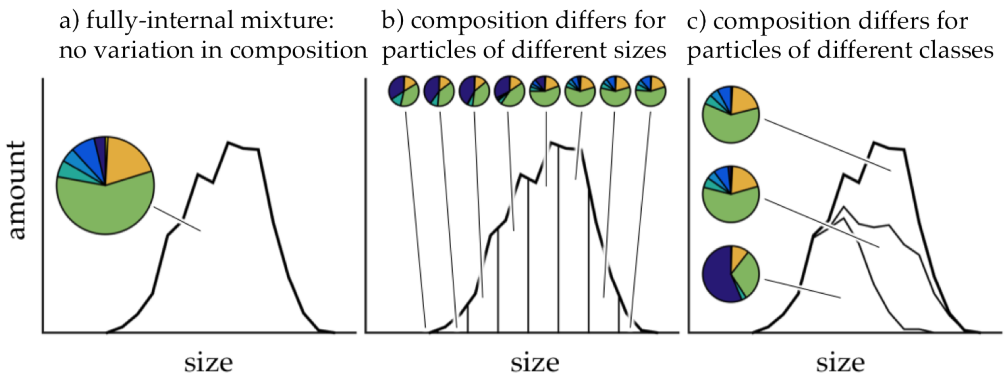

Figure 8.5: Model representations of aerosol composition. For the same distribution in aerosol size, we compare the particle-resolved representation of composition with three simplified representations: (a) assuming uniform composition across all particles, (b) assuming uniform composition for particles within a size bin, and (c) assuming uniform composition for particles of the same type.

emissions. CCN concentrations for populations that have aged for longer times than τ_{mix} can be accurately calculated by any of the representations of aerosol composition investigated here.

8.7 Implications

Many chemical transport models are moving toward the inclusion of aerosol schemes that simulate the evolution of the aerosol mixing state, but the extent to which mixing state needs to be tracked for accurate prediction of climate-relevant aerosol properties has not been quantified. Although aerosol populations are comprised of complex particles of varied chemical composition (120; 95; 81; 53), previous studies have demonstrated that, in some cases, particle-level variation in composition does not strongly affect CCN activity of aerosol populations and, instead, particles can be modeled as full internal mixture (39; 42). The present study puts these observations into context by quantifying the timescale for this full internal mixture approximation to become valid. We show that, in many locations, the fully-mixed approximation becomes valid for modeling CCN activity within hours after particles are emitted. The rate of this transformation can be predicted using a first-order aging timescale τ_{mix}, which depends on quantities that are easily extracted from global models and ambient measurements.

A more detailed representation of the aerosol mixing state is needed to model aerosol optical properties or the hygroscopic properties of populations containing freshly emitted particles. We found that populations containing fresh emissions can be modeled with greater accuracy if schemes resolve differences between aerosol types, which is possible in modal models. Size-resolved and bulk schemes that assume fully-mixed populations artificially distribute the BC mass between the entire population, yielding overestimation in

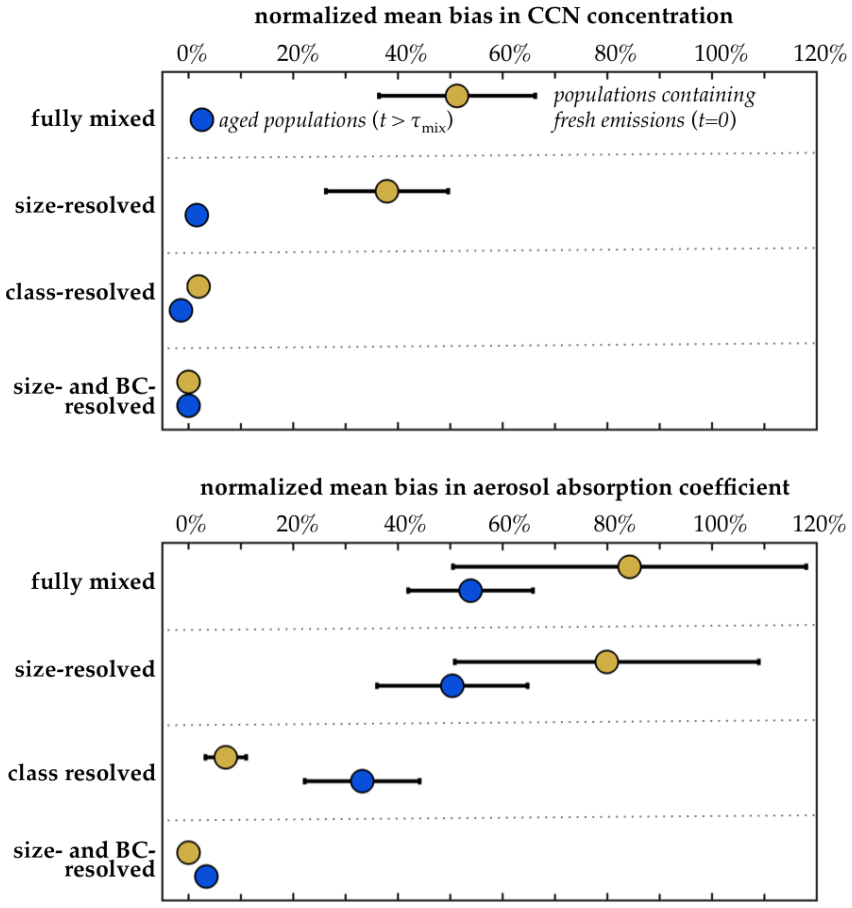

Figure 8.6: Normalized mean factor bias in (a) CCN concentration and (b) aerosol absorption coefficient for populations containing fresh emission (blue) and for populations in which all particles have aged (yellow). Error bars show 95% confidence intervals about the mean error in each case.

modeled absorption and in CCN activation by fresh particles. On the other hand, modal schemes are able to track separate populations for BC-containing particles and, thereby resolve differences in particle optical properties and hygroscopic properties. This advantage would also apply to sectional schemes that resolve separate aerosol distributions, such the global aerosol scheme described in Jacobson (60). It should also be noted that aerosol schemes simplify the representation of the aerosol size distribution, where modal models, in particular, assume the shape size distribution for each mode, but the findings presented here apply only to model representations of composition.

Chapter 9

Conclusions

This dissertation describes multiple studies that fall under the broad goal of improving model representations of atmospheric aerosols, particularly black carbon. The objective of this research is (1) to improve the scientific understanding of the underlying factors that drive aerosol aging, (2) to quantify error in climate-relevant aerosol properties from approximating the representation of aerosol composition, and (3) to produce parameterizations that enable improved representations of black carbon within existing global model frameworks. The specific objectives of each study are outlined in Chapter 2.

9.1 Factors that drive aerosol aging

9.1.1 Summary of key findings

In Chapter 4, I evaluated the importance of particles' emission size distribution and composition in predicting their cloud condensation nuclei (CCN) activation properties as they undergo aging by condensation and coagulation in the atmosphere. I show that particle characteristics at emission affect their removal and their influence on CCN concentrations only under specific conditions. At low supersaturation levels ($s < 0.2\%$), the primary particles yielded little increase in CCN, regardless of aging conditions. At $s > 0.2\%$, total CCN was sensitive to particles' characteristics at emission and the relative importance of particles' initial size versus composition depended on the aging mechanisms at work. Under conditions of rapid condensation of semi-volatile substances, CCN concentrations were more sensitive to particles' initial size than particles' initial composition. On the other hand, in the absence of condensation, primary aerosol emissions did not increase CCN concentrations at any supersaturation below $s = 1\%$.

The first study demonstrated the importance of aging conditions of particle's eventual CCN activation properties, considering only a few aging regimes. Chapter 5 provides a comprehensive analysis of the factors that influence changes in aerosol CCN activation. From the particle-resolved model data, I extracted a timescale for BC aging based which quantifies the rate at which BC-containing particles transition from CCN-inactive to CCN-active at a specific supersaturation level s. I performed a regression analysis to identify

the set of independent variables that most affect the value of this aging timescale. I showed that most of the variance in BC's aging timescale is explained by only a few independent variables. At all supersaturation levels between $s = 0.1\%$ and $s = 1\%$, 90% of variance in timescale for aging by coagulation are explained by two independent variables: 1) the size distribution of BC-containing particles and 2) the overall number concentration of particles that are both CCN-active and large enough to be good coagulation sinks for small BC-containing particles ($D > 200$ nm). Three variables were required to explain 80% of variance in the condensation aging timescale: 1) the size distribution of BC-containing particles, 2) the volume condensation rate of secondary aerosol per particle surface area, and 3) the hygroscopicity parameter of the secondary aerosol.

9.1.2 Implications

In addition to the scientific findings, one contribution of the analysis described in Chapter 5 is a framework for applying nonparametric regression analysis to identify parameters that most affect processes simulated by the particle-resolved model PartMC-MOSAIC. Previously, PartMC-MOSAIC had been used to analyze the aerosol evolution in specific urban scenarios. By applying regression to model data across hundreds of time steps in hundreds of scenarios, I was able to develop general relationships that describe aerosol aging processes and identify governing parameters.

9.1.3 Recommendations for future work

The set of independent variables that most affect black carbon aging rates can be used to develop reduced models, as demonstrated in Chapter 8. However, the parameterization described in Chapter 8 is framed in a particular way, to describe the timescale for freshly emitted particles to become internally mixed with per-existing particles, but these independent variables could also be used to develop parameterizations that describe the aerosol evolution in terms of, for example, changes in CCN activation or changes in aerosol absorption.

The conclusion that the variables identified in Chapter 5 are the minimal set of parameters needed to explain the rate at which particles transition from CCN-inactive to CCN-active requires confirmation using field observations. It may be possible to use observational data to approximate the rate at which particles transition from CCN-inactive to CCN-active under specific conditions, but in many cases these transition rates are not easily predicted because the evolution of the number concentration of CCN is also affected by particle emissions, dilution, and advection. While the effects of individual processes may be distinguished in the particle-resolved model simulations, field observations are able to detect only the cumulative effects of

all processes affecting CCN concentrations. However, it may be possible to validate the key findings using chamber studies. For example, the Aerosol Dynamics and Interactions in the Atmosphere (AIDA) chamber measures the evolution of aerosol populations for extended periods of time, on the order of days, whereas particles remain in most chambers for at most a few hours. Using the temporal evolution of the number concentration of CCN, an aging timescale could be extracted using the approach described in Chapter 5. The nonparametric relationship for this aging timescale could be validated if the temporal evolution of condensational growth rates and particle size distributions are also tracked within the chamber.

9.2 Error in climate-relevant properties from approximate representations of particle characteristics

9.2.1 Summary of key findings

While Chapters 4 and 5 showed that particle size, rather than composition, was most important in predicting the CCN activity of aged particles, in Chapter 6 I show that absorption by populations of BC-containing particles depends strongly on the representation of particle composition. If BC-containing particles are assumed to have uniform composition, neglecting any variation between particles, I find global absorption by BC is overestimated by 30%. Although I find that particle-level variation in composition must be accounted for to estimate BC's absorption, through a regression analysis, I show that enhancement in light absorption by BC due to non-absorbing coatings can be modeled with high accuracy using variables that models already track: 1) the volume fraction of coating mixed with BC-containing particles, 2) the hygroscopicity of the coating, and 3) the environmental relative humidity.

In Chapter 8, I quantify the error in a number of model representations of aerosol composition to assess how more detail in the representation of aerosol composition affects CCN concentrations and aerosol absorption. Based on detailed particle-resolved simulations we derive a characteristic timescale of aging after which CCN concentration can be accurately estimated using only the average composition of the aerosol population. To accurately calculate optical properties, in contrast, more detailed information of particle-level aerosol composition is needed, even for highly aged particle populations.

9.2.2 Implications

Chapters 6 and 8 describe an approach for evaluating model representations of the state of aerosol populations. In the last twenty years, many aerosol schemes have been developed to simulate the evolution of

aerosol size and composition (e.g. 145; 56; 11; 9), and the amount of composition detail tracked has tended to increase over time (e.g. 60; 102; 87). However, it has not been demonstrated that the representation of aerosol composition applied in these models is sufficient, or how resolving additional details impacts estimation of model results. Rather than comparing model predictions using an approximate representation of aerosol composition with a model that applies a different, but also approximate, representation of aerosol composition, Chapters 8 provides a framework for quantifying errors from numerical representations of the aerosol mixing state a benchmark model that fully resolves the aerosol mixing state.

While the research described in Chapters 6 and 8 focuses on quantifying error in, and improving, existing aerosol frameworks, this analysis is also a necessary step in the development of reduced models of the aerosol mixing state. The findings of this research demonstrate the limitations of traditional univariate aerosol schemes, which track only variation in particle size within populations. This research also shows that models need not resolve the full distribution in aerosol components within individual particles, as simulated by PartMC-MOSAIC, to adequately estimate CCN activation and aerosol optical properties. In this way, the analysis provides guidance on the type of composition information that should be resolved in the next generation of aerosol microphysical schemes.

9.2.3 Recommendations for future work

Chapters 6 and 8 evaluated model representations of the aerosol state, but these studies did not consider differences in the model representations of aerosol processes. A comprehensive analysis of error from approximating the aerosol mixing state would compare aerosol populations simulated using different aerosol microphysical schemes but within the same chemical transport model, similar to the methodology described in Fast et al. (43). Additionally, a complete evaluation of model representations of aerosol properties would also evaluate approximations of the aerosol size distribution and of particles' internal morphology. Comparison between model representations of aerosol size would require simulating the evolution of the aerosol size distribution under each model framework because the aerosol processes that affect the evolution of the size distribution depend strongly on the model representation of the size distribution itself (158).

While the results of Chapters 6 and 8 are generally consistent with previous observations, the conclusions of these study need to be rigorously validated. For example, Chapter 6 shows that diversity in the amount of coating between individual particles leads to lower estimates of black carbon absorption than if particles are assumed to have identical composition. Absorption by diverse populations could be modeled using field observations of particle-level composition, such as those provide by the Single Particle Soot Photometer (130; 125). Based on the findings in Chapter 6, a collection of diverse particles would be expected to have

lower modeled absorption than if the particles in that population were assumed to be identical in composition. This could be tested by applying a similar analysis to the observations of per-particle composition as I applied to the modeled particles simulated by PartMC-MOSAIC (Chapter 6). The predictions of absorption enhancement by the diverse and uniform BC populations could be compared with observations of absorption enhancement, similar to the approach described in Cappa et al. (21).

9.3 Parameterizations to improve aerosol representations in chemical transport models

9.3.1 Summary of key findings

The final research objective, to produce parameterizations that enable improved representations of black carbon carbon within existing global model frameworks, was accomplished in the studies described Chapters 7 and 8. Chapter 8 describes a timescale for emitted particles to become internally mixed with background, using variables easily extracted from bulk aerosol models. This parameterization introduces a new framework for quantifying aerosol aging and can be implemented in bulk aerosol schemes.

In Chapter 7, I build on the work of Chapter 6 and provide a parametric relationship that estimates BC's absorption coefficient as a function of variables tracked by modal aerosol models. In addition to depending on the volume fraction of dry coating, the coating hygroscopicity, and the environmental relativity, as was found in Chapter 6, the full parameterization also depends on the mass concentration of BC and the wavelength of light. Chapter 6 focused on absorption enhancement at only a single wavelength, whereas Chapter 7 provides a parameterization for the absorption coefficient that has been verified for wavelengths between 350 nm to 850 nm. The parametric relationship reproduces the particle-resolved model results with high accuracy ($R^2 = 99\%$).

9.3.2 Implications

The parametric relationships described in Chapters 7 and 8 are the first parametric expressions that have been developed from a particle-resolved aerosol model. These studies introduce a new procedure for developing reduced aerosol representations from particle-resolved simulations. The parametric relationships described in this dissertation were developed as a way to represent processes that cannot be captured in certain simplified aerosol representations. Therefore, applying these parameterizations to model data should improve aerosol representations in bulk and modal models, but the parameterizations must first be validated

against observations.

9.3.3 Recommendations for future work

An important next step is to validate the proposed parameterizations against field observations. The parameterization described in Chapter 7 that estimates the absorption coefficient of BC populations should be validated using measurements of the bulk composition of BC populations and measurements of BC's absorption coefficient, which indicates absorption per BC mass. Bulk composition of BC-containing particles can be measured using the Soot Particle Aerosol Mass Spectrometer (100), which measures the mass and chemical composition of coatings and the mass of BC contained in populations of BC-containing particles. The absorption coefficient as a function of wavelength can be measured using the Particle Soot Absorption Photometer (14).

Validation of the mixing timescale τ_{mix} is more difficult because, rather than requiring measurements of the aerosol state at a particular time and location, validation against *in situ* observations would require knowledge of the aging history of the aerosol population that led to the observed aerosol state. Instead, I would suggest implementing the parameterization in a regional-scale chemical transport model, such as the Weather Research and Forecasting model with Chemistry (48), to identify in which locations CCN activity can be accurately estimated if particles are assumed to be fully mixed, and in which locations differences in composition must be resolved to model CCN activity. The predicted error in various locations can be validated against field observations using CCN closure studies, as described in, for example, Ervens et al. (42).

After these parameterizations have been validated against observations, the next step is to implement each relationship into chemical transport models. The parametric relationship for black carbon's aging timescale that is described in Chapter 8 was designed for mass-based aerosol models, such as the ModelE2 version of the Goddard Institute for Space Studies General Circulation Model (118) run with a bulk aerosol scheme. Although this parametric relationship was designed for used in bulk models, it may also provide a physically-relevant rate for transitions between modes in modal aerosol models. The expression for black carbon's absorption coefficient that is described in Chapter 6 should be implemented into a modal aerosol scheme, such as the Goddard Institute for Space Studies ModelE run with the modal aerosol scheme MATRIX (9). Additionally, this expression for BC's absorption coefficient may be useful for mass-based aerosol models if certain assumptions are applied about the amount and hygroscopicity of aerosol that is mixed with BC-containing particles.

Finally, while this dissertation describes one line of approaches to improve aerosol representations within

existing aerosol model frameworks, focusing on the development of simple parameterizations from detailed model simulations. However, rather than parameterizing key processes, the findings in this dissertation could also be used to develop aerosol schemes that resolve sufficient information about the particle population to adequately represent climate-relevant properties and dominant aerosol processes. I plan to build upon this dissertation research in the future through the development of a multivariate moment-based aerosol scheme, which tracks variation in the particle characteristics that I have found, through my doctoral research, need to be resolved for adequate representation of climate-relevant aerosol properties: 1) particle size, 2) particle hygroscopicity parameter, and 3) the volume fraction of absorbing aerosol, such as BC or mineral dust, contained in each particle. In this way, in addition to evaluating current model representations and providing simple parameterizations to improve them, my doctoral research will guide the development of a new model for simulating the evolution of atmospheric aerosols.

References

[1] Ackerman, A. S., Toon, O., Stevens, D., Heymsfield, A., Ramanathan, V., and Welton, E. (2000). Reduction of tropical cloudiness by soot. *Science*, 288(5468):1042–1047.

[2] Adachi, K., Chung, S. H., and Buseck, P. R. (2010). Shapes of soot aerosol particles and implications for their effects on climate. *Journal of Geophysical Research*, 115(D15).

[3] Albrecht, B. (1989). Aerosols, cloud microphysics, and fractional cloudiness. *Science*, 245(4923):1227–1230.

[4] Andreae, M. and Rosenfeld, D. (2008). Aerosol–cloud–precipitation interactions. Part 1. The nature and sources of cloud-active aerosols. *Earth-Science Reviews*, 89(1):13–41.

[5] Aquila, V., Hendricks, J., Lauer, A., Riemer, N., Vogel, H., Baumgardner, D., Minikin, A., Petzold, A., Schwarz, J., Spackman, J., et al. (2011). Made-in: a new aerosol microphysics submodel for global simulation of insoluble particles and their mixing state. *Geoscientific Model Development*, 4(2):325–355.

[6] Archer, D. (2005). Fate of fossil fuel co2 in geologic time. *Journal of Geophysical Research: Oceans (1978–2012)*, 110(C9).

[7] Archer, D., Eby, M., Brovkin, V., Ridgwell, A., Cao, L., Mikolajewicz, U., Caldeira, K., Matsumoto, K., Munhoven, G., Montenegro, A., et al. (2009). Atmospheric lifetime of fossil fuel carbon dioxide. *Annual Review of Earth and Planetary Sciences*, 37(1):117.

[8] Bauer, S., Menon, S., Koch, D., Bond, T., and Tsigaridis, K. (2010). A global modeling study on carbonaceous aerosol microphysical characteristics and radiative effects. *Atmospheric Chemistry and Physics*, 10(15):7439–7456.

[9] Bauer, S., Wright, D., Koch, D., Lewis, E., McGraw, R., Chang, L., Schwartz, S., and Ruedy, R. (2008). MATRIX (multiconfiguration Aerosol TRacker of mIXing state): an aerosol microphysical module for global atmospheric models. *Atmospheric Chemistry and Physics*, 8(20):6003–6035.

[10] Bauer, S. E. and Menon, S. (2012). Aerosol direct, indirect, semidirect, and surface albedo effects from sector contributions based on the ipcc ar5 emissions for preindustrial and present-day conditions. *Journal of Geophysical Research: Atmospheres (1984–2012)*, 117(D1).

[11] Binkowski, F. and Roselle, S. (2003). Models-3 community multiscale air quality (CMAQ) model aerosol component: 1. Model description. *Journal of Geophysical Research*, 108(4183):15.

[12] Boer, G. and Yu, B. (2003). Climate sensitivity and response. *Climate Dynamics*, 20(4):415–429.

[13] Bohren, C. F. and Huffman, D. R. (1983). Absorption and scattering by a sphere. *Absorption and Scattering of Light by Small Particles*.

[14] Bond, T. C., Anderson, T. L., and Campbell, D. (1999). Calibration and intercomparison of filter-based measurements of visible light absorption by aerosols. *Aerosol Science & Technology*, 30(6):582–600.

[15] Bond, T. C., Doherty, S. J., Fahey, D., Forster, P., Berntsen, T., DeAngelo, B., Flanner, M., Ghan, S., Kärcher, B., Koch, D., et al. (2013). Bounding the role of black carbon in the climate system: A scientific assessment. *Journal of Geophysical Research: Atmospheres*, 118(11):5380–5552.

[16] Bond, T. C., Habib, G., and Bergstrom, R. W. (2006). Limitations in the enhancement of visible light absorption due to mixing state. *Journal of Geophysical Research: Atmospheres (1984–2012)*, 111(D20).

[17] Boucher, O., Randall, D., Artaxo, P., Bretherton, C., Feingold, G., Forster, P., Kerminen, V.-M., Kondo, Y., Liao, H., Lohmann, U., et al. (2013). Clouds and aerosols. In *Climate change 2013: the physical science basis. Contribution of Working Group I to the Fifth Assessment Report of the Intergovernmental Panel on Climate Change*, pages 571–657. Cambridge University Press.

[18] Browse, J., Carslaw, K., Arnold, S., Pringle, K., and Boucher, O. (2012). The scavenging processes controlling the seasonal cycle in arctic sulphate and black carbon aerosol. *Atmos. Chem. Phys*, 12:6775–6798.

[19] Cantrell, W., Shaw, G., Cass, G. R., Chowdhury, Z., Hughes, L. S., Prather, K. A., Guazzotti, S. A., and Coffee, K. R. (2001). Closure between aerosol particles and cloud condensation nuclei at kaashidhoo climate observatory. *Journal of Geophysical Research: Atmospheres (1984–2012)*, 106(D22):28711–28718.

[20] Cape, J., Coyle, M., and Dumitrean, P. (2012). The atmospheric lifetime of black carbon. *Atmospheric Environment*, 59:256–263.

[21] Cappa, C. D., Onasch, T. B., Massoli, P., Worsnop, D. R., Bates, T. S., Cross, E. S., Davidovits, P., Hakala, J., Hayden, K. L., Jobson, B. T., et al. (2012). Radiative absorption enhancements due to the mixing state of atmospheric black carbon. *Science*, 337(6098):1078–1081.

[22] Chang, L., Schwartz, S., McGraw, R., and Lewis, E. (2009). Sensitivity of aerosol properties to new particle formation mechanism and to primary emissions in a continental-scale chemical transport model. *Journal of Geophysical Research*, 114:D07203.

[23] Chen, W., Lee, Y., Adams, P., Nenes, A., Seinfeld, J., et al. (2010). Will black carbon mitigation dampen aerosol indirect forcing? *Geophysical Research Letters*, 37(9):L09801.

[24] Cheng, Y., Su, H., Rose, D., Gunthe, S., Berghof, M., Wehner, B., Achtert, P., Nowak, A., Takegawa, N., Kondo, Y., et al. (2012). Size-resolved measurement of the mixing state of soot in the megacity beijing, china: diurnal cycle, aging and parameterization. *Atmospheric Chemistry and Physics*, 12(10):4477–4491.

[25] Chin, M., Diehl, T., Tan, Q., Prospero, J., Kahn, R., Remer, L., Yu, H., Sayer, A., Bian, H., Geogdzhayev, I., et al. (2014). Multi-decadal aerosol variations from 1980 to 2009: a perspective from observations and a global model. *Atmospheric Chemistry and Physics*, 14(7):3657–3690.

[26] China, S., Mazzoleni, C., Gorkowski, K., Aiken, A. C., and Dubey, M. K. (2013). Morphology and mixing state of individual freshly emitted wildfire carbonaceous particles. *Nature communications*, 4.

[27] Chung, C. E., Lee, K., and Müller, D. (2011). Effect of internal mixture on black carbon radiative forcing. *Tellus B*, 64.

[28] Chung, S. H. and Seinfeld, J. H. (2002). Global distribution and climate forcing of carbonaceous aerosols. *Journal of Geophysical Research: Atmospheres (1984–2012)*, 107(D19):AAC–14.

[29] Chung, S. H. and Seinfeld, J. H. (2005). Climate response of direct radiative forcing of anthropogenic black carbon. *Journal of Geophysical Research: Atmospheres (1984–2012)*, 110(D11).

[30] Church, J. A. and White, N. J. (2011). Sea-level rise from the late 19th to the early 21st century. *Surveys in Geophysics*, 32(4-5):585–602.

[31] Chylek, P., Ramaswamy, V., and Cheng, R. J. (1984). Effect of graphitic carbon on the albedo of clouds. *Journal of the Atmospheric Sciences*, 41(21):3076–3084.

[32] Clegg, S., Brimblecombe, P., and Wexler, A. (1998). Thermodynamic model of the system H^+-NH_4^+-SO_4^{2-}-NO_3^--H_2O at tropospheric temperatures. *The Journal of Physical Chemistry A*, 102(12):2137–2154.

[33] Cooke, W., Liousse, C., Cachier, H., and Feichter, J. (1999). Construction of a 1× 1 fossil fuel emission data set for carbonaceous aerosol and implementation and radiative impact in the echam4 model. *Journal of Geophysical Research*, 104(D18):22137–22.

[34] Cooke, W. and Wilson, J. (1996). A global black carbon aerosol model. *Journal of Geophysical Research*, 101(D14):19395–19.

[35] Cozic, J., Verheggen, B., Mertes, S., Connolly, P., Bower, K., Petzold, A., Baltensperger, U., and Weingartner, E. (2007). Scavenging of black carbon in mixed phase clouds at the high alpine site jungfraujoch. *Atmospheric Chemistry and Physics*, 7(7):1797–1807.

[36] Croft, B., Lohmann, U., Von Salzen, K., et al. (2005). Black carbon ageing in the canadian centre for climate modelling and analysis atmospheric general circulation model. *Atmos. Chem. Phys*, 5(7):1931–1949.

[37] Cross, E. S., Onasch, T. B., Ahern, A., Wrobel, W., Slowik, J. G., Olfert, J., Lack, D. A., Massoli, P., Cappa, C. D., Schwarz, J. P., et al. (2010). Soot particle studiesinstrument inter-comparisonproject overview. *Aerosol Science and Technology*, 44(8):592–611.

[38] Cubison, M., Ervens, B., Feingold, G., Docherty, K., Ulbrich, I., Shields, L., Prather, K., Hering, S., and Jimenez, J. (2008). The influence of chemical composition and mixing state of los angeles urban aerosol on ccn number and cloud properties. *Atmospheric Chemistry and Physics*, 8(18):5649–5667.

[39] Dusek, U., Frank, G., Hildebrandt, L., Curtius, J., Schneider, J., Walter, S., Chand, D., Drewnick, F., Hings, S., Jung, D., et al. (2006). Size matters more than chemistry for cloud-nucleating ability of aerosol particles. *Science*, 312(5778):1375–1378.

[40] Eldering, A. and Cass, G. (1996). Source-oriented model for air pollutant effects on visibility. *Journal of Geophysical Research*, 101(D14):19343–19.

[41] Engelhart, G., Hennigan, C., Miracolo, M., Robinson, A., and Pandis, S. (2012). Cloud condensation nuclei activity of fresh primary and aged biomass burning aerosol. *Atmospheric Chemistry and Physics*, 12:7285–7293.

[42] Ervens, B., Cubison, M., Andrews, E., Feingold, G., Ogren, J., Jimenez, J., Quinn, P., Bates, T., Wang, J., Zhang, Q., et al. (2010). CCN predictions using simplified assumptions of organic aerosol composition and mixing state: a synthesis from six different locations. *Atmospheric Chemistry and Physics*, 10:4795–4807.

[43] Fast, J. D., Gustafson Jr, W. I., Chapman, E. G., Easter, R. C., Rishel, J. P., Zaveri, R. A., Grell, G. A., and Barth, M. C. (2011). The aerosol modeling testbed: A community tool to objectively evaluate aerosol process modules. *Bulletin of the American Meteorological Society*, 92(3):343–360.

[44] Fierce, L., Riemer, N., and Bond, T. (2015). Explaining variance in black carbon's aging timescale. *Atmospheric Chemistry and Physics*, 15(6):3173–3191.

[45] Fierce, L., Riemer, N., and Bond, T. C. (2013). When is cloud condensation nuclei activity sensitive to particle characteristics at emission? *Journal of Geophysical Research: Atmospheres*, 118(24):13–476.

[46] Furutani, H., Dallosto, M., Roberts, G., and Prather, K. (2008). Assessment of the relative importance of atmospheric aging on CCN activity derived from field observations. *Atmospheric Environment*, 42(13):3130–3142.

[47] Gieré, R. and Querol, X. (2010). Solid particulate matter in the atmosphere. *Elements*, 6(4):215–222.

[48] Grell, G. A., Peckham, S. E., Schmitz, R., McKeen, S. A., Frost, G., Skamarock, W. C., and Eder, B. (2005). Fully coupled online chemistry within the wrf model. *Atmospheric Environment*, 39(37):6957–6975.

[49] Hansen, J. and Nazarenko, L. (2004). Soot climate forcing via snow and ice albedos. *Proceedings of the National Academy of Sciences of the United States of America*, 101(2):423–428.

[50] Hansen, J., Ruedy, R., Sato, M., and Lo, K. (2010). Global surface temperature change. *Reviews of Geophysics*, 48(4).

[51] Hansen, J. and Sato, M. (2001). Trends of measured climate forcing agents. *Proceedings of the National Academy of Sciences*, 98(26):14778.

[52] Haywood, J., Roberts, D., Slingo, A., Edwards, J., and Shine, K. (1997). General circulation model calculations of the direct radiative forcing by anthropogenic sulfate and fossil-fuel soot aerosol. *Journal of Climate*, 10(7):1562–1577.

[53] Healy, R., Riemer, N., Wenger, J., Murphy, M., West, M., Poulain, L., Wiedensohler, A., O'Connor, I., McGillicuddy, E., Sodeau, J., et al. (2014). Single particle diversity and mixing state measurements. *Atmospheric Chemistry and Physics Discussions*, 14(3):3973–4005.

[54] Healy, R., Sciare, J., Poulain, L., Kamili, K., Merkel, M., Müller, T., Wiedensohler, A., Eckhardt, S., Stohl, A., Sarda-Estève, R., et al. (2012). Sources and mixing state of size-resolved elemental carbon particles in a european megacity: Paris. *Atmospheric Chemistry and Physics*, 12(4):1681–1700.

[55] Hitzenberger, R., Berner, A., Giebl, H., Drobesch, K., Kasper-Giebl, A., Loeflund, M., Urban, H., and Puxbaum, H. (2001). Black carbon (BC) in alpine aerosols and cloud water–concentrations and scavenging efficiencies. *Atmospheric Environment*, 35(30):5135–5141.

[56] Jacobson, M. (1997). Development and application of a new air pollution modeling system–II. Aerosol module structure and design. *Atmospheric Environment*, 31(2):131–144.

[57] Jacobson, M. (2010). Short-term effects of controlling fossil-fuel soot, biofuel soot and gases, and methane on climate, arctic ice, and air pollution health. *Journal of Geophysical Research*, 115(D14):D14209.

[58] Jacobson, M. Z. (2000). A physically-based treatment of elemental carbon optics: Implications for global direct forcing of aerosols. *Geophysical Research Letters*, 27(2):217–220.

[59] Jacobson, M. Z. (2001). Strong radiative heating due to the mixing state of black carbon in atmospheric aerosols. *Nature*, 409(6821):695–697.

[60] Jacobson, M. Z. (2002). Analysis of aerosol interactions with numerical techniques for solving coagulation, nucleation, condensation, dissolution, and reversible chemistry among multiple size distributions. *Journal of Geophysical Research: Atmospheres (1984–2012)*, 107(D19):AAC–2.

[61] Jacobson, M. Z. (2004). Climate response of fossil fuel and biofuel soot, accounting for soot's feedback to snow and sea ice albedo and emissivity. *Journal of Geophysical Research*, 109(D21).

[62] Jacobson, M. Z. (2005). Correction to control of fossil-fuel particulate black carbon and organic matter, possibly the most effective method of slowing global warming. *Journal of Geophysical Research*, 110(D14).

[63] Jacobson, M. Z. (2006). Effects of externally-through-internally-mixed soot inclusions within clouds and precipitation on global climate. *The Journal of Physical Chemistry A*, 110(21):6860–6873.

[64] Jacobson, M. Z. (2012). Investigating cloud absorption effects: Global absorption properties of black carbon, tar balls, and soil dust in clouds and aerosols. *Journal of Geophysical Research: Atmospheres (1984–2012)*, 117(D6).

[65] Jimenez, J., Canagaratna, M., Donahue, N., Prevot, A., Zhang, Q., Kroll, J., DeCarlo, P., Allan, J., Coe, H., Ng, N., et al. (2009). Evolution of organic aerosols in the atmosphere. *Science*, 326(5959):1525–1529.

[66] Jo, D., Park, R., Kim, M., and Spracklen, D. (2013). Effects of chemical aging on global secondary organic aerosol using the volatility basis set approach. *Atmospheric Environment*, 81:230–244.

[67] Johnson, K. S., Zuberi, B., Molina, L., Molina, M. J., Iedema, M. J., Cowin, J. P., Gaspar, D. J., Wang, C., and Laskin, A. (2005). Processing of soot in an urban environment: case study from the mexico city metropolitan area. *Atmospheric Chemistry and Physics*, 5(11):3033–3043.

[68] Jones, P., Lister, D., Osborn, T., Harpham, C., Salmon, M., and Morice, C. (2012). Hemispheric and large-scale land-surface air temperature variations: An extensive revision and an update to 2010. *Journal of Geophysical Research*, 117(D5).

[69] Kennedy, J., Rayner, N., Smith, R., Parker, D., and Saunby, M. (2011). Reassessing biases and other uncertainties in sea surface temperature observations measured in situ since 1850: 1. measurement and sampling uncertainties. *Journal of Geophysical Research*, 116(D14).

[70] Khalizov, A., Zhang, R., Zhang, D., Xue, H., Pagels, J., and McMurry, P. (2009). Formation of highly hygroscopic soot aerosols upon internal mixing with sulfuric acid vapor. *Journal of Geophysical Research*, 114:D05208.

[71] Kim, D. and Ramanathan, V. (2008). Solar radiation budget and radiative forcing due to aerosols and clouds. *Journal of Geophysical Research*, 113:D02203.

[72] Kittelson, D., Watts, W., and Johnson, J. (2006a). On-road and laboratory evaluation of combustion aerosols–Part 1: Summary of diesel engine results. *Journal of Aerosol Science*, 37(8):913–930.

[73] Kittelson, D., Watts, W., Johnson, J., Schauer, J., and Lawson, D. (2006b). On-road and laboratory evaluation of combustion aerosols–Part 2: Summary of spark ignition engine results. *Journal of Aerosol Science*, 37(8):931–949.

[74] Koch, D. (2001). Transport and direct radiative forcing of carbonaceous and sulfate aerosols in the giss gcm. *Journal of Geophysical Research*, 106(D17):20311–20332.

[75] Koch, D., Balkanski, Y., Bauer, S., Easter, R., Ferrachat, S., Ghan, S., Hoose, C., Iversen, T., Kirkevåg, A., Kristjansson, J., et al. (2011). Soot microphysical effects on liquid clouds, a multi-model investigation. *Atmospheric Chemistry and Physics*, 11(3):1051–1064.

[76] Koch, D., Schulz, M., Kinne, S., McNaughton, C., Spackman, J., Balkanski, Y., Bauer, S., Berntsen, T., Bond, T. C., Boucher, O., et al. (2009). Evaluation of black carbon estimations in global aerosol models. *Atmospheric Chemistry and Physics*, 9(22):9001–9026.

[77] Köhler, H. (1936). The nucleus in and the growth of hygroscopic droplets. *Transactions of the Faraday Society*, 32:1152–1161.

[78] Krieger, U. K., Marcolli, C., and Reid, J. P. (2012). Exploring the complexity of aerosol particle properties and processes using single particle techniques. *Chemical Society Reviews*, 41(19):6631–6662.

[79] Kulmala, M., Vehkamäki, H., Petäjä, T., Dal Maso, M., Lauri, A., Kerminen, V.-M., Birmili, W., and McMurry, P. H. (2004). Formation and growth rates of ultrafine atmospheric particles: a review of observations. *Journal of Aerosol Science*, 35(2):143–176.

[80] Levitus, S., Antonov, J., Boyer, T., Locarnini, R., Garcia, H., and Mishonov, A. (2009). Global ocean heat content 1955–2008 in light of recently revealed instrumentation problems. *Geophysical Research Letters*, 36(7).

[81] Liu, D., Allan, J., Whitehead, J., Young, D., Flynn, M., Coe, H., McFiggans, G., Fleming, Z., and Bandy, B. (2012). Ambient black carbon particle hygroscopic properties controlled by mixing state and composition. *Atmospheric Chemistry and Physics Discussions*, 12(11):28955–28992.

[82] Liu, J., Fan, S., Horowitz, L. W., and Levy, H. (2011). Evaluation of factors controlling long-range transport of black carbon to the arctic. *Journal of Geophysical Research: Atmospheres (1984–2012)*, 116(D4).

[83] Lloyd, A. and Cackette, T. (2001). Diesel Engines: Environmental Impact and Control. *Journal of the Air and Waste Management Association*, 51(6):809–847.

[84] Lohmann, U. and Feichter, J. (2005). Global indirect aerosol effects: a review. *Atmospheric Chemistry and Physics*, 5(3):715–737.

[85] Maricq, M. M. (2007). Chemical characterization of particulate emissions from diesel engines: A review. *Journal of Aerosol Science*, 38(11):1079–1118.

[86] Martin, M., Chang, R.-W., Sierau, B., Sjogren, S., Swietlicki, E., Abbatt, J., Leck, C., and Lohmann, U. (2011). Cloud condensation nuclei closure study on summer arctic aerosol. *Atmospheric Chemistry and Physics*, 11(22):11335–11350.

[87] Matsui, H., Koike, M., Kondo, Y., Moteki, N., Fast, J. D., and Zaveri, R. A. (2013). Development and validation of a black carbon mixing state resolved three-dimensional model: Aging processes and radiative impact. *Journal of Geophysical Research: Atmospheres*, 118(5):2304–2326.

[88] McGraw, R. (1997). Description of aerosol dynamics by the quadrature method of moments. *Aerosol Science and Technology*, 27(2):255–265.

[89] McGraw, R., Leng, L., Zhu, W., Riemer, N., and West, M. (2008). Aerosol dynamics using the quadrature method of moments: Comparing several quadrature schemes with particle-resolved simulation. In *Journal of Physics: Conference Series*, volume 125, page 012020. IOP Publishing.

[90] McGraw, R. and Wright, D. L. (2003). Chemically resolved aerosol dynamics for internal mixtures by the quadrature method of moments. *Journal of Aerosol Science*, 34(2):189–209.

[91] McGuire, M., Jeong, C.-H., Slowik, J., Chang, R.-W., Corbin, J., Lu, G., Mihele, C., Rehbein, P., Sills, D., Abbatt, J., et al. (2011). Elucidating determinants of aerosol composition through particle-type-based receptor modeling. *Atmospheric Chemistry and Physics*, 11(15):8133–8155.

[92] McKay, M. D., Beckman, R. J., and Conover, W. J. (1979). Comparison of three methods for selecting values of input variables in the analysis of output from a computer code. *Technometrics*, 21(2):239–245.

[93] Menne, M. J., Durre, I., Vose, R. S., Gleason, B. E., and Houston, T. G. (2012). An overview of the global historical climatology network-daily database. *Journal of Atmospheric and Oceanic Technology*, 29(7):897–910.

[94] Mikhailov, E., Vlasenko, S., Podgorny, I., Ramanathan, V., and Corrigan, C. (2006). Optical properties of soot–water drop agglomerates: An experimental study. *Journal of Geophysical Research: Atmospheres (1984–2012)*, 111(D7).

[95] Moffet, R. C., Qin, X., Rebotier, T., Furutani, H., and Prather, K. A. (2008). Chemically segregated optical and microphysical properties of ambient aerosols measured in a single-particle mass spectrometer. *Journal of Geophysical Research: Atmospheres (1984–2012)*, 113(D12).

[96] Myhre, G., Shindell, D., Bréon, F., Collins, W., Fuglestvedt, J., Huang, J., Koch, D., Lamarque, J., Lee, D., Mendoza, B., et al. (2013). Anthropogenic and natural radiative forcing. *Climate change*, 423.

[97] Nadaraya, E. A. (1964). On estimating regression. *Theory of Probability & Its Applications*, 9(1):141–142.

[98] Nasa Earth Observatory Global maps: Aerosol optical depth.

[99] Ogren, J. and Charlson, R. (1983). Elemental carbon in the atmosphere: cycle and lifetime. *Tellus B*, 35(4).

[100] Onasch, T., Trimborn, A., Fortner, E., Jayne, J., Kok, G., Williams, L., Davidovits, P., and Worsnop, D. (2012). Soot particle aerosol mass spectrometer: development, validation, and initial application. *Aerosol Science and Technology*, 46(7):804–817.

[101] Oshima, N. and Koike, M. (2013). Development of a parameterization of black carbon aging for use in general circulation models. *Geoscientific Model Development*, 6(2):263–282.

[102] Oshima, N., Koike, M., Zhang, Y., Kondo, Y., Moteki, N., Takegawa, N., and Miyazaki, Y. (2009). Aging of black carbon in outflow from anthropogenic sources using a mixing state resolved model: Model development and evaluation. *Journal of Geophysical Research*, 114(D6).

[103] Penner, J., Chuang, C., and Grant, K. (1998). Climate forcing by carbonaceous and sulfate aerosols. *Climate Dynamics*, 14(12):839–851.

[104] Petters, M. and Kreidenweis, S. (2007). A single parameter representation of hygroscopic growth and cloud condensation nucleus activity. *Atmospheric Chemistry and Physics*, 7(8):1961–1971.

[105] Petters, M., Prenni, A., Kreidenweis, S., DeMott, P., Matsunaga, A., Lim, Y., and Ziemann, P. (2006). Chemical aging and the hydrophobic-to-hydrophilic conversion of carbonaceous aerosol. *Geophysical research letters*, 33(24):L24806.

[106] Pierce, J. and Adams, P. (2009). Uncertainty in global CCN concentrations from uncertain aerosol nucleation and primary emission rates. *Atmospheric Chemistry and Physics*, 9:1339–1356.

[107] Pierce, J., Theodoritsi, G., Adams, P., and Pandis, S. (2009). Parameterization of the effect of sub-grid scale aerosol dynamics on aerosol number emission rates. *Journal of Aerosol Science*, 40(5):385–393.

[108] Prenni, A., Petters, M., Kreidenweis, S., DeMott, P., and Ziemann, P. (2007). Cloud droplet activation of secondary organic aerosol. *Journal of Geophysical Research*, 112(D10):10223.

[109] Pringle, K., Tost, H., Pozzer, A., Pöschl, U., and Lelieveld, J. (2010). Global distribution of the effective aerosol hygroscopicity parameter for ccn activation. *Atmospheric Chemistry and Physics*, 10(12):5241–5255.

[110] Ramanathan, V. and Carmichael, G. (2008). Global and regional climate changes due to black carbon. *Nature geoscience*, 1(4):221–227.

[111] Ramaswamy, V., Boucher, O., Haigh, J., Hauglustaine, D., Haywood, J., Myhre, G., Nakajima, T., Shi, G., Solomon, S., Betts, R. E., et al. (2001). Radiative forcing of climate change. Technical report, Pacific Northwest National Laboratory (PNNL), Richland, WA (US).

[112] Reddington, C., Carslaw, K., Spracklen, D., Frontoso, M., Collins, L., Merikanto, J., Minikin, A., Hamburger, T., Coe, H., Kulmala, M., et al. (2011). Primary versus secondary contributions to particle number concentrations in the european boundary layer. *Atmospheric Chemistry and Physics*, 11:12007–12036.

[113] Riemer, N., Vogel, H., and Vogel, B. (2004). Soot aging time scales in polluted regions during day and night. *Atmospheric Chemistry and Physics*, 4(7):1885–1893.

[114] Riemer, N., West, M., Zaveri, R., and Easter, R. (2010). Estimating black carbon aging time-scales with a particle-resolved aerosol model. *Journal of Aerosol Science*, 41(1):143–158.

[115] Riemer, N., West, M., Zaveri, R. A., and Easter, R. C. (2009). Simulating the evolution of soot mixing state with a particle-resolved aerosol model. *Journal of Geophysical Research*, 114(D9).

[116] Rose, D., Gunthe, S., Su, H., Garland, R., Yang, H., Berghof, M., Cheng, Y., Wehner, B., Achtert, P., Nowak, A., et al. (2011). Cloud condensation nuclei in polluted air and biomass burning smoke near the mega-city guangzhou, china–part 2: Size-resolved aerosol chemical composition, diurnal cycles, and externally mixed weakly ccn-active soot particles. *Atmospheric Chemistry and Physics*, 11(6):2817–2836.

[117] Rosen, H., Hansen, A., Gundel, L., and Novakov, T. (1978). Identification of the optically absorbing component in urban aerosols. *Applied Optics*, 17(24):3859–3861.

[118] Schmidt, G. A., Kelley, M., Nazarenko, L., Ruedy, R., Russell, G. L., Aleinov, I., Bauer, M., Bauer, S. E., Bhat, M. K., Bleck, R., et al. (2014). Configuration and assessment of the giss modele2 contributions to the cmip5 archive. *Journal of Advances in Modeling Earth Systems*.

[119] Schnaiter, M., Horvath, H., Möhler, O., Naumann, K.-H., Saathoff, H., and Schöck, O. (2003). Uv-vis-nir spectral optical properties of soot and soot-containing aerosols. *Journal of Aerosol Science*, 34(10):1421–1444.

[120] Schwarz, J., Gao, R., Spackman, J., Watts, L., Thomson, D., Fahey, D., Ryerson, T., Peischl, J., Holloway, J., Trainer, M., et al. (2008). Measurement of the mixing state, mass, and optical size of individual black carbon particles in urban and biomass burning emissions. *Geophysical Research Letters*, 35(13).

[121] Seber, G. and Wild, C. (2003). Nonlinear regress.

[122] Sedlacek, A. J., Lewis, E. R., Kleinman, L., Xu, J., and Zhang, Q. (2012). Determination of and evidence for non-core-shell structure of particles containing black carbon using the single-particle soot photometer (SP2). *Geophysical Research Letters*, 39(6).

[123] Seinfeld, J. H. and Pandis, S. N. (1998). *Atmospheric chemistry and physics: from air pollution to climate change*. John Wiley & Sons.

[124] Silverman, B. (1986). *Density estimation for statistics and data analysis*, volume 26. Chapman & Hall/CRC.

[125] Slowik, J. G., Cross, E. S., Han, J.-H., Davidovits, P., Onasch, T. B., Jayne, J. T., Williams, L. R., Canagaratna, M. R., Worsnop, D. R., Chakrabarty, R. K., et al. (2007). An inter-comparison of instruments measuring black carbon content of soot particles. *Aerosol Science and Technology*, 41(3):295–314.

[126] Smith, T. M., Reynolds, R. W., Peterson, T. C., and Lawrimore, J. (2008). Improvements to noaa's historical merged land-ocean surface temperature analysis (1880-2006). *Journal of Climate*, 21(10):2283–2296.

[127] Sodeman, D., Toner, S., and Prather, K. (2005). Determination of single particle mass spectral signatures from light-duty vehicle emissions. *Environmental Science and Technology*, 39(12):4569–4580.

[128] Spracklen, D., Carslaw, K., Pöschl, U., Rap, A., and Forster, P. (2011). Global cloud condensation nuclei influenced by carbonaceous combustion aerosol. *Atmospheric Chemistry and Physics*, 11(17):9067–9087.

[129] Spracklen, D. V., Carslaw, K. S., Merikanto, J., Mann, G. W., Reddington, C. L., Pickering, S., Ogren, J. A., Andrews, E., Baltensperger, U., Weingartner, E., et al. (2010). Explaining global surface aerosol number concentrations in terms of primary emissions and particle formation. *Atmospheric Chemistry and Physics*, 10(10):4775–4793.

[130] Stephens, M., Turner, N., and Sandberg, J. (2003). Particle identification by laser-induced incandescence in a solid-state laser cavity. *Applied optics*, 42(19):3726–3736.

[131] Stier, P., Feichter, J., Kinne, S., Kloster, S., Vignati, E., Wilson, J., Ganzeveld, L., Tegen, I., Werner, M., Balkanski, Y., et al. (2005). The aerosol-climate model echam5-ham. *Atmospheric Chemistry and Physics*, 5(4):1125–1156.

[132] Stier, P., Seinfeld, J., Kinne, S., and Boucher, O. (2007). Aerosol absorption and radiative forcing. *Atmospheric Chemistry and Physics*, 7(19):5237–5261.

[133] Svenningsson, B., Rissler, J., Swietlicki, E., Mircea, M., Bilde, M., Facchini, M., Decesari, S., Fuzzi, S., Zhou, J., Mønster, J., et al. (2006). Hygroscopic growth and critical supersaturations for mixed aerosol particles of inorganic and organic compounds of atmospheric relevance. *Atmospheric Chemistry and Physics*, 6(7):1937–1952.

[134] Takemura, T., Nozawa, T., Emori, S., Nakajima, T., and Nakajima, T. (2005). Simulation of climate response to aerosol direct and indirect effects with aerosol transport-radiation model. *Journal of Geophysical Research*, 110(D2):D02.

[135] Toner, S., Sodeman, D., and Prather, K. (2006). Single particle characterization of ultrafine and accumulation mode particles from heavy duty diesel vehicles using aerosol time-of-flight mass spectrometry. *Environmental Science and Technology*, 40(12):3912–3921.

[136] Tunved, P., Ström, J., and Krejci, R. (2013). Arctic aerosol life cycle: linking aerosol size distributions observed between 2000 and 2010 with air mass transport and precipitation at zeppelin station, ny-ålesund, svalbard. *Atmospheric Chemistry and Physics*, 13(7):3643–3660.

[137] Twomey, S. (1977). The influence of pollution on the shortwave albedo of clouds. *Journal of the Atmospheric Sciences*, 34:1149–1152.

[138] Twomey, S., Piepgrass, M., and Wolfe, T. (1984). An assessment of the impact of pollution on global cloud albedo. *Tellus B*, 36(5):356–366.

[139] Van Dingenen, R., Raes, F., Putaud, J.-P., Baltensperger, U., Charron, A., Facchini, M.-C., Decesari, S., Fuzzi, S., Gehrig, R., Hansson, H.-C., et al. (2004). A european aerosol phenomenology1: physical characteristics of particulate matter at kerbside, urban, rural and background sites in europe. *Atmospheric Environment*, 38(16):2561–2577.

[140] VanReken, T. M., Rissman, T. A., Roberts, G. C., Varutbangkul, V., Jonsson, H. H., Flagan, R. C., and Seinfeld, J. H. (2003). Toward aerosol/cloud condensation nuclei (ccn) closure during crystal-face. *Journal of Geophysical Research: Atmospheres (1984–2012)*, 108(D20).

[141] Walsh, J. E. and Chapman, W. L. (2001). 20th-century sea-ice variations from observational data. *Annals of Glaciology*, 33(1):444–448.

[142] Wang, J., Cubison, M., Aiken, A., Jimenez, J., and Collins, D. (2010). The importance of aerosol mixing state and size-resolved composition on CCN concentration and the variation of the importance with atmospheric aging of aerosols. *Atmosphic Chemistry and Physics*, 10(15):7267–7283.

[143] Watson, G. S. (1964). Smooth regression analysis. *Sankhyā: The Indian Journal of Statistics, Series A*, pages 359–372.

[144] Weingartner, E., Burtscher, H., and Baltensperger, U. (1997). Hygroscopic properties of carbon and diesel soot particles. *Atmospheric Environment*, 31(15):2311–2327.

[145] Wexler, A., Lurmann, F., and Seinfeld, J. (1994). Modelling urban and regional aerosols–i. model development. *Atmospheric Environment*, 28(3):531–546.

[146] Whiteaker, J. R., Suess, D. T., and Prather, K. A. (2002). Effects of meteorological conditions on aerosol composition and mixing state in bakersfield, ca. *Environmental science & technology*, 36(11):2345–2353.

[147] Wilson, J., Cuvelier, C., and Raes, F. (2001). A modeling study of global mixed aerosol fields. *Journal of Geophysical Research: Atmospheres (1984–2012)*, 106(D24):34081–34108.

[148] Woodworth, P., White, N. J., Jevrejeva, S., Holgate, S., Church, J., and Gehrels, W. (2009). Evidence for the accelerations of sea level on multi-decade and century timescales. *International Journal of Climatology*, 29(6):777–789.

[149] Wright, D. L., McGraw, R., and Rosner, D. E. (2001). Bivariate extension of the quadrature method of moments for modeling simultaneous coagulation and sintering of particle populations. *Journal of Colloid and Interface Science*, 236(2):242–251.

[150] Yu, S., Eder, B., Dennis, R., Chu, S.-H., and Schwartz, S. E. (2006). New unbiased symmetric metrics for evaluation of air quality models. *Atmospheric Science Letters*, 7(1):26–34.

[151] Zaveri, R., Easter, R., Fast, J., and Peters, L. (2008). Model for simulating aerosol interactions and chemistry (MOSAIC). *Journal of Geophysical Research*, 113:D13204.

[152] Zaveri, R., Easter, R., and Peters, L. (2005a). A computationally efficient multicomponent equilibrium solver for aerosols (MESA). *Journal of Geophysical Research*, 110(D24):D24203.

[153] Zaveri, R., Easter, R., and Wexler, A. (2005b). A new method for multicomponent activity coefficients of electrolytes in aqueous atmospheric aerosols. *Journal of Geophysical Research*, 110(D2):D02201.

[154] Zaveri, R. and Peters, L. (1999). A new lumped structure photochemical mechanism for large-scale applications. *Journal of Geophysical Research*, 104(D23):30387–30.

[155] Zaveri, R. A., Barnard, J. C., Easter, R. C., Riemer, N., and West, M. (2010). Particle-resolved simulation of aerosol size, composition, mixing state, and the associated optical and cloud condensation nuclei activation properties in an evolving urban plume. *Journal of Geophysical Research*, 115(D17).

[156] Zhang, G., Bi, X., He, J., Chen, D., Chan, L. Y., Xie, G., Wang, X., Sheng, G., Fu, J., and Zhou, Z. (2014). Variation of secondary coatings associated with elemental carbon by single particle analysis. *Atmospheric Environment*, 92:162–170.

[157] Zhang, R., Khalizov, A. F., Pagels, J., Zhang, D., Xue, H., and McMurry, P. H. (2008). Variability in morphology, hygroscopicity, and optical properties of soot aerosols during atmospheric processing. *Proceedings of the National Academy of Sciences*, 105(30):10291–10296.

[158] Zhang, Y., Seigneur, C., Seinfeld, J. H., Jacobson, M. Z., and Binkowski, F. S. (1999). Simulation of aerosol dynamics: A comparative review of algorithms used in air quality models. *Aerosol Science & Technology*, 31(6):487–514.

[159] Zuberi, B., Johnson, K., Aleks, G., Molina, L., Molina, M., and Laskin, A. (2005). Hydrophilic properties of aged soot. *Geophysical Research Letters*, 32(1).